NASA Technical Memorandum 104791

The Lunar Scout Program

An International Program to Survey the Moon From Orbit for Geochemistry, Mineralogy, Imagery, Geodesy, and Gravity

Edited by Donald A. Morrison

APRIL 1994

NASA Technical Memorandum 104791

The Lunar Scout Program

An International Program to Survey the Moon From Orbit for Geochemistry, Mineralogy, Imagery, Geodesy, and Gravity

Edited by Donald A. Morrison
Lyndon B. Johnson Space Center
Houston, Texas

National Aeronautics and
Space Administration

Contents

	Page
Introduction	1
A Short History of the Lunar Scout Program	2
Instrument Selection	3
Spacecraft Procurement	3
Termination of the Lunar Scout Program	4
Program Objectives and Goals	5
Schedule	6
Program Organization and Structure	7
Budget	9
Spacecraft and Instrument Module	10
Instruments	13
Instrument Descriptions	16
X-ray Fluorescence Spectrometer	16
High Resolution Stereo Camera	18
LANL Neutron Spectrometer	20
LANL Ge Gamma Ray Spectrometer	21
Imaging Spectrometer (MinMap)	22
Gravity experiment	24
Ballistic Missile Defense Organization (BMDO) LADAR	25
Mapping Strategies	26
Introduction	26
Lunar Scout I	26
Global Mapping Strategy	26
Lunar Scout II	32
Global Mapping Phase	33
Regional High Resolution Mapping Phase	39
Preliminary Mission Analysis	40
Overview	40
Instrument and Operational Considerations	40
Trajectory Design Considerations	45
Launch Window Design	46
Mission Summary	49
Operations Concepts	52
Mission Operations Plan	52
Prelaunch Support	54
Launch Operations	54
Telemetry, Tracking, and Navigation	54
Mission Control	55
Science Data Distribution	55
Data Analysis	55
Ancillary Data	55
Project Data Archive	56
Mission Planning and Sequence Integration	56
Payload Control	56
Mission Studies	57
Photogrammetry	57
Lunar Trajectory Interpolation for HRSC Stereo Mapping	59
Background	59
Objective	59
Methodology	59

Contents
(continued)

	Page
Results	60
Conclusions	61
Lunar Scout Gravity Mapping	61
Introduction	61
Two-Spacecraft Geometry Options	62
Objective	62
Methodology	62
Results	62
Wedge Angle	63
Scout II Apsides Angle	64
Tracking Duration / Scout II Orbit Period	64
Conclusions	65
Gravity Field Extraction	65
Objective	65
Methodology	66
Results	66
Conclusions	71
Co-Orbiting Satellite Options	72
Objective	72
Methodology	72
Orbit Lifetimes	72
Formation Lifetimes	73
Gravity Modeling Errors	73
Velocity Insertion Errors	73
Navigation Errors	73
Results	74
Orbit Lifetimes	74
Formation Lifetimes	74
Gravity Modeling Errors	74
Velocity Insertion Errors	74
Navigation Errors	74
Conclusions	75
Radiometric Tracking Power Requirements	75
Objective	75
Methodology	75
Results	76
Conclusions	79
References	83

Contents
(continued)

Page

Appendixes

Appendix A - Lunar Scout: Crossrange Movement for Evaluation of Swath Width Overlap of the Lunar Scout Spacecraft A-1

Appendix B - Polynomial Curve Fit of Lunar Trajectory Segments B-1

Appendix C - A General Analysis of the Effects of Both Deterministic and Stochastic Pointing Fluctuations on Imaging Performance C-1

Appendix D - New Ways of Doing Business D-1

Contents
(continued)

Page

Figures

1	Lunar Scout Program schedule - June 1993	6
2	Organization of the Lunar Scout Program Office in FY93 after the disbandment of the Office of Exploration	8
3	Lunar Scout instrument module block diagram	12
4	Illustration of the instrument selection process used by the Lunar Scout Program	13
5	Geometry of the HRSC focal plate arrays relative to the imaged surface	19
6	Image cube geometry of MinMap	24
7	Swath width in kilometers as a function of orbit altitude	26
8	Swath width in pixels as a function of spacecraft altitude	27
9	Swath length for the HRSC	27
10	Data collection and downlink strategy for the HRSC	28
11	Global imaging strategy based on a data storage constrained scenario	29
12	Derived pointing and orbit inclination tolerances, given the mission scenario shown in table XIII for global stereo mapping by the HRSC	30
13	Improvements in global resolution are significant with a small increase in storage capacity	31
14	Swath width in kilometers and in pixels as a function of orbit altitude	33
15	Swath length as determined by the requirement to have 10% sidelap at the equator	34
16	Acquisition of signal cases (AOS) and loss of signal cases (LOS) determine maximum spatial and spectral resolution that is achievable for global mapping given mission and spectrometer capabilities	34
17	Aos mapping scenario for MinMap	35
18	22% of the Moon must be imaged at a reduced rate from an altitude of 500 km	36
19	Strategies for far-side mapping	37

Contents
(continued)

Page

Figures

20	Derived tolerances for pointing deviation and orbit inclination	38
21	Instrument dependence on Sun (beta) angle	42
22	Lunar mapping considerations	43
23	Scout launch window - LOI delta-V	47
24	Scout I launch window - TLI delta-V	48
25	Lunar Scout I "strawman" mission profile	50
26	Lunar Scout II "strawman" mission profile	51
27	Tracking, data acquisition, and control overview	53
28	Vertical measurement opportunities	62
29	Surface coverage vs. wedge angle	64
30	Downrange/radial velocity perturbation sensitivity	68
31	Radial/downrange velocity perturbation sensitivity	68
32	Radial/crosstrack perturbation sensitivity (degree 30)	69
33	Crosstrack/radial velocity perturbation sensitivity (degree 30)	69
34	Radial/crosstrack perturbation sensitivity (order 30)	70
35	Crosstrack/radial perturbation sensitivity (order 30)	70
36	Active target transmission power estimates: co-orbiting satellites	77
37	Active target transmission power estimates: 500 x 7000 km elliptical relay orbit	77
38	Passive target transmission power estimates	78
39	Passive target transmission power cost vs. antenna gain	78

Contents
(continued)

Page

Tables

1	Lunar Scout Program Budget	9
2	Lunar Scout Spacecraft Bus Orbital Mission Requirements	10
3	Lunar Scout Spacecraft Bus Performance Requirements	11
4	Instruments Manifested on Scout I And II	14
5	Technical Attributes of the Instruments Manifested on Lunar Scout I And II	15
6	Physical Characteristics of the X-Ray Spectrometer	16
7	XRF Integration Times for Compositional Determination	17
8	HRSC Physical Characteristics	20
9	Physical Characteristics of the Neutron Spectrometer	21
10	Physical Characteristics of the Gamma Ray Spectrometer	22
11	MinMap Physical Characteristics	23
12	Bmdo Ladar Altimeter Characteristics	25
13	Nominal Mapping Strategy for Global Mapping by the HRSC on Lunar Scout I	29
14	Regional Mapping Strategy Parameters for the HRSC on Lunar Scout I	32
15	Cumulative Data Load Produced by the HRSC, Scout I, Excluding Photometry And Color Channels	32
16	Comparison of Results of Near-Side and Far-Side Mapping	37
17	Mapping Strategy Summary for Global Mapping of MinMap	38
18	Regional Mapping Parameters for MinMap	39
19	Mission Design Considerations	40
20	Measurement Objectives for Lunar Scouts I and II	41
21	Instrument Operational Constraints for Lunar Scouts I and II	41
22	Mission Mapping Parameters for Lunar Scout I	44

Contents
(concluded)

Page

Tables

23	Mission Mapping Parameters for Lunar Scout II	45
24	Delta-V Budget for Lunar Scouts I and II	45
25	HRSC and Mission Parameters for Both the Global and Regional Mapping Phases	57
26	Maxium Interpolation Errors for 3rd Order Lagrange Polynomial (5 X 5 Spherical Harmonic Gravity Model With Point Mascons)	60
27	Maximum Interpolation Errors for 3rd Order Lagrange Polynomial (75 X 75 Spherical Harmonic Gravity Model)	61
28	Parametric Variations - General Trend Analysis	63
29	Change in Coverage vs. Line of Apsides Rotation	64
30	Far-Side Coverage vs. Bin Width	65
31	Maximum Formation Errors After 1 Month	74

Acronyms

ABE	Army Background Explorer
ADC	Analog to digital conversion
AO	Announcement of Opportunity
AOS	acquisition of signal
APL	Applied Physics Laboratory
BMDO	Ballistic Missile Defense Organization
CBD	Commerce Business Daily
CCD	charge-coupled-devices
CCT	Central Communications Terminal
DARA	German Space Agency
DSCC	Deep Space Communications Complex
DSN	Deep Space Network
DTM	digital terrain model
GCF	Ground Communications Facility
GPS	global positioning system
GRS	gamma ray spectrometer
GSFC	Goddard Space Flight Center
HRSC	High Resolution Stereo Camera
ICD	Interface Control Document
IFOV	instantaneous field of view
JPL	Jet Propulsion Laboratory
JSC	Johnson Space Center
KSC	Kennedy Space Center
LANL	Los Alamos National Laboratory
LExSWG	Lunar Exploration Science Working Group
LLNL	Laurence Livermore National Laboratory
LOI	lunar orbit insertion
LOS	loss of signal
LSMCC	Lunar Scout Mission Control Center
LSMOT	Lunar Scout Mission Operations Team
LVLH	local vertical local horizontal"
m	meters
m/p	meters per pixel
MCT	Mission Control Team
MinMap	imaging spectrometer
MMNav	Multi-mission Navigation Team
MMT	Mission Management Team
NOCC	Network Operations Control Center
NS	Neutron Spectrometer
OMB	Office of Management and Budget
PCC	Payload Control Center
PI	Principal Investigator
PIU	payload interface unit
RFP	Request for Proposal
SiCCD	silicon charge-coupled-device
TLI	trans-lunar injection
XRF	X-ray fluorescence
XRS	X-ray spectrometer

Introduction

This report summarizes the results of the work of the Lunar Scout Program Office in the planning and development of the Lunar Scout Program from 1991 to 1993.

The Lunar Scout Program was one of a series of attempts by NASA to develop and fly an orbiting mission to the Moon to collect global geochemical, geological, and gravity data. Predecessors were the Lunar Observer (circa 1989-92), the Lunar Geochemical Orbiter proposed in the early 1980s, and the Lunar Polar Orbiter discussed in the mid-1970s—all three missions studied under the auspices of the Office of Space Science.

Unlike its predecessors, the Lunar Scout Program was an initiative of the Office of Exploration. The Program was begun in late 1991 and continued under the auspices of the Office of Exploration until 1993 when it was transferred to the Office of Space Science after the disbanding of the Office of Exploration.

Most of the work was done by a small group of civil servants in the Exploration Programs Office, an arm of the Office of Exploration (Code X) located at the Center from 1991 to 1993. Personnel of the Charles Stark Draper Laboratories and the Lawrence Livermore National Laboratory, which is operated by the University of California for the Department of Energy, played key roles in mission planning. The Boeing Company and the Martin Marietta Corporation made significant corporate investments in developing spacecraft designs and mission scenarios in response to a Request for Proposal for which funds were rescinded by Congress in 1992.

Like its predecessors, the Lunar Scout Program did not survive the budget process. It failed to achieve New Start funding in the FY93 and 94 budgets. It was a casualty of the downturn in the budget as well as the shift in emphasis that resulted in the disbanding of the Office of Exploration and the de-emphasis of the Space Exploration Initiative announced by President Bush in 1989. Furthermore, as was the case for earlier lunar mission proposals, lunar science did not have an overriding priority among space science advisory groups, and it did not have first place in the queue in planetary science. In an intensely competitive funding atmosphere, particularly in the absence of an imperative related to the Space Exploration Initiative, only the highest priority missions achieve New Start status. But the work done on the Lunar Scout Program and other lunar orbiter studies represents assets that will be useful in developing new approaches to lunar orbit science. The purpose of this report is to document those assets.

A Short History of the Lunar Scout Program

The Lunar Scout Program began in late 1991 following the formation of the Office of Exploration and the commitment of NASA to the Space Exploration Initiative. It was to be one of the first in a series of low-cost, fast-paced missions that would provide the fundamental science and engineering data needed to prepare the way for follow-on human and robotic exploration of the Moon. The Office of Exploration began preparations to plan, design, and construct a lunar base. They concluded that fundamental characterization of the planet from lunar orbit was a necessary precursor for lunar base site selection and lunar exploration. The Lunar Scout Program resulted. The Office of Exploration pressed forward with its implementation until the fall of 1992 when the Office was disbanded. The Lunar Scout Program proceeded thereafter under the auspices of the Office of Space Science until October of 1993 when it failed to achieve a New Start in the FY94 budget.

The Office of Exploration formed a program plan and a budget with an FY92 New Start target date for a lunar orbiter program that became Lunar Scout in late 1991. The following guidelines for the program were established to minimize cost and to proceed from New Start approval to launch in three years. The guidelines were intended to implement the policy of carrying out frequent small-scale, rapidly paced robotic missions executed under strict cost caps.

- The program consisted of two launches, both on Delta II 7925s capable of inserting approximately 1300 kg (spacecraft, fuel, payload) into lunar orbit—the first launch scheduled originally for March 1995 and the second, for March 1996. Mission operation funding was to cease at one year from launch.

- The spacecraft were to be procured competitively from a commercial source.

- Schedule from New Start to launch was set at 30 months (originally an October 1992-FY93 New Start and a March 1995 launch for the first orbiter). This schedule allowed approximately 22months for fabrication and delivery of payloads for integration to the spacecraft.

- Cost per launch was to be held to $120 million in FY92 dollars. This cost included payload ($20M), launch vehicle ($50M), spacecraft (approximately $30M), and operations cost ($20M). Michael Griffin, Associate Administrator for Exploration, made a commitment to this cost cap to the Congress in the spring of 1992.

- The Applied Physics Laboratory (APL) of Johns Hopkins University was to be responsible for project management and mission integration.

- An instrument module provided the flexibility to accommodate a variety of requirements. APL was responsible for the design and construction of the instrument module.

- Program management was minimized and primary responsibility placed with industry and the APL. Program management was under the auspices of the Exploration Programs Office located at the Johnson Space Center (JSC). Full authority, including procurement authority, was vested in the program office. A Lunar Scout Program Office under Michael Conley was established by the Explorations Program Office at JSC, and a Project Office at APL under Tom Coughlin was formed in March 1992.

These guidelines provided a framework for mission implementation that was quite different from earlier efforts to develop a lunar orbiting mission. Schedule and cost guidelines eliminated consideration of spacecraft or instruments that were not fully developed. The requirement to have both spacecraft and instruments ready for integration in 22 months eliminated all but the most mature hardware, systems, and software. Procurement methods had to be accelerated. Instrument selection via the classical Announcement of Opportunity (AO) process was not possible, and selection proceeded with a market survey approach.

With the guidelines established, the Office of Exploration initiated a process for instrument selection in December 1991 and issued a Request for Proposal (RFP) for a commercial spacecraft buy.

Instrument Selection

A Commerce Business Daily (CBD) announcement was issued in December 1991 calling for ideas for instruments for lunar orbiting missions. The proposals received were discussed and evaluated by a peer group in a workshop held at the Lunar and Planetary Institute in February 1992. Proposals were ranked in terms of maturity (i.e., readiness for flight) and science return. The workshop functioned as a market survey and served as the basis for instrument selection for the Lunar Scout Program.

Instrument selection was begun by the Lunar Scout Program Office in March 1992 with the LPI workshop report as a basis for consideration of instruments that would be capable of meeting cost and schedule constraints. The proposed March 1995 and 1996 launches and imminent spacecraft procurement required quick selection so that instrument requirements could be considered in the spacecraft study phase and instrument teams could be on board and ready to proceed in October 1992, the proposed New Start date of the program. The LPI workshop market survey rankings were used to develop a list of candidate instruments. The kinds of instruments required were defined by the measurement objectives set out by the Lunar Exploration Science Working Group (LExSWG). The need to limit consideration to developed instruments limited the number of candidates to a very few.

Instruments were reviewed that could provide global and local elemental mapping (including a measure of volatiles of which hydrogen was considered to be the key), mineralogical mapping, geodesy, a digital imagery data base at between 10 and 20 m/p for a global database and less than 10 m/p for local and regional imagery, and a means to map the gravity field of the Moon and correlate it with terrain features.

The candidate instruments were reviewed in a two-step review process that took place over several months. Detailed cost, schedule, and performance profiles for each of the candidate instruments were reviewed. The review team included prominent non-NASA scientists with the necessary technical expertise and experience. The results of this process were announced in late June 1992.

Spacecraft Procurement

A "horse race" spacecraft procurement strategy was adopted for a commercial buy of developed spacecraft. The strategy consisted of a two-stage procurement plan. The first stage was the selection of two vendors to complete a four-month "pre-phase A" study simultaneously and in competition. The product of the "pre-phase A" study was to be a final proposal allowing for down selection to a spacecraft vendor. This strategy allowed potential vendors to become thoroughly familiar with requirements as they developed their proposals.

An RFP for the spacecraft "pre-phase A" study contract was issued in February with the deadline for selection in June. The Martin Marietta and Boeing Companies were selected from among the respondents. The RFP called for a four-month study of spacecraft design and mission profiles, and required the submission of a proposal at the end of the study phase for spacecraft fabrication and operation for one year in lunar orbit. The "pre-phase A" study was not completed because funds for its initiation were withdrawn by Congress in August 1992.

Termination of the Lunar Scout Program

In August 1992, funds for support of the Office of Exploration and for the support of the Exploration Programs Office located at JSC were rescinded by the Congress. This action prevented implementation of the Lunar Scout spacecraft phase I RFP.

The FY92 budget, submitted to Congress, contained funds for a New Start for Lunar Scout, but the funds were not appropriated. Congressional action in FY93 led to disbanding of the Office of Exploration and the shift of its responsibilities to the Office of Space Science and Applications (now the Office of Space Science, Code S). Code S carried forward a budget submittal for an FY94 New Start for Lunar Scout. This submittal was rejected, and the Lunar Scout Program was removed from consideration as a New Start.

Program Objectives and Goals

The overarching science goal of the Lunar Scout Program was adapted from the rationale for its predecessors, namely to "further our understanding of the Moon's early history as a scientific objective in its own right and also because of the impact such understanding would have on the general scientific goals of planetary exploration" (Solar System Exploration Committee of the NASA Advisory Council, part 1, 1983). An Office of Exploration programmatic objective was to prepare for follow-on human and robotic missions. This objective placed added emphasis on the value of a geodetic net and refinement of the gravity field because of their implications for spacecraft navigation to very precisely located preselected sites on the lunar surface.

The Office of Exploration adopted as guidelines the science themes and measurement objectives established by LExSWG. LExSWG had been chartered by the Office of Space Science and Applications and "Code Z," the Office of Exploration's predecessor, to provide scientific expertise and advice. The measurement objectives of the Lunar Scout Program, as adapted from LExSWG recommendations, were

- **Determine the elemental and mineralogical composition of the lunar surface.**
  Global and regional maps of the chemical composition of the lunar regolith, including an assessment of volatile content, at scales that can be used to discriminate geological units on the lunar surface. Elements to be mapped include the major rock-forming elements, minor elements, selected trace elements, and hydrogen. Mapping of chemical compositions accomplished by gamma ray spectrometry, X-ray spectrometry, and neutron spectrometry.

- **Determine the mineralogical composition of the lunar surface.**
  Global maps of the common rock-forming minerals and their abundances in the lunar regolith, supplemented by higher resolution regional maps of mineral modes of selected areas. Mineralogy determined spectroscopically.

- **Obtain global stereo imagery.**
  Global stereo imagery of the Moon at a resolution between 15 and 20 m/p with a target objective of 20 m/p. Global stereo imagery supplemented by regional stereo imagery of selected areas with an average resolution of 4 m/p.

- **Provide global geodesy and topography.**
  Produce a digital terrain model with geodetic fidelity and provide data for construction of a global geodetic map of the Moon with positional control of hundreds of meters or better and elevation control of better than 50 m.

- **Determine the global lunar gravity field.**
  Map the gravity field globally to the mGal level to allow orbit stability predictions on the order of 600 m (3-sigma) per orbit.

The instruments and systems selected to achieve these measurement goals were

- X-ray Spectrometer (XRS) (Goddard Space Flight Center)
- Neutron Spectrometer (NS) (Los Alamos National Laboratory, or LANL)
- High Resolution Stereo Camera (HRSC) (German Aerospace Research Establishment)
- Gravity Experiment [investigator named via NASA Research Announcement (NRA)]
- Imaging Spectrometer (MinMap) (Brown University/SETS Technology/Ball Aerospace)
- Ge Gamma Ray Spectrometer (LANL)
- Gravity (program provided altimeter and oscillators, NRA selected investigators).

Schedule

A general schedule for the major events of Lunar Scout I and II as formulated in June 1993 is shown in figure 1.

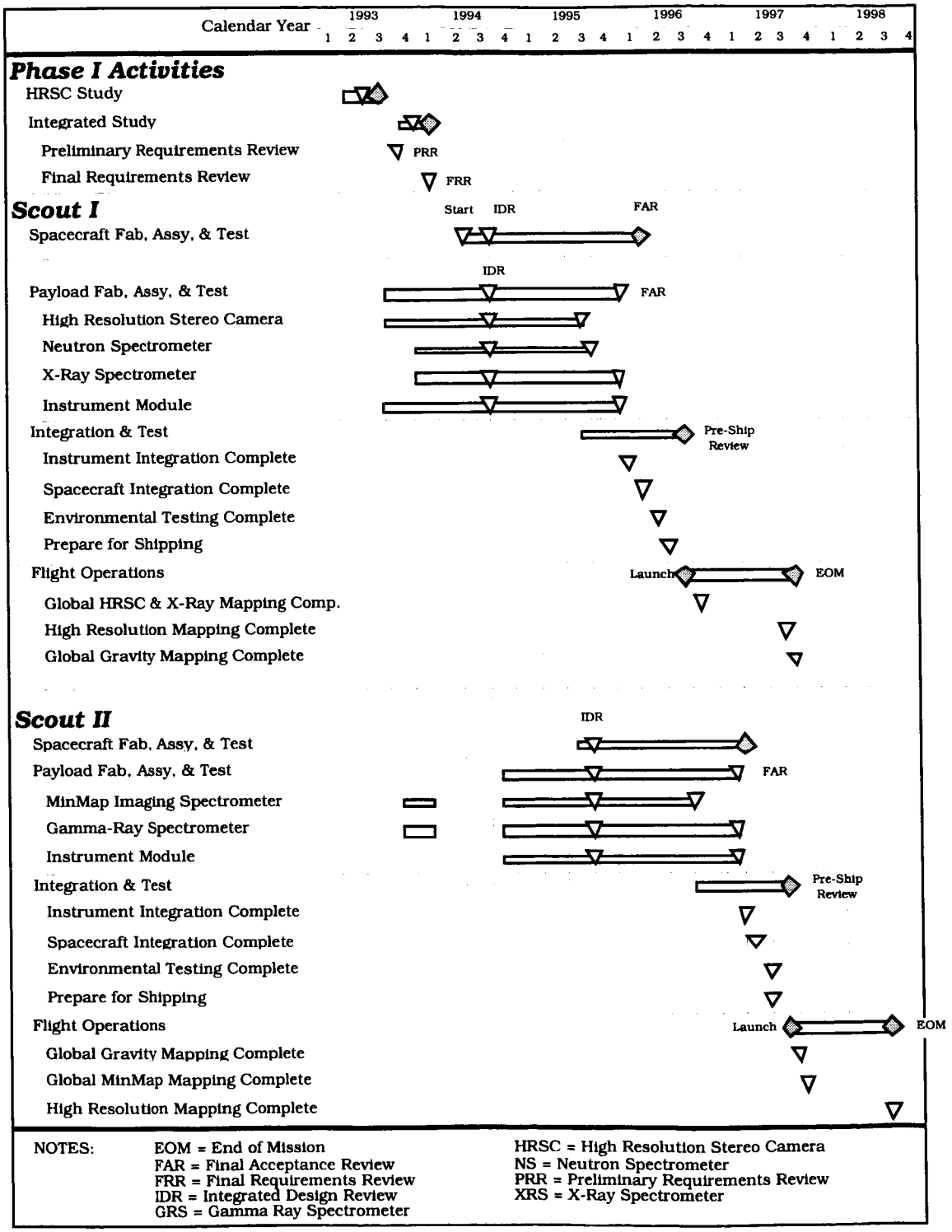

Figure 1. Lunar Scout Program schedule - June 1993.

Program Organization and Structure

A Lunar Scout Program Office was formed in April 1992 by the Office of Exploration and located at JSC within the Exporation Programs Office, an Office of Exploration organ-ization located at JSC.

Full authority was delegated to the Lunar Scout Program Manager. Procurement authority was delegated as well and to JSC procurement specialists. Decision-making power was vested in the Program Manager for direction of APL, instrument selection (with approval by the Associate Administrator), mission organization and operating principles, spacecraft procurement and direction of commercial vendors, and mission operations and operational decisions and Program Control. This authority simplified the chain of command and improved efficiency greatly. Oversight was provided by the Deputy Associate Administrator for Exploration and the Exploration Programs Office Manager.

Project management and project science management were placed in the hands of APL of Johns Hopkins University. APL had responsibility for developing a mission operations plan, mission science operations planning, mission integration, instrument module construction, integration and testing, module-to-spacecraft integration and testing, mission operations, operation of a mission control center, and development of mission operations scenarios.

In the fall of CY1992 and after the beginning of FY93, the Office of Exploration was disbanded and the Lunar Scout Program became a part of the Office of Space Science under the direction of the Solar System Exploration Division (Code SL). The essentials of the Lunar Scout Program Office remained intact during the budget submittal process for FY94. The organizational structure during this period under Office of Space Science and Applications (Code S) is shown in figure 2.

The Lunar Scout Program Office in the Exploration Programs Office consisted of the following:

Michael G. Conley, Program Manager
Bret G. Drake, Chief Engineer
Kent Joosten, Operations Manager
Donald A. Morrison, Program Scientist
Mark C. Nebrig, Business Manager
Brenda Ward, Instruments Manager
Taylor Lawrence (Lawrence Livermore National Laboratory), Technical Assistant

The adjective "Program" in Program Manager and Program Scientist would have been changed to the traditional "Project " had the program been funded under the auspices of the Office of Space Science.

An advisory group of non-NASA scientists played an important role in providing science guidance to the program, particularly in instrument selection: Dr. James Arnold, University of California, Dr. Larry Haskin, Washington University, Dr. William Farrand, Science Application International Corp., Dr. Robert Housley, Rockwell Co., Dr. James Anderson, Jet Propulsion Laboratory, Dr. Randolph Kirk, U.S. Geological Survey, Dr. Raymond Batson, U.S. Geological Survey, and Dr. Paul Spudis, Lunar and Planetary Institute.

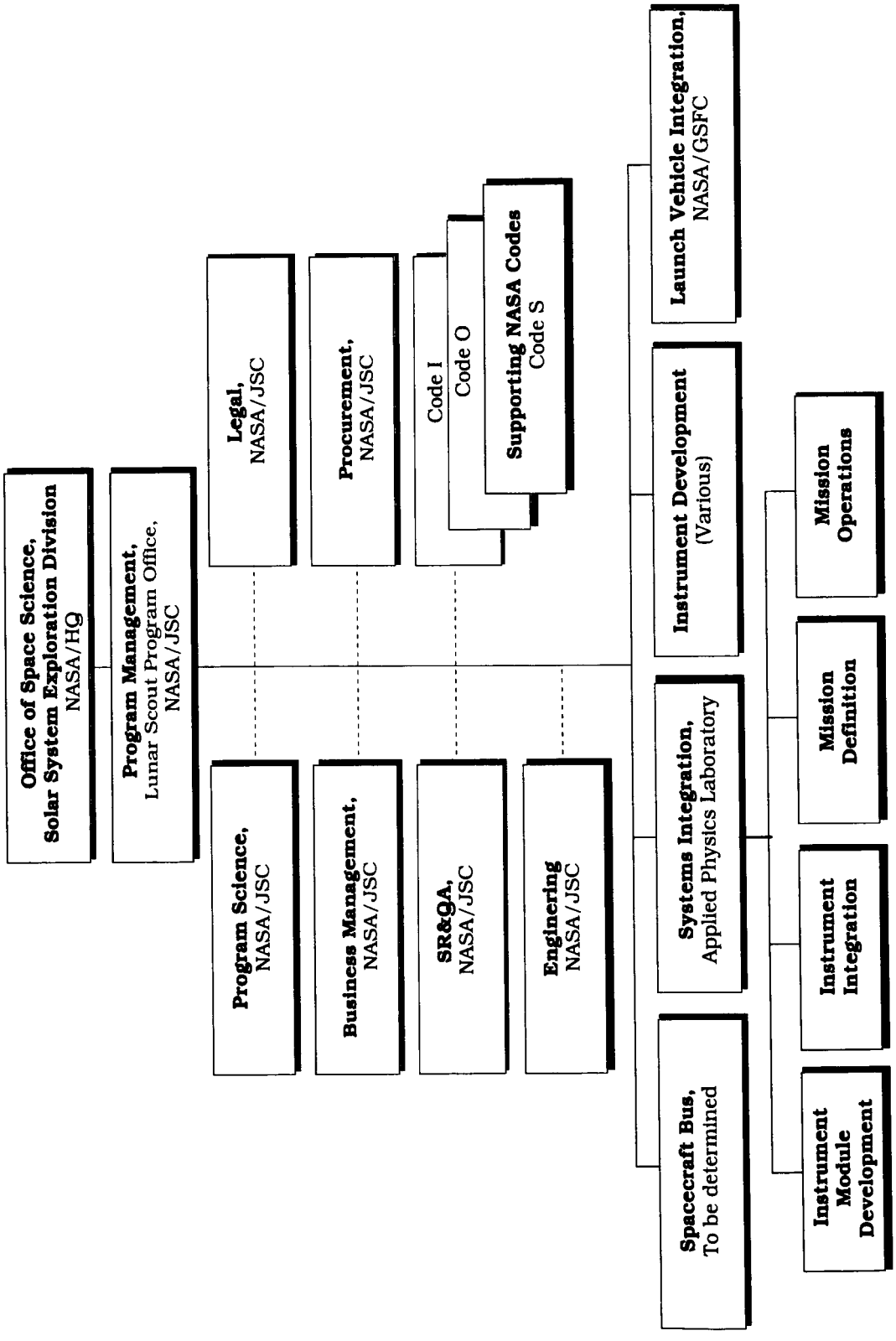

Figure 2. Organization of the Lunar Scout Program Office in FY93 after the disbandment of the Office of Exploration. The Office of Space Science submitted the Program to the Office of Management and Budget (OMB) for consideration in the FY94 budget for a New Start.

Budget

Table I shows the budget as submitted to the OMB by the Office of Space Science for an FY94 New Start for the Lunar Scout Program

TABLE I. LUNAR SCOUT PROGRAM BUDGET

	FY94	FY95	FY96	FY97	FY98	FY99	Total
Lunar Scout I							
Spacecraft	$15.7	$ 10.5	$ 5.2				$ 31.4
Hard X-ray	3.3	2.3	1.5				7.1
Neutron	2.5	1.6	2.0				6.1
LANL ops/products	0.7	0.8	0.4				2.0
HRSC		1.6	1.6				3.1
Front-side gravity	0.5	0.5	0.5				1.5
Instrument integration	3.2	6.0	3.8				13.0
Spacecraft total	$26.0	$ 23.2	$15.0				$ 64.3
Operations		3.2	5.2				8.4
Launch vehicle	5.4	38.8	11.4				55.6
Tracking	0.1	1.7	6.6	$ 4.5	$3.3		16.1
Reserve		4.2					4.2
Mission total	$31.5	$ 71.1	$38.2	$ 4.5	$3.3		$148.5
Lunar Scout II							
Spacecraft	2.1	15.7	3.1	5.2			26.1
MinMap		3.6	2.8	1.1			7.6
Gamma-ray		5.6	3.0	2.0			10.6
LANL ops/products		0.7	0.8	0.4			2.0
Global gravity		0.5	0.5	0.6			1.6
Instrument integration		1.5	2.9	1.9			6.4
Spacecraft total	$ 2.1	$ 27.7	$13.2	$11.3			$ 54.3
Operations			3.2	5.2			8.4
Launch vehicle	2.3	22.5	20.2	11.9			56.9
Tracking	0.1	0.6	2.8	5.1	4.0	4.0	16.6
Reserve			7.2				7.2
Mission total	$ 4.5	$ 50.8	$46.6	$33.5	$4.0	$4.0	$143.3
Two mission total	**$36.0**	**$121.9**	**$84.8**	**$38.0**	**$7.3**	**$4.0**	**$291.9**

All cost in real year $M.

Spacecraft and Instrument Module

The Lunar Scout program consisted of two identical spacecraft which were to be procured from a commercial supplier. Each Lunar Scout spacecraft is composed of a spacecraft bus and an instrument module. The purpose of the instrument module is to isolate the spacecraft bus from the instruments so that an off-the-shelf spacecraft can be fabricated in parallel with the instrument development cycle. The intent of the parallel development is to reduce the overall program schedule and cost. The idea is to create a single unit on the instrument module that contains the variability specific to a particular mission. In this manner, a single spacecraft design can accommodate a variety of exploration missions and instrument sensors. In addition, by merging the interface problems into a single unit, the risks associated with interfaces are localized where they can be better managed.

The Lunar Scout spacecraft is a three-axis stabilized spacecraft launched from a Delta 7925. The spacecraft bus serves as the basic transportation element providing power, pointing and attitude control, and telemetry. Tables II and III provide a summary of the Lunar Scout spacecraft performance requirements. These requirements were current best estimates and were to be updated as the mission and technical studies progressed. Final selection of the spacecraft design and spacecraft supplier was not completed prior to program termination.

The instrument module is composed of the scientific instruments, a mass storage unit, and a payload interface unit. A physical block diagram of the instrument module is shown in figure 3. The payload mass storage unit provides up to 1 Gbit of storage capability to record and plays back data from the instruments, except for the High Resolution Stereo Camera (HRSC), which supplies its own mass storage unit. The payload interface unit (PIU) interfaces the instruments with the spacecraft. It distributes the payload power and commands, as sent from the spacecraft, and collects and processes telemetry from the instruments.

TABLE II. LUNAR SCOUT SPACECRAFT BUS ORBITAL MISSION REQUIREMENTS

Orbital parameter	Phase I	Phase II	Phase III	Phase IV
Scout I				
Orbital altitude (km)	300 x 300	300 x 300	100 x 100	100 x 100
Altitude variation	±30%	±10%	TBD	TBD
Inclination	90°±0.5°	90°±0.5°	90°±TBD	90°±TBD
Duration (days)	30	30	305	30
Pointing mode	Coarse pointing	Active pointing	Active pointing	Coarse pointing
Scout II				
Orbital altitude (km)	7000 x 500	500 x 500	100 x 100	---
Altitude variation	TBD	±7%	TBD	---
Inclination	90°±0.5°	90°±0.5°	90°±TBD	---
Argument of periapsis	TBD	---	---	N/A
Duration (days)	30	30	305	---
Pointing mode	Coarse pointing	Active pointing	Active mapping	---

TABLE III. LUNAR SCOUT SPACECRAFT BUS PERFORMANCE REQUIREMENTS

Description	Requirement
Payload power - end of life	
Voltage	28 ± 6 V DC
Peak power	190 W
Average power	130 W
Minimum quiescent power*	10 W
Payload physical characteristics	
Total mass	177 kg
Inertia properties	TBD
Dimensions	TBD
Command and data handling	
Payload health & status data rate	500 bps
Maximum payload science data rate	1.0Mbps
Spacecraft data rate to be recorded**	1000 bps
Transmission frequency	S-band
Attitude determination and control	
Pointing accuracy (real-time)	4.7 mrad per axis, 3σ
Maximum drift rate (real-time)	0.3 mrad/sec per axis, 3σ
Pointing stability (real-time)	TBD
Absolute pointing knowledge (post-processing)	1.7 mrad per axis, 3σ
Relative pointing knowledge (post-processing)	1.7 mrad/20 sec per axis, 3σ
Frequency of attitude measurement	2 Hz
Accuracy of time tags	TBD
Reliability	
Spacecraft lifetime design requirement	1 year
Spacecraft lifetime design goal	3 years
Safe mode	Self initiating safe mode
Payload accommodations	
Thermal environment	Thermally isolated
Payload field of view	Unobstructed in nadir
Keep out zone	Provide anti-solar side
Structural interface	Mechanical bolt interface
Mounting platform	Provided by the spacecraft
Payload/spacecraft interface	Instrument module ICD***
Launch compatibility	
Launch vehicle	Delta II 7925
Payload fairing	Standard 2.9 m fairing

* Payload is in quiescent mode during lunar eclipse events.

** Spacecraft health and performance data will be stored by the instrument module during periods of loss-of- signal with earth.

*** Interface Control Document (ICD)

Appendix C is a comprehensive discussion of a general methodology for determining drift and jitter requirements for instruments with pointing and attitude control constraints.

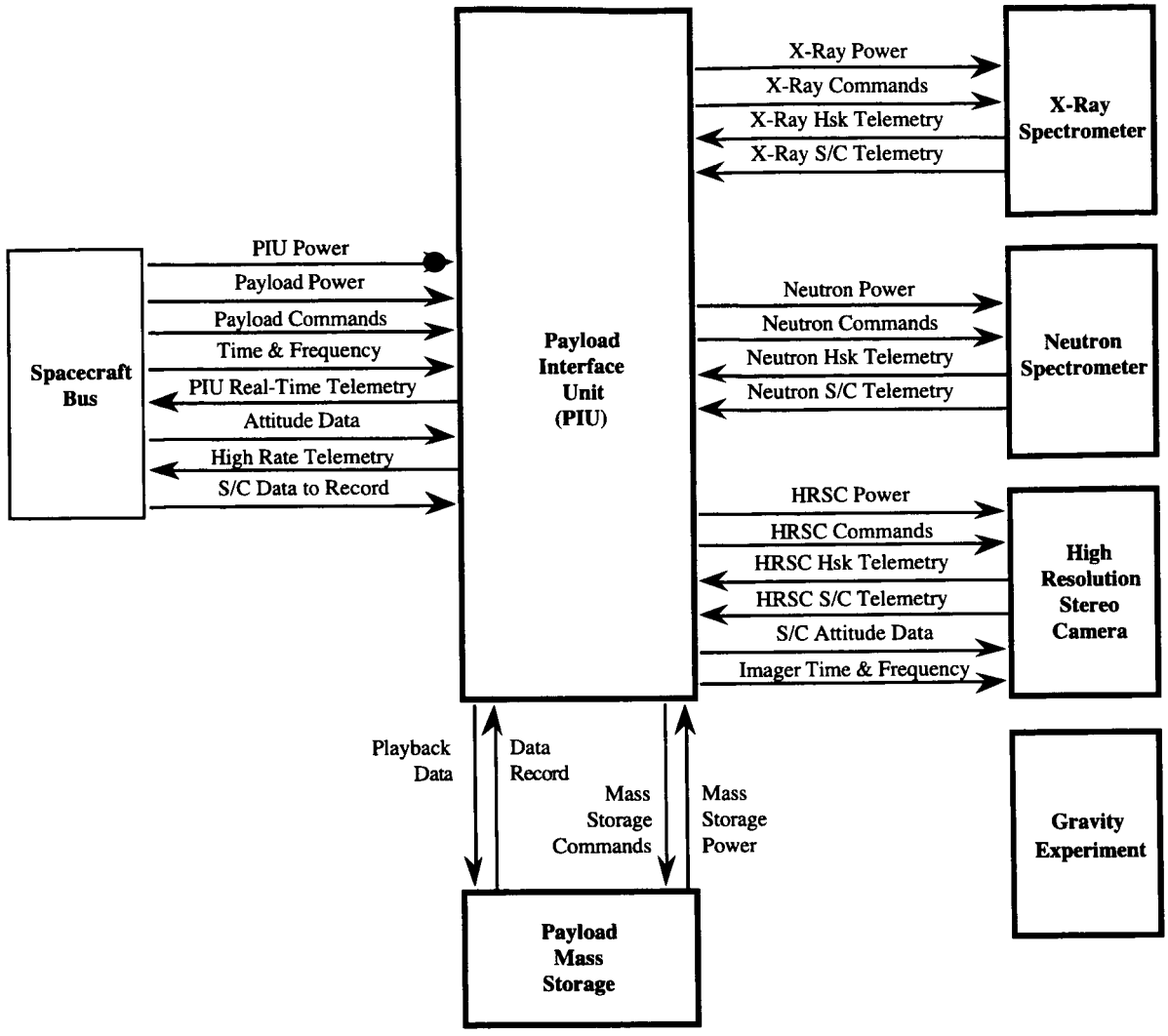

Figure 3. Lunar Scout instrument module block diagram.

Instruments

The instruments for the Lunar Scouts were selected by a process that represented a modification of the traditional AO. The Office of Exploration was formed in late 1991 and it designated FY92 (October 1991) as the New Start date for a lunar orbiter, first launch in March 1995. It was necessary, therefore, to select a spacecraft vendor and to select instruments and investigators by no later than June 1992. The traditional AO process could not be followed, and a market survey approach was taken as previously mentioned. All potential vendors who met basic criteria (cost, schedule, and mission suitability) were considered. Each Lunar Scout was limited to $20M for instrument costs in FY92 dollars. Prospective investigators had to deliver a functioning, fully capable instrument to the integration site in 22 months. The approach taken by the Lunar Scout Program for instrument selection is illustrated in figure 4.

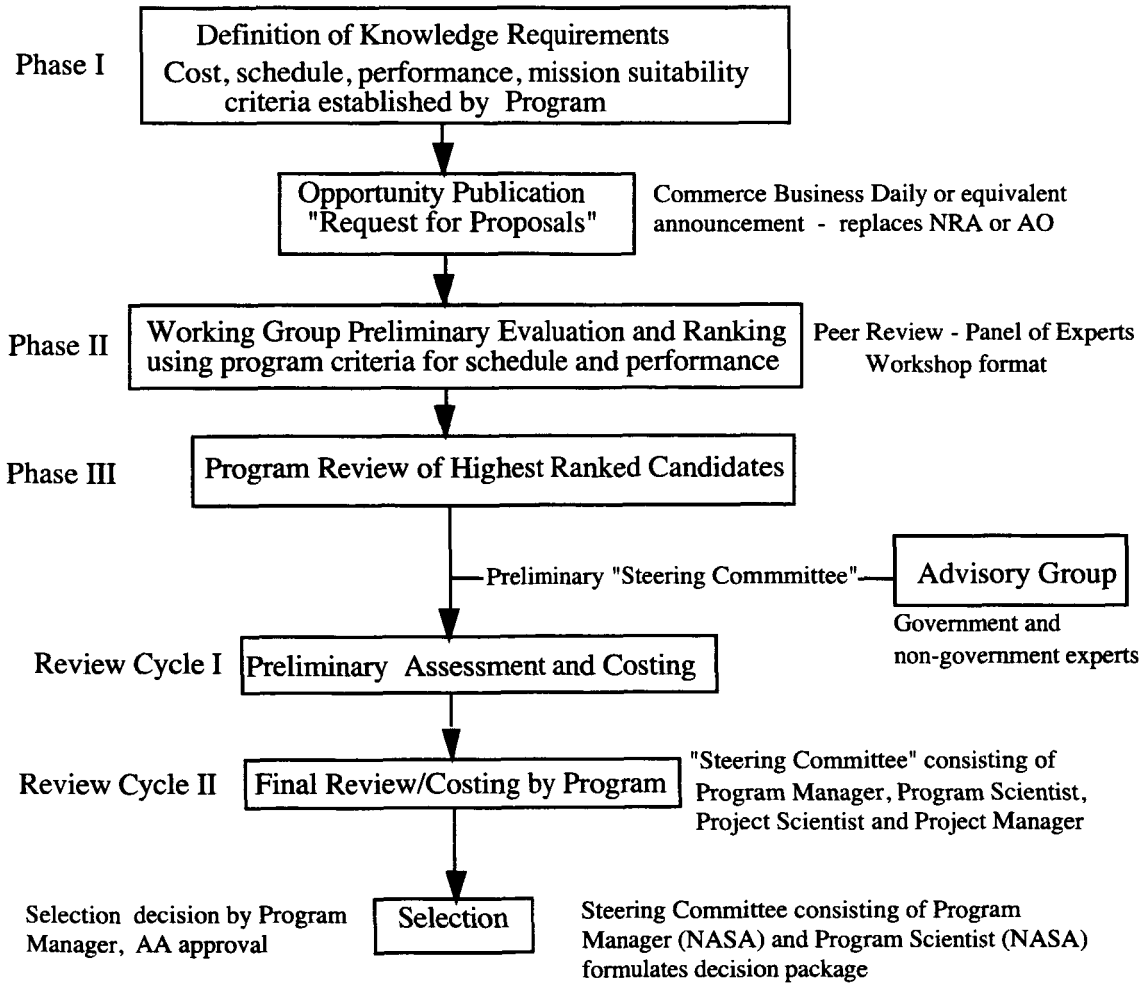

Figure 4. Illustration of instrument selection process used by the Lunar Scout Program. Scientific requirements followed guidelines established by LExSWG. Candidates to be reviewed were established by market survey mechanism; most were selected from a workshop report issued by the Lunar and Planetary Science Institute. This process satisfies all legal requirements.

The instruments selected for the Lunar Scouts are listed in table IV. Not listed in table IV is the Ballistic Missile Defense Organization (BMDO) LADAR altimeter that is manifested on the CLEMENTINE mission. An altimeter of this type was manifested on the Scout I spacecraft but was considered to be part of the spacecraft hardware necessary for accurate reconstruction of the spacecraft ephemeris and was not considered to be an instrument.

The allocation of the instruments between Scout I and II shown in table IV was determined by instrument maturity and costs. It was concluded that the imaging spectrometer (MinMap) and the Ge gamma ray spectrometer (GRS) would profit most by the extra time, provided by a 1996 instead of a 1995 launch, to prepare for integration to the spacecraft. The $20M cost cap for instruments per spacecraft prevented flying the gamma ray, NS, and MinMap on the same spacecraft, and the NS was placed on the first spacecraft. In addition, the HRSC and the GRS on the same spacecraft introduced some minor incompatibilities. Because of these factors the imaging system, the NS, and the X-ray spectrometer (XRS) were placed on Scout I. This risked an incomplete data set in the event of a failure or cancellation of the second spacecraft.

TABLE IV. INSTRUMENTS MANIFESTED ON SCOUT I AND II

Instrument/data	Investigator	Coverage
X-ray spectrometer Si, Mg, Al, Ca, Mg, Fe	Jack Trombka - Goddard Space Flight Center/Applied Physics Laboratory	Global, 10-40 km footprint
Neutron Spectrometer H, neutron spectra	George Auchampaugh - LANL	Global, 100 km footprint
High Resolution Stereo Camera: Global and regional imagery, topography, geodesy	Gerhard Neukum - German Aerospace Research Establshment	Global stereo; 24 m/p Regional stereo; 4 m/p Topo; 20-50 m global 100 meter lat. and long.
Gamma ray spectrometer U, K, Th, Sm, Gd, O, Na, H, Mg, Al, Si, S, Ca, Ti, Mn, Fe	Cal Moss - LANL	Global, 100 km footprint
Imaging spectrometer 0.35-24μm, 12.5 nm, >200 S/N; minerals	Jim Head - Brown Univ., Ball Co., SETS Tech., Inc.	Global, 200-400 m/p Regional 80 m/p
Gravity, mGal level Doppler tracking	TBD by NRA; tracking signal spacecraft provided	Global

Scout I
- X-ray spectrometer
- NS
- High resolution stereo camera
- Gravity measurement system (Scout I and II)

Scout II
- Imaging spectrometer (MinMap)
- Ge GRS

Technical attributes of each instrument, particularly those that affect the spacecraft, are listed in table V with the exception of the BMDO LADAR altimeter.

TABLE V. TECHNICAL ATTRIBUTES OF THE INSTRUMENTS MANIFESTED ON LUNAR SCOUT I AND II

	MinMap	**Gamma Ray (Ge)- LANL**	**Neutron (3 sensors)**	**Hard X-ray**	**HRSC (DLR)**
MASS (Kg)	16	84.7	38.5	12	49
POWER (W)	35	53 (cooler 40)	14	22	67.5 Record 21.1 Playback 17 Stand-by
HEALTH & STATUS TELEMETRY (bps)	1000	18	18	16	18
DATA GATHERING PERIOD	± 45 Zenith	Continuous	Continuous	Sunlit Side	Sunlit Side
MAX DATA RATE (Kbps)	2000	7.4 Uncomp 1.1 Compressed	50.4 Unproc 1 Processed	5 Unprocessed 2 Processed	131 Kbps* Playback
DATA/ORBIT (Mbits)	3400	54 Uncomp 7.9 Compressed	363 Unprocessed 6.7 Processed	18 Unprocessed 7.2 Processed	1000
INSTRUMENT STORAGE (Mbits)		30	30	0	1000
ATTITUDE POINTING (mrad per axis)	8	85	85	34	4.7, 3 sigma
ATTITUDE K'LEDGE (mrad per axis)	4	48	48	17	1.7, 3 sigma
ATTITUDE STABILITY (mrad/sec)	0.1/0.15	48/20	48/20	None	.02/.002
VIEW FOV (Deg)	± 2.9	±45	± 50	10x10	38x12
ON-ORBIT CALIBRATIONS		10/year 1 Trans Lunar		Internal	Lunar Cals Only
SPECIAL RESTRICTIONS	Radiator FOV	Likes isolation	Likes isolation	Need detector Zenith pointing	Sun Keep out Zone
INSTRUMENT CMD INTERFACE	5 Hi-Level Disc. 1 Serial Digital	8 Bit Parallel	8 Bit Parallel	1 Serial Digital	Serial Digital, Relay
INSTRUMENT TLM INTERFACE	Serial Digital	16 Bit Parallel	16 Bit Parallel	Serial Digital	Serial Data, Analog
MECHANICAL ALIGNMENT (Deg)	0.5	1	1	1	0.03

* 131 kbps is the playback rate for the Mars '94 mission. The HRSC team planned to upgrade the playback rate to 1 mbps for lunar case.

Instrument Descriptions

X-ray Fluorescence Spectrometer

Jack Trombka, Principal Investigator (PI) - Goddard Space Flight Center (GSFC)

The objective of the X-ray experiment was to produce a global map of six major rock-forming elements: Si, Mg, Al, Ti, Ca, and Fe. The GSFC XRS is capable of accomplishing this objective at the spatial resolution necessary to understand many of the features observed on the lunar surface. Observation for one year greatly enhances the utility of the X-ray fluorescence (XRF) method in measuring major elements to a high precision. Properties of the XRS are shown in table VI.

TABLE VI. PHYSICAL CHARACTERISTICS OF THE X-RAY SPECTROMETER (XRS)

XRS Mass	
Sensor Head	5.0 kg
Central Elec. & Cabling	7.0 kg
Total XRS	12.0 kg
XRS Power	
Analog Processor	3.5 watts
Micro Computer	2.0 watts
Power Supply	1.7 watts
HVPS	0.8 watts
Total XRS	8.0 watts
XRS Dimensions	
Central Electronics	20.6 cm x 20.3 cm x 17.8 cm
Solar Sensor Head	16.2 cm x 7.0 cm x 6.9 cm
Lunar Sensor Assembly	17.0 cm x 14.0 cm x 21.0 cm

The XRF spectrometer selected consists of four gas proportional counters with an energy range of 0 to 10 keV. Energy resolution is 800 eV at 5.9 keV. All detectors have Be windows to reduce the coherent scatter in the lower part of the energy range. One detector acts as a solar monitor. The other three detectors look at the lunar surface. The detectors measure the abundances of Mg, Al, Si, Ca, Ti, and Fe. The detectors have differential filters to assist in the separation of Al, Si, and Mg lines. The differential filters have little or no effect on the Ca, Ti, and Fe lines. Error bars on measurements should range from 10% to 15% of the measured values.

The XRF spectrometer has a footprint approaching 10 km for Si on the lunar surface, assuming a spacecraft orbit of 100 km and XRF detectors with a 10° field of view. This orbital configuration

allows the equivalent of five or more re-encounters for a given area. Because of more extensive overlapping coverage and signal integration at higher latitudes, mapping is possible to within 10° to 20° of the poles.

X-rays are stimulated by solar activity. Periodic increases in solar activity will enhance spatial resolution. Calculations of XRF sensitivity use estimates of frequency and duration of solar activity based on observations made during solar minimum of the last two solar cycles. In reality, of course, the sun is extremely variable and only predictable in the most general way. Class B Subflare conditions can be expected to occur about 20% of the time; Class C Flares, about 4% of the time. Flares and subflares will most likely occur in clusters over periods of days, separated by three to four weeks. A model had been developed to calculate lunar surface XRF spectra under a variety of solar conditions and, in particular, under the conditions that may prevail during the Scout Program, circa 1995-96-97.

The X-ray emission is strongly dependent on the incident solar flare spectrum, as previously pointed out. The solar flare spectrum varies in intensity and in spectral shape. The differential energy spectrum falls sharply with increasing energy, and lower Z elements are excited more than high Z elements. With solar flare activity, the solar spectrum hardens, intensity increases, higher Z elements are excited and the spatial resolution improves for the lower Z elements. Given the spectrometer design to be employed, calculations were made to determine the time required to measure the abundances with a three-sigma accuracy for each of the six major elements. Table VII illustrates these calculations.

TABLE VII. XRF INTEGRATION TIMES FOR COMPOSITIONAL DETERMINATION

Apollo 16 Composition

Solar Condition	Mg	Al	Si	Ca	Ti	Fe
Low-Level Quiet	310 s	75 s	100 s	1 h	1500 h	130 h
Normal Quiet Sun	170 s	37 s	32 s	0.3 h	270 h	16 h
Subflare	37 s	7 s	6 s	82 s	22 h	2 h
Low-Level Flare	8 s	1 s	<1 s	2 s	500 s	19 s
High-Level Flare	2 s	<1 s	<1 s	<1 s	48 s	2 s

Apollo 12 Composition

Solar Condition	Mg	Al	Si	Ca	Ti	Fe
Low-Level Quiet	170 s	200 s	97 s	2 h	99 h	42 h
Normal Quiet Sun	97 s	98 s	30 s	0.5 h	19 h	5 h
Subflare	22 s	16 s	6 s	130 s	1.5 h	0.5 h
Low-Level Flare	5 s	3 s	<1 s	2 s	43 s	7 s
High-Level Flare	1 s	<1 s	<1 s	<1 s	4 s	<1 s

It is impossible to predict the spectrum, frequency, and duration of flare activity but, even during solar minimum, there is an average of one flare per day. The distribution is uneven and flares tend to occur

in clusters. Calculations indicate that there is a significant amount of time where observation can be made when there is solar activity that enhances the incident X-ray excitation flux.

The calculations show that Si will be routinely obtainable with a resolution of 10 km or better, Mg and Al with a resolution of 15 km, Ca with a resolution of 35 km, Fe with a resolution of 130 km, and Ti with a resolution of 210 km. But because of the occurrence of solar flares (Class C or above), one-third or more of the surface can be mapped at resolutions of better than 10 km for Mg, Al, Ca, and Fe, and 20 km for Ti.

This XRF experiment is considerably improved over the Apollo XRF experiment in the following ways:

- The extended energy range (0 to 10 keV compared to 1 to 2.5 keV) and improved energy resolution (800 eV at 5.9 keV compared to 1200 eV) of the detectors will allow inherently greater separation of all lines and detection of Fe, Ti, and Ca lines for the first time.

- The polar orbit will allow mapping of 90% of the lunar surface, as opposed to the 10% of the surface mapped in the past.

- The narrower field of view, combined with further integration between overlapping orbits, will allow inherently higher spatial resolution than the nominal 30-km resolution for Al and Mg obtained from the Apollo experiments.

- The one-year duration of the mission provides 365 days of signal integration compared to approximately three days for Apollo.

High Resolution Stereo Camera

Gerhard Neukum, PI - German Aerospace Research Establishment (DLR)

The HRSC is a planetary imaging system developed by the German Space Agency (DARA) and the German Aerospace Research Establishment for the Russian Mars '94 and Mars '96 missions. The same instrument, virtually unmodified, is ideal for imaging the Moon for production of a geodetic map and stereo imagery of the highest quality over the entire Moon.

The HRSC consists of a camera system and a mass memory system. The camera has one objective lens (focal length = 175 mm, f/5.6 as configured for Mars), nine spectral filters, and three focal plate modules. The focal plate modules have three charge-coupled-devices (CCD), each for a total of nine CCDs. Each CCD (Thomson THX 7808) has 5200 7 x 7 micron pixels, of which 5184 are active. Each focal plate module is separately adjustable with respect to the objective lens. All CCDs are active simultaneously. There is significant capability for on-board parameter selection. Compression is on board and selectable with a ratio from 2 to 20:1.

The HRSC operates in the "push broom" line scanner mode as shown in figure 5. One focal plate array is forward-looking, one is nadir-pointing, and the third is aft-looking. The forward-looking focal plate module CCDs are dedicated to stereo, infrared (970 nm) and photometry (675 nm); the nadir module CCDs are sensitive in the blue (440 nm), green (530 nm), and visible (675 nm); and the aft-looking module has stereo, purple (750 nm), and photometry (675 nm). The stereo convergence angle is 18.9°.

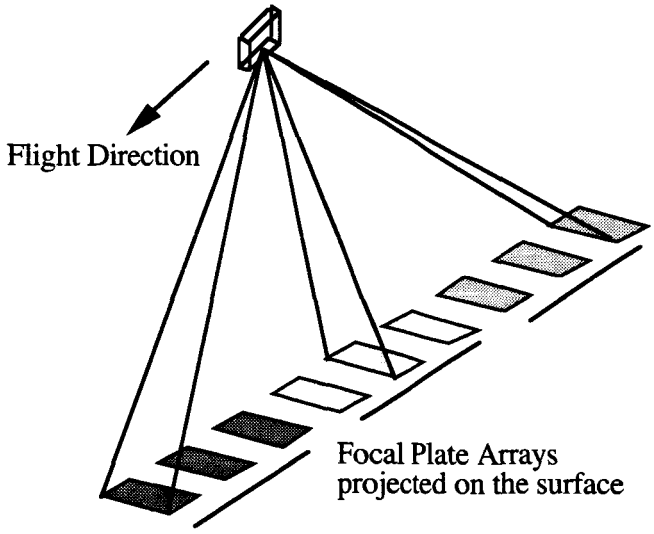

Figure 5. Geometry of the HRSC focal plate arrays relative to the imaged surface.

The single objective lens for the three focal plate arrays is a technological step forward. The lens parameters provide an instantaneous field of view (IFOV) of 46 μrad resulting in, for example, a swath width of 41 km at 100-km altitude. The camera characteristics, plus a downlink rate of 1Mbps, allow full global coverage to be achieved in a one-month mapping program. In the lunar case, the camera system is capable of 8 m/p resolution from an altitude of 200 km and 4 m/p from an altitude of 100 km.

The mass memory unit has a maximum capability of 2 Gbit and a net of 1 Gbit storage. A high degree of on-board data manipulation is available, e.g., compression ranging from 2:1 to 20:1, pixel summing, and parameter selection. The flexibility has major advantages when combining the HRSC with other instruments that may compete for data rates and data storage. Camera physical characteristics are shown in table VIII.

The HRSC can produce a Digital Image Model (stereo), and the data can be used for generation of a global lunar geodetic net. Digital stereo imagery resolution, meters per pixel (m/p), is a function of altitude (nominally 4 m/p at 100 km). The Scout I mapping plan called for 20 m/p global mapping at an altitude of 300 km, and regional and local stereo imagery of regions and sites of interest to the exploration and science community at a resolution of 4 m/p from an orbit altitude of 100 km.

The HRSC could produce a global geodetic net with 50-m latitude and longitude control and 50-m elevation control as a worst case (no altimetry, no ground control points, and worst case tracking). New algorithms developed by the German aerospace and university communities simplify data reduction with a concomitant improvement in precision. These algorithms have been proven in the MOMS/D2 experiment flown by DARA on the STS-55 flight in the spring of 1993. (See Photogrammetry.)

TABLE VIII. HRSC PHYSICAL CHARACTERISTICS

Unit	Mass (kg)	Power/Mode Standby (MM)	Imaging	Trans	MM Normal
Camera					
Camera Head	11.1	-	10.62	-	
Digital Unit	11.4	-	23.3	-	
Harness (Internal)	0.5				
Thermal H/W	1.0				
Total Camera	24.0		33.9		
Memory System					
Telemetry Controller	10.2	9.6	15.7	10.2	13.9
Memory Unit	14.8	7	11.8	7.2	7.2
Total System	25.0	16.6	27.5	--	21.10
Total	49.0	16.6	67.5	17.4	21.10
Dimensions					
Camera	262 x 707 x 280 mm				
Memory System					
Camera Sensor Parameters					
FOV					
x-track	12°				
along track	38°				
Entrance Pupil	3.125 cm				
Focal Length	175 mm (f/5.6)				
Stereo convergence	18.9°				
Pixel size (IFOV)	7μ (40μrad)				
Pointing and stability budget:					
Pointing accuracy (real-time)	± 10.5 mrad per axis, 3σ				
Pointing stability (real-time)	± 0.02 °/s (0.035 mrad in 0.1 s)				
Frequency of attitude corrections	≤ 0.1 Hz				
Pointing knowledge (post processing)					
Absolute	± 1.7 mrad per axis				
Relative within 20 s interval	± 0.01 mrad per axis				

LANL Neutron Spectrometer

George Auchampaugh, PI - LANL

The LANL NS measures fast and slow (epithermal and thermal) neutrons in the ranges of 0.5 MeV to 25 MeV and 0.01 eV to more than 1 keV, respectively (assuming counting for approximately 11 months at an altitude of 100 km). The NS consists of two assemblies, a fast neutron sensor and two proportional counters for thermal and epithermal neutron measurements. The field of view of the spectrometer is 50°. Physical parameters are listed in table IX.

TABLE IX. PHYSICAL CHARACTERISTICS OF THE NEUTRON SPECTROMETER

Unit	Mass (kg)	Power (w)
Fast Neutron Spectrometer Envelope: 54.2 x 51.6 x 51.6 cm	27.6	TBD
Thermal/Epithermal Spectrometers Envelope: 50.8 x 38.1 x 33.02 cm	10.9	TBD
Totals	38.5 kg	14 w (average)

The fast neutron sensor consists of four borated plastic scintillator rods, optically coupled to photomultiplier tubes. Calculations show that in this configuration the data can be corrected for spacecraft neutron background, thereby eliminating the need for a boom. This assemblage has previous flight heritage as the Army Background Explorer (ABE) instrument. ABE was deeded to LANL by the U. S. Army for the Lunar Scout Program. This significantly reduced cost and had a positive impact on schedule risk.

Thermal and epithermal neutrons are measured with ^{3}He gas proportional counters. The thermal neutron proportional counter is wrapped with tin; and the epithermal proportional counter, wrapped with cadmium. Similar counters have extensive flight heritage in Earth orbit.

The sensitivity of the NS and its spectral range would have significantly reduced ambiguities in the interpretation of the gamma ray data that would have been obtained by Lunar ScoutII. Conversely, full interpretation of neutron flux data requires knowledge of the bulk regolith composition, supplied by the GRS. This synergism between the neutron and gamma ray measurements leads to a greater confidence in the concentration levels and distributions of volatiles in the lunar regolith and in the concentrations derived from the gamma ray data.

The NS sensitivity would allow the determination of H abundances below the 100-ppm level to a depth of 150 g/cm^2 (the top 60 cm of regolith), providing maps of volatile concentrations (extrapolated from H abundances) and of regolith maturity. Lunar Scout I was to be placed in a polar orbit, thereby allowing a survey of the polar regions where high concentrations of volatiles, including water ice, may occur in permanently shadowed areas.

LANL Ge Gamma Ray Spectrometer

Cal Moss, PI - LANL

The GRS was to be equipped with a 70% efficient n-type Ge crystal detector cooled to 80 K with twin mechanical cryocoolers. The design included secondary and backup sensors consisting of a CsI shield around the Ge detector and two photomultiplier tubes plus assemblies to form an anticoincidence shield for the detector. These shield elements eliminate the need for a boom and provide Apollo gamma ray instrument equivalent data in the event of a Ge failure. Resolution of the Ge system is 1.8 keV at 1.33 MeV, and the range is 50 keV to 10 MeV. Footprint is 100 to 140 km. The spectrometer will operate for a year in lunar orbit, with approximately 11 months at 100-km altitude. Field of view is 45°.

A global survey can be completed in one month, and one-year operation provides the integration time necessary for high precision. Physical characteristics are listed in table X.

TABLE X. PHYSICAL CHARACTERISTICS OF THE GAMMA RAY SPECTROMETER

Unit	Mass (kg)	Power (W)
Ge Sensor Assembly	62.9	8
Cooler & Electronics	21.8	45
Totals	84.7	53
Envelope:	87.6 x 71.9 x 79.2 cm (Total Instrument Envelope)	
	40.6 x 38 x 58.4 cm (Sensor Assembly - included in above)	

The resolution and spectral range are unprecedented for an interplanetary GRS, allowing it to map the following elements at the detection limits specified for a 10-hour integration time:

H	0.05%	O	0.68%	Na	0.20%
Mg	0.33%	Al	0.58%*	Si	0.31%
S	0.5%	Ca	1.3%	Ti	0.11%
Mn	0.12%	Fe	0.26%	K	32 ppm
U	0.016 ppm	Th	0.043 ppm	Sm	12 ppm
Gd	19 ppm				

*If no interference from spacecraft.

Precision is at the percentage level or better of the amount present. The GRS data was to be complemented by NS data. Data of this extraordinary quality for the entire Moon would provide the means to distinguish the known lunar rock types and geological units and discover new ones.

The actively cooled GRS represents the first time that a Ge detector, cooled to its optimum operating temperature, was selected to fly and function for a one-year mission in deep space. This technological breakthrough was made possible by recent advances in active cooler technology by industry, demonstration through flight experience of the maturity of the technology ISAMS satellite, and the elimination of microphonics problems through careful experiment design.

Imaging Spectrometer (MinMap)

Jim Head, PI - Brown University (team includes SETS Technology and Ball Aerospace)

The imaging spectrometer, known as MinMap, was developed by Brown University, Ball Aerospace, and SETS Technology to provide global mineralogical mapping. MinMap is a hyperspectral grating-type imaging system with a spectral range of 0.35 to 2.4 microns. The system uses two detectors to cover this spectral range: a silicon charge-coupled-device (Si CCD) for visible imaging from 0.35 to

0.95 microns, and a mercury-cadmium-telluride (HgCdTe) CCD for the infrared from 0.9 to 2.4 microns. The two detectors have sufficient spectral overlap to allow photometric cross-calibration. The Si CCD will operate at a nominal temperature of 300 K with a maximum readout rate of 160 kHz, read noise of approximately 10 e^- per pixel, and a dark current of 1800 e^-/s. The HgCdTe CCD is passively cooled to a temperature of 140 K with a maximum readout rate of 320 kHz, read noise of approximately 400 e^- per pixel, and a dark current of 100 000 e^-/s. Both detectors are anticipated to have a signal-to-noise ratio in excess of 200 for nominal lighting and albedo conditions. The number of spectral channels and their bandwidths is selectable and, as in the case of the HRSC, the specific experiment strategy is driven by global requirements and spacecraft constraints. Characteristics of the spectrometer are shown in table XI.

TABLE XI. MINMAP PHYSICAL CHARACTERISTICS

Mass	16 kg
Power	≤ 35 W
Dimensions	
Radiator	44 x 15 x 20 cm
Sensor Assembly	34 x 9 x 11 cm
Electronics	25 x 25 x 20 cm
FOV	5.8 deg
IFOV (Pixel Size)	24 μm (400 μrad)
Entrance Pupil	1.8 cm
Focal Length	6 cm (f/3.3)

The spectral and spatial data form an image cube consisting of 256 spatial channels, each with an associated 192 spectral channels (figure 6). Spatial resolution is a function of orbit altitude (at 450 km, pixel size is 180 m; and at 100 km, pixel size is 80 m). A global mineralogical map could be produced at a high orbital altitude in approximately one month, given Lunar Scout II characteristics and limiting the spectral channels to approximately 100. Regional and local maps of selected targets, of as much as 26% of the Moon, could be produced at the 80-m pixel level over the full spectral range at a lower altitude with a 1Mbps downlink rate over a period of 10 months.

The hyperspectral (> 100 channels) character of the MinMap instrument will allow the characterization of major rock types by determining composition and relative abundance of the major rock-forming minerals (e.g., ortho- and clinopyroxene, olivine, plagioclase, plus phases such as glass). The data will also provide a measure of the maturity of the regolith and of the TiO_2 abundance in the soils. If hydrous alteration species occur on the surface, MinMap will be able to detect and map them.

MinMap mineral modal data combined with XRS elemental maps, of approximately the same scale (10kms), would allow correlation between the two and extrapolation to the much more complete elemental mapping that can be produced by a GRS. The combined results can produce a complete chemical and mineralogical characterization of lunar surface units.

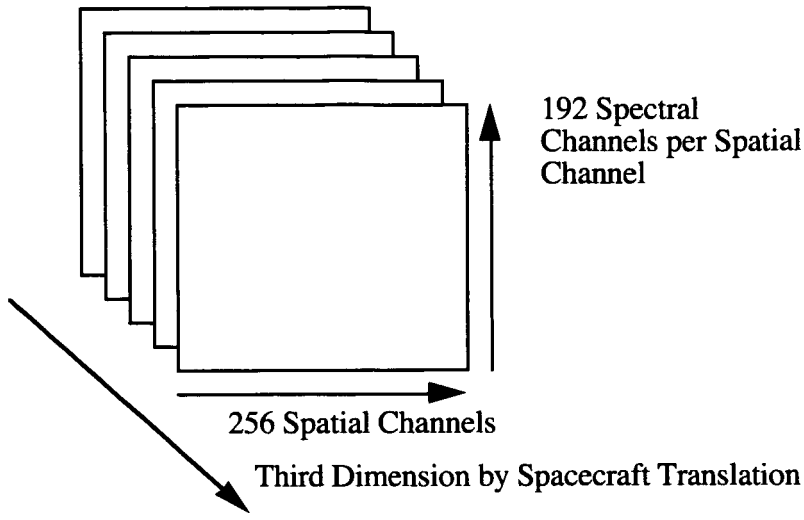

Figure 6. Image cube geometry of MinMap. Spatial and spectral channels are co-registered. Given the parameters shown in table XI, swath width at 500 km is 48.8 km and the spatial resolution is 200 m/p. Because of spacecraft memory limitations, not all spectral and spatial channels could be used in the global mapping phase of the Scout II mission, whereas all channels were to be used in the regional mapping phase.

Gravity experiment

Measurement of the gravity field of the Moon has a high science priority because of its implications for the internal structure and thermal history of the Moon. This measurement had a high priority for the Space Exploration Initiative because of the influence of lunar gravity on spacecraft navigation and orbit maintenance. A minimum Doppler measurement accuracy of 0.5 mm/sec is required for science purposes. This accuracy will satisfy requirements for spacecraft navigation expressed as spacecraft position error propagation with time.

The gravity field of the Moon was to be mapped during the Scout Program using a two-spacecraft concept. In the two-spacecraft concept, one spacecraft is placed in a high-altitude eccentric orbit with a nominal apolune of 7000 km while the second spacecraft is in a low-altitude polar orbit. The spacecraft in elliptical orbit serves as a relay while the low-altitude spacecraft is in a quiescent mode and responding to the lunar gravity field.

The gravity experiment requires a radio frequency that will permit one-way Doppler tracking between the spacecraft. Both spacecraft carry NASA standard transponder systems for data transmission to Earth, as well as for tracking and orbit determination. The telecommunications systems of the low orbit spacecraft is modified to accommodate an ultrastable oscillator to provide a stable reference frequency. Consequently, it serves as a radio frequency beacon that can be tracked by either the high altitude spacecraft (which relays data to Earth) or by Earth directly. Use of the Deep Space Network (DSN) 34-m antenna permits a Doppler measurement accuracy of 0.3 mm/sec for the 34-m standard antenna or

0.1mm/sec for the 34-m HEF antennas. A gravity field map could be produced within two months with this system.

The nominal Scout Program plan for a global gravity map called for Lunar Scout II to be placed in an elliptical orbit at the beginning of its mission to serve as the relay while Lunar Scout I was in a quiescent mode at 100-km altitude, after completing its mapping phase. Lunar Scout I was to be equipped with an ultrastable oscillator and tracked. (DSN tracking of Lunar Scout I during its low-altitude orbit would provide an initial gravity map of the Moon. Substantial improvements in the lunar gravity model can be obtained by this method.) Full scale global mapping with the high precision achievable with the two-spacecraft concept would have been completed during the flight of Lunar Scout II.

A possible alternative is the utilization of a spacecraft subsatellite released by a parent-orbiting spacecraft and subsequently tracked. The changes in the relative distances between the two spacecraft as the Moon is orbited provide a precise measurement of the lunar gravity field. The implications of this alternative scheme were examined by the CS Draper Laboratories. (See Mission Studies and Appendixes.)

Ballistic Missile Defense Organization (BMDO) LADAR

The accurate reconstruction of the spacecraft ephemeris is extremely important for gravity measurements and for photogrammetry. An altimeter is a useful tool for determining the ephemeris, and the data can be converted directly into topographic profiles of the lunar surface. The Lunar Scout Program initiated successful discussions with the BMDO concerning flying the Laurence Livermore National Laboratory (LLNL)/LADAR of the type manifested on the CLEMENTINE mission. Technical aspects of the altimeter are shown below in table XII. The framing camera was not considered as part of the Scout payload. The altimeter data plus the gravity tracking data would have been supplied to a PI for gravity, chosen competitively via a NASA Research Announcement.

TABLE XII. BMDO LADAR ALTIMETER CHARACTERISTICS

Beam divergence	=	0.5 mrad
Spot Diameter	=	300 m at 300 km, 100 m at 100 km
1 Hz pulse spacing on surface	=	1.32 km @ 300 km, 1.54 km @ 100 km
Energy per puls	=	175 mJ
Wave length	=	1.06 μ
Bandpass	=	5 nm FWHM
Detector IFOV	=	5 mrad
Collection aperture	=	13 cmϕ
Gating time	=	30 nsec
Detector APD, 50x gain at 0.1 albedo		
Background signal	=	10 500 pe^-
Return Signal	=	18 500 pe^-
Threshold	=	18 500 pe^-
Probability of correct ranging	=	99.9+%
PWR $\leq$ 14W @ 1 Hz in full ranging/imaging, including framing camera power		
Mass < 5 kg		

Mapping Strategies

Introduction

Mapping strategies for Lunar Scouts I and II were driven by global coverage requirements for the HRSC on Scout I and MinMap on Scout II, and by the requirement for measuring the lunar gravity field using both spacecraft early in the flight of Scout II.

Lunar Scout I

A nominal mission scenario for the global mapping phase of Lunar Scout I, involving the HRSC, was derived from consideration of the following constraints:

- Provide gore-free, global three-axis stereo imagery
- 1 Gbit of onboard mass memory available
- 1Mbps of downlink capacity
- 10% equatorial sidelap, 1% minimum, per swath to ensure gore-free coverage
- No downlink during data collection, and one-minute DSN acquire/release time

Given these constraints and the parameters of the HRSC, absolute pointing and orbit plane tolerances were derived. Appendix C is a method for specifying attitude control requirements.

Global Mapping Strategy

The 10% equatorial sidelap constraint leads to the swath width possibilities in km and pixels shown in figures 7 and 8. The HRSC has a maximum of 5284 active pixels; therefore, the minimum altitude for global coverage is 188 km.

The swath length is determined by the highest latitudes that can be skipped on successive passes while maintaining 10% sidelap at the equator. Figure 9 illustrates swath length and shows that latitudes 60° S to 60° N must be covered on every pass. A swath length of 150° or 4551 km, therefore, is necessary (e.g., 90° N to 60° S/60° N to 90° S) to maintain the required sidelap. The swath length thus dictates data storage requirements (assuming the maximum downlink rate).

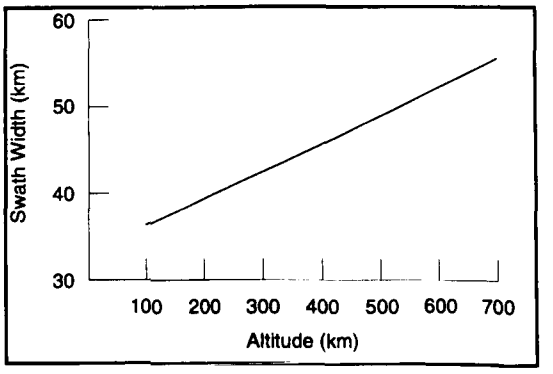

Figure 7. Swath width in kilometers as a function of orbit altitude.

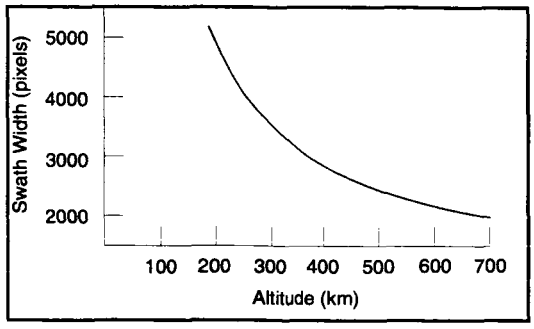

Figure 8. Swath width in pixels as a function of spacecraft altitude. The HRSC has 5284 active pixels with 7μ spacing and an IFOV of 40μrad. (Other HRSC parameters are shown in table VIII.)

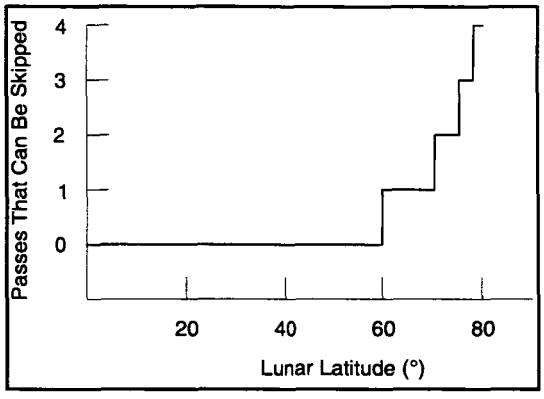

Figure 9. Swath length for the HRSC. At greater than 60° latitude, successive passes can be skipped and still achieve global coverage, given the swath width of the HRSC and the requirement to maintain a minimum of 1° sidelap.

The total data load for the global mapping scenario is calculated using the relevant HRSC parameters, namely:

Camera pixel resolution	40μrad
Pixel binning options	1, 2, 4, 8
Compression ratio	10:1 (up to 20:1 is possible)
Analog to digital conversion	8 bits/pixel
Distance between sensor lines (s)	60.2 mm

For a given altitude, the binning options (1, 2, 4, 8) are selected so that the total data accumulated for both nadir and stereo channels do not exceed the 1 Gbit storage constraint. (For this calculation, six channels—color and photometry on the three focal plate arrays—were not considered. They could be included if sufficient margin were available at the actual flight altitude.) Binning options have spatial resolution consequences, and a trade-off must be made between binning option and resolution. This trade-off dictates mission strategy.

The maximum downlink achievable (within the 1Mbps) is determined by the worst case geometry of the spacecraft relative to the DSN when the spacecraft and DSN are in the same plane. This case and a feasible strategy is illustrated in figure 10. Given the swath length, it is possible to begin Orbit1 mapping at 60° N and continue data collecting to 90° S. At the selected altitude, a certain amount of time is available for downlink because the spacecraft remains within view of the DSN until loss of signal occurs as it goes behind the Moon. The mass memory is downlinked and prepared for the next pass during this period. One minute is allowed for signal release. Orbit 2 then begins mapping at 90° N and continues to 60° S, where downlink begins and preparation is made for the next orbit, which begins mapping at 60° N and follows the sequence of Orbit 1. The orbit illustrated is 300 km, which allows 11 minutes for downlink.

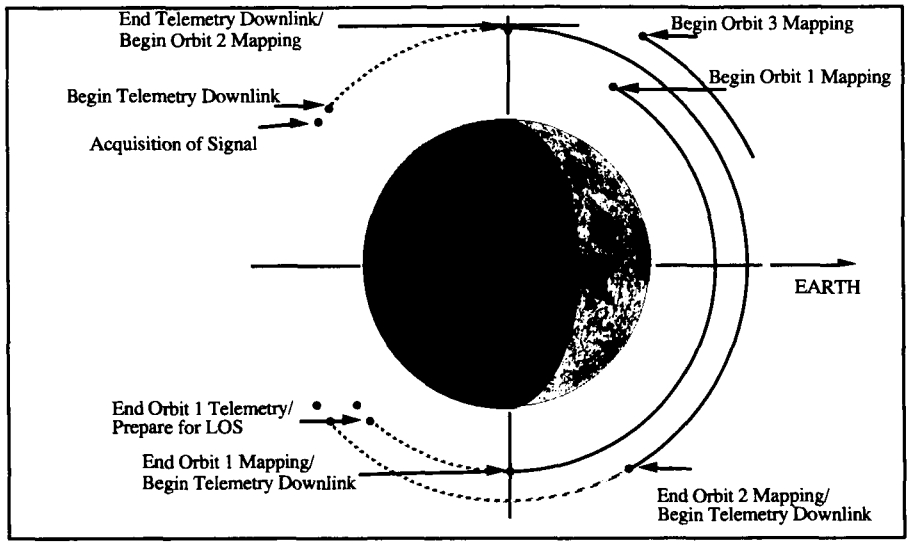

Figure 10. Data collection and downlink strategy for the HRSC.

These considerations lead to the strategy illustrated in figure 11 and listed in table XIII. The nominal scenario meets the following constraints and criteria:

- Data storage
- Downlink constraint
- Highest nadir and highest stereo resolution
- 10° tolerance in altitude
- Minimum Altitude: swath width ratio

It is possible to achieve global stereo imagery in one month with this strategy, primarily because of the 1Mbps downlink capability of the DSN that is to be on line in the mid-1990s. The strategy, based on data rates, is linked with Sun angle and the requirements of other instruments in developing a mission plan.

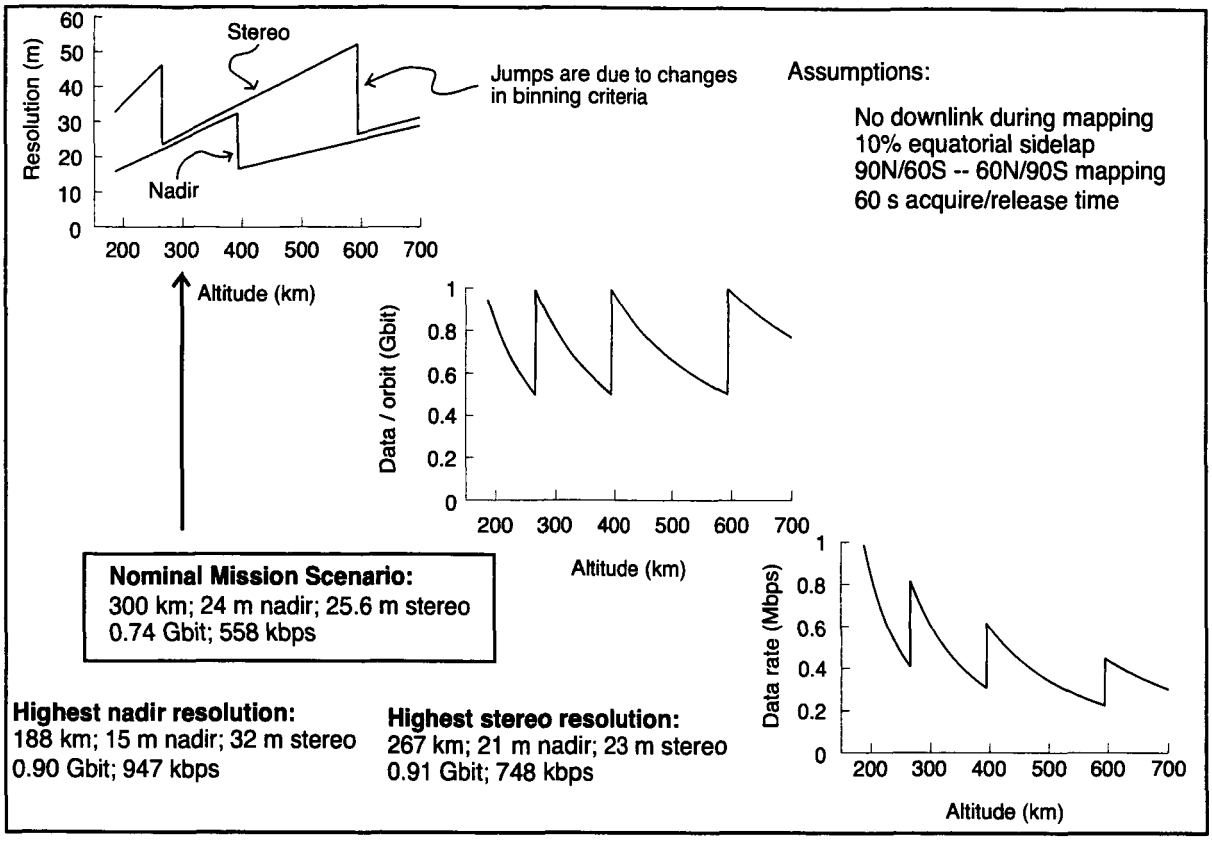

Figure 11. Global imaging strategy based on a data storage constrained scenario.

TABLE XIII. NOMINAL MAPPING STRATEGY FOR GLOBAL MAPPING BY THE HRSC ON LUNAR SCOUT I

Nominal orbital altitude	300 km
Number of active line sensors	3
Nadir/stereo resolution	24 m/25.6 m
Data per orbit	0.74 Gbit
Downlink	558 kbps
Swath length	4551 km (90N-60S/60N-90S)
Swath width	42.4 km (3536 pixels binned by 2)
Stereo base length	103.8 km (18.9°)
Altitude tolerance	30 km
Pointing tolerance	0.37°
Orbit plane tolerance	0.64°

Once the nominal altitude is selected, 300 km for global mapping as shown in table XIII, tolerances for both absolute pointing and orbit inclination can be determined to assure gore-free coverage. Pointing deviation is calculated assuming worst case geometry with a 1° sidelap tolerance. Orbit inclination (deviation from a polar orbit) is calculated assuming a 10° polar overlap tolerance. The derived tolerances are shown in figure 12. See also appendix C.

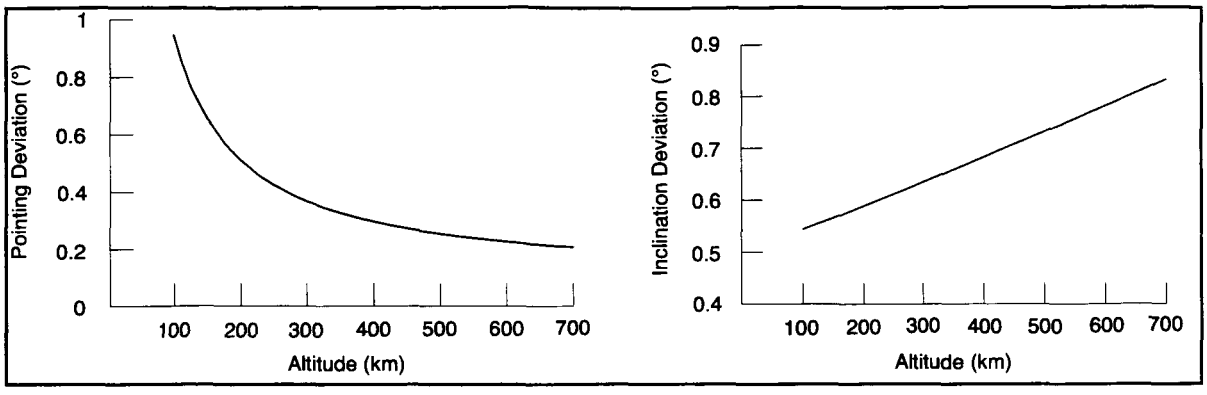

Figure 12. Derived pointing and orbit inclination tolerances, given the mission scenario shown in table XIII for global stereo mapping by the HRSC.

Downlink Constrained Mapping Strategy

As noted, the mapping strategy for the HRSC is based on a data storage limit of 1 Gbit and the downlink rate of 1Mbps. If the storage constraint is relaxed so that data can be collected to the limit that can be downlinked at high altitudes (nominally ~ 300 km) and at 100 km and a rate of 1Mbps, then it is possible to map at higher global resolutions and to cover a higher percent of the Moon during the low altitude mapping phase. A higher resolution is possible for the global mapping because fewer pixels need to be binned and there is inherently higher resolution.

Figure 13 illustrates the trade-offs in the data rate limited case—where data storage is not an issue. In this case, the nominal global mapping altitude that would be selected is 240 km to maximize resolution of both nadir and stereo channels at about 20 m/p. Highest resolution is obtained at an altitude of 295 km for the nadir CCD (with 20% overlap for stereo per swath), but the stereo CCD channels would have a resolution of 25 m/p. Total data storage for the selected option is 1.33 Gbit. A 30% increase in storage capacity results in a very significant increase in capability.

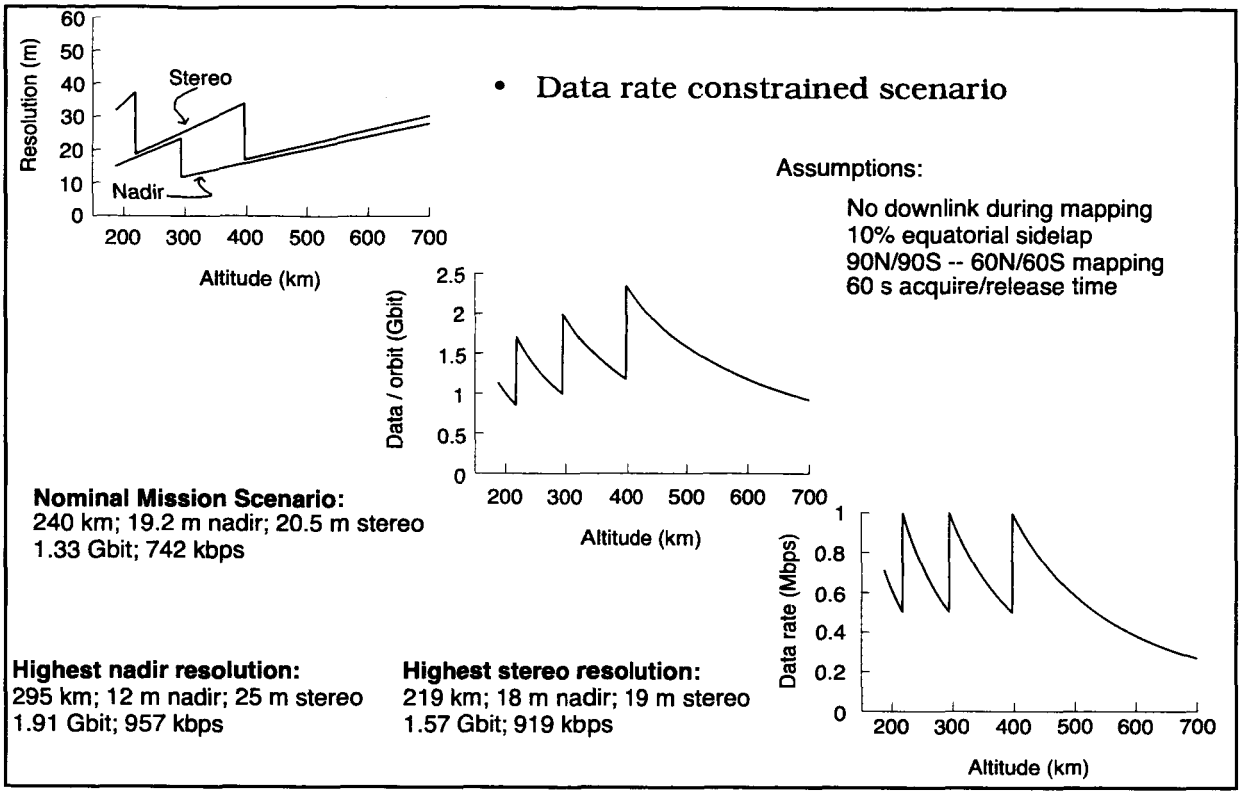

Figure 13. Improvements in global resolution are significant with a small increase in storage capacity. The nominal strategy represents an equalization of nadir and stereo imagery resolution. An alternative is to bin the stereo CCD data a factor of two and not bin the nadir channel. This strategy maximizes the nadir pointing CCD resolution and would result in 20% global stereo (at the equator) and 100% stereo at latitudes greater than 60° N or S. The highest stereo resolution is achieved in a similar way by binning the nadir CCD and not binning pixels for the fore and aft stereo CCDs.

Regional Mapping Strategy

High-resolution imagery of selected regions on the Moon is possible after collecting the global data. The nominal strategy selected for the low altitude mapping phase is shown in table XIV. An altitude of 100 km was selected to provide adequate high-resolution stereo imagery resolution (4m/p), while minimizing the delta-V required for orbit maintenance. Having selected the altitude, the mapping strategy is then constrained by data storage and downlink capabilities. As is shown in table XIV, 26% of the Moon can be mapped in stereo at a resolution of 4 m/p. Data per swath length is 0.94 Gbit, near the limit of 1 Gbit storage. Increasing storage capacity increases the percent of the Moon that can be mapped at high resolution. Increased storage (say, to 2 Gbit) is a viable option for the HRSC.

TABLE XIV. REGIONAL MAPPING STRATEGY PARAMETERS FOR THE HRSC ON LUNAR SCOUT I

Altitude	100 km
Nadir/stereo resolution	4 m/4.24 m
Color/photometry resolution	16 m
Swath width	20.74 km
Swath length	172 km (111 s)
Compression	6:1
Data / swath	**0.94 Gbit**
Data rate	8417 kbps
Stereo base	34.4 km
Number of swaths/orbit	1
Number of swaths/mission	2782
Lunar surface coverage	26%

Cumulative Data Load

The total data load for Scout I for imaging for the storage constrained global and regional mapping strategies is shown in table XV. For the data rate constrained strategy, the total data load increases by about 30%.

The data load added by the NS and the XRS are minor additions to the total data load.

TABLE XV. CUMULATIVE DATA LOAD PRODUCED BY THE HRSC, SCOUT I, EXCLUDING PHOTOMETRY AND COLOR CHANNELS

Mode	Months	Passes	Data (Gbytes)
Global mapping	1	286	30.0
Regional mapping	8.3	2782	325.5
Total			**355.5**

Lunar Scout II

A global and regional (high-resolution) mapping strategy was developed for MinMap. The strategy was dictated by the requirement to achieve global coverage before implementation of its high-resolution mapping phase, and by data storage and data downlink capability.

The following constraints were considered in developing a global mapping strategy for MinMap. Absolute pointing and orbit plane tolerances were derived from these requirements.

- Global coverage at an acceptable resolution to satisfy science requirements
- 1 Gbit of mass memory available
- 10% sidelap with 1% minimum per swath
- 1Mbps maximum science data downlink
- Real-time data collection and downlink capability during acquisition of signal (AOS)
- 1 minute DSN signal acquire/release time at the beginning and end of loss of signal (LOS)

The following instrument characteristics were used in calculations:

Field of view	5.8°
IFOV (pixel size)	24μm (400μrad)
Entrance Pupil	1.8 cm
Focal Length	6 cm (f/3.3)
Pixel binning options	1, 2
Compression ratio	2:1
Analog to digital conversion (ADC)	12 bits per pixel

Global Mapping Phase

The orbit altitude required for global mapping is a function of the mission requirements and the spectrometer's capabilities. The 10% equatorial sidelap requirement leads to the swath width shown in figure 14. MinMap has a maximum of 256 pixels; therefore, as is illustrated in the figure, the minimum altitude for global coverage is 465 km.

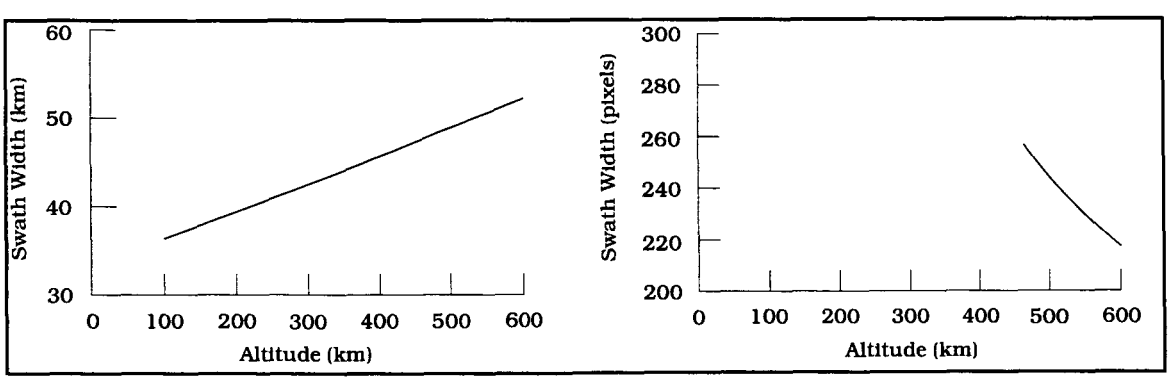

Figure 14. Swath width in kilometers and in pixels as a function of orbit altitude. The spectrometer had a maximum of 256 pixels, therefore, 465 km is the minimum altitude for global coverage while maintaining 10% sidelap coverage.

Swath length is determined by the highest altitudes that can be skipped on successive orbits and still maintain 10% sidelap at the equator. Swath length given this constraint is shown in figure 15.

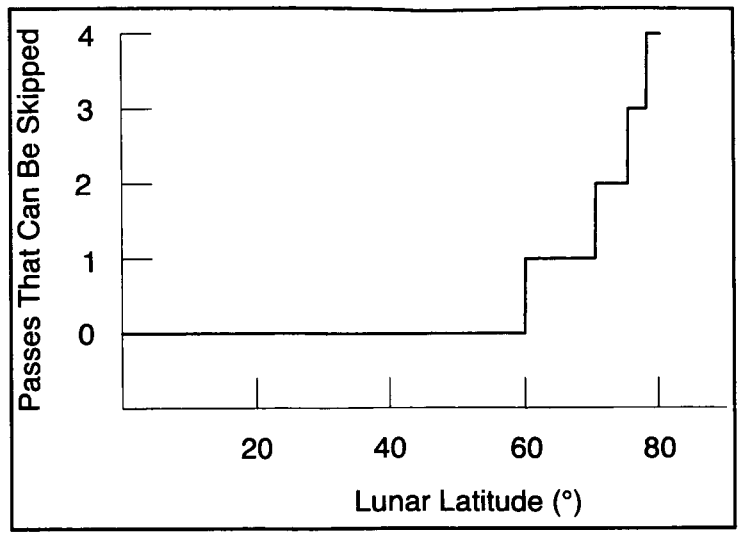

Figure 15. Swath length as determined by the requirement to have 10% sidelap at the equator.

As is illustrated in figure 15, 60° S to 60° N must be covered on every orbit in the global mapping phase of Lunar Scout II. The polar latitudes at greater than 60° can be covered on every other orbit. A swath length of 150° (4551 km) or, for example, 90° N to 60° S/60° S to 90° N, is necessary. The maximum spatial and spectral resolution that can be achieved is determined by downlink capacity when the spacecraft is in view of DSN (AOS case), and by storage capacity (1Gbit) for the part of the lunar far side measured when the spacecraft is out of view (LOS case) of the DSN. This situation is illustrated in figure 16 for the worst case when the spacecraft and the DSN are in the same plane.

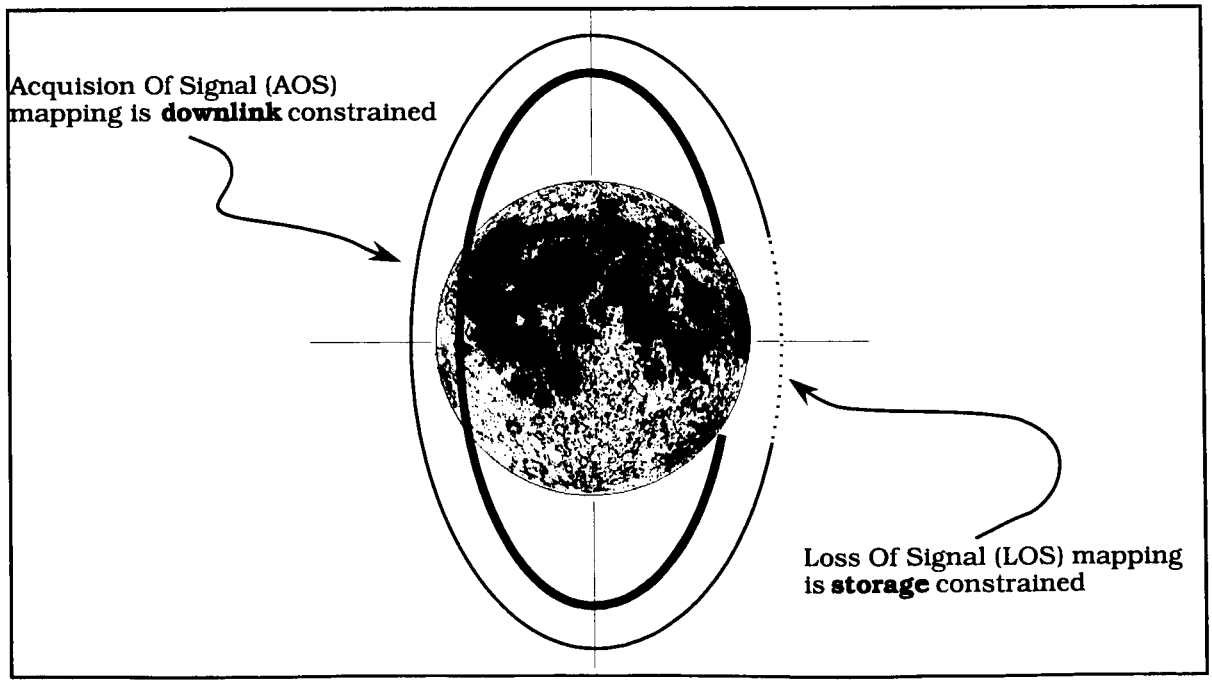

Figure 16. AOS and LOS determine maximum spatial and spectral resolution that is achievable for global mapping given mission and spectrometer capabilities.

The downlink constraint is 1Mbps. The number of spectral channels versus spatial channels satisfying the downlink constraint is computed for AOS mapping—when the spacecraft is in full view of DSN. Once the orbit altitude and the number of spectral channels are chosen for the AOS phase (with real-time downlink during AOS mapping), the number of spatial pixels that must be binned to meet the data storage constraint for LOS mapping can be calculated.

The AOS scenario is illustrated in figure 17. The driving assumption is real-time downlink of data collected. The nominal scenario that is selected results in a 500-km orbit, 110 spectral channels instead of the maximum possible of 192, and a spatial resolution of 200 m/p. These data would form a 110 x 265 pixel image cube. The downlink rate of 926 kbps is near the maximum. As is illustrated in the figure, it is possible to acquire the full spectrum of 192 channels of MinMap at an orbit altitude of 636 km but at a decrease in spatial resolution.

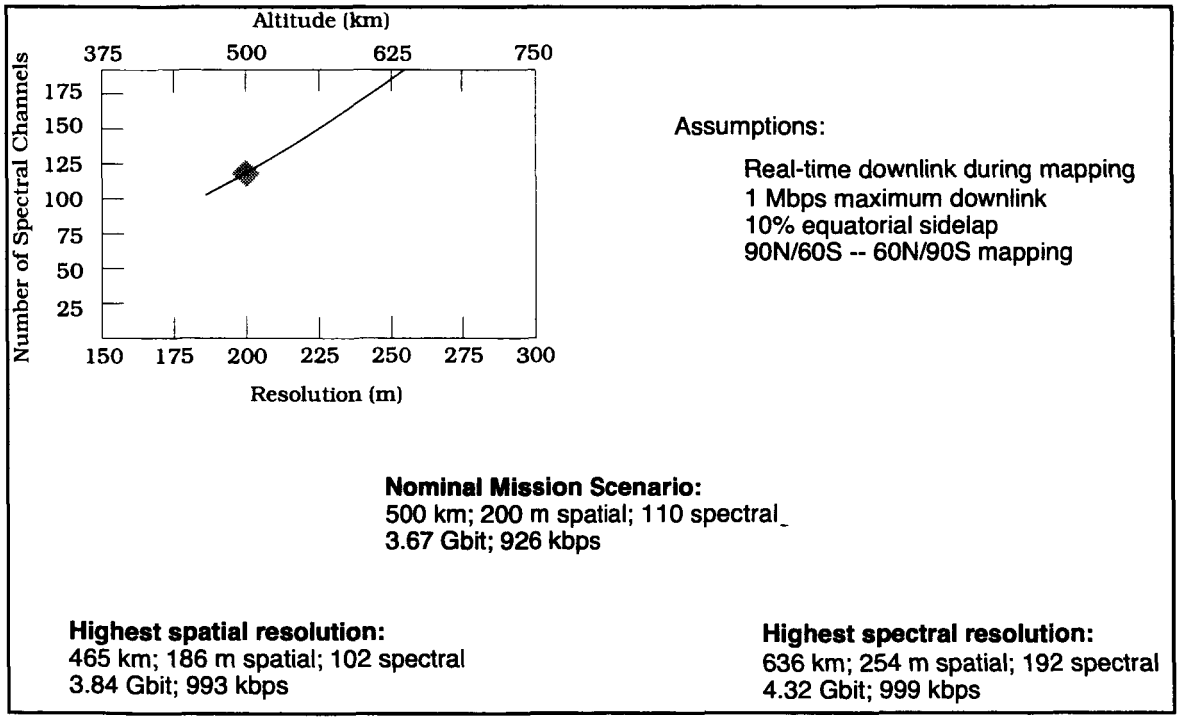

Figure 17. AOS mapping scenario for MinMap.

Far-side mapping is storage dependent but, at an altitude of 500 km, the spacecraft is in view of the DSN while surveying a significant fraction of the far side. This leads to a mixed-mission scenario wherein a large fraction of the far side can be mapped using real-time downlink; a smaller fraction must be mapped using the data storage capacity and selecting a pixel-binning option that represents a trade-off between spectral and spatial resolution. The fraction of the Moon that is imaged at the reduced rate, as a consequence of data storage limits, is illustrated in figure 18.

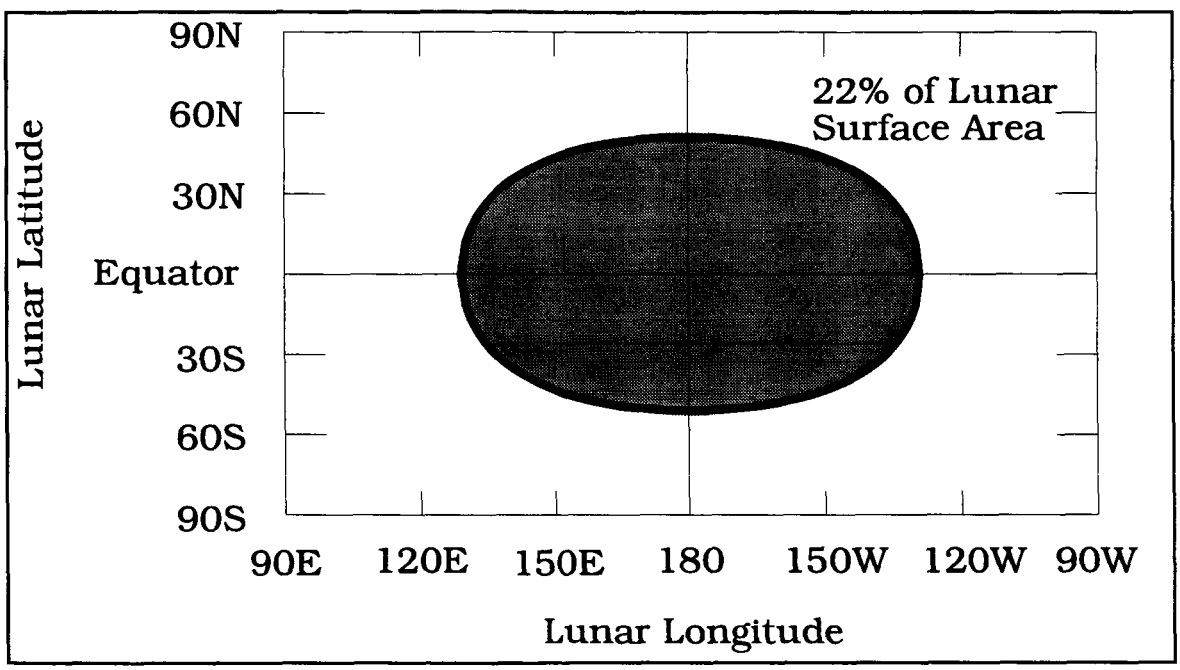

Figure 18. 22% of the Moon must be imaged at a reduced rate from an altitude of 500 km. The latitude and longitude of this area is shown. Data must be stored when above these coordinates because of LOS. A mixed-mission scenario—downlink/store/downlink—results in maximum spectral return from the far side.

The mapping strategy scenario for the far side is shown in figure 19.

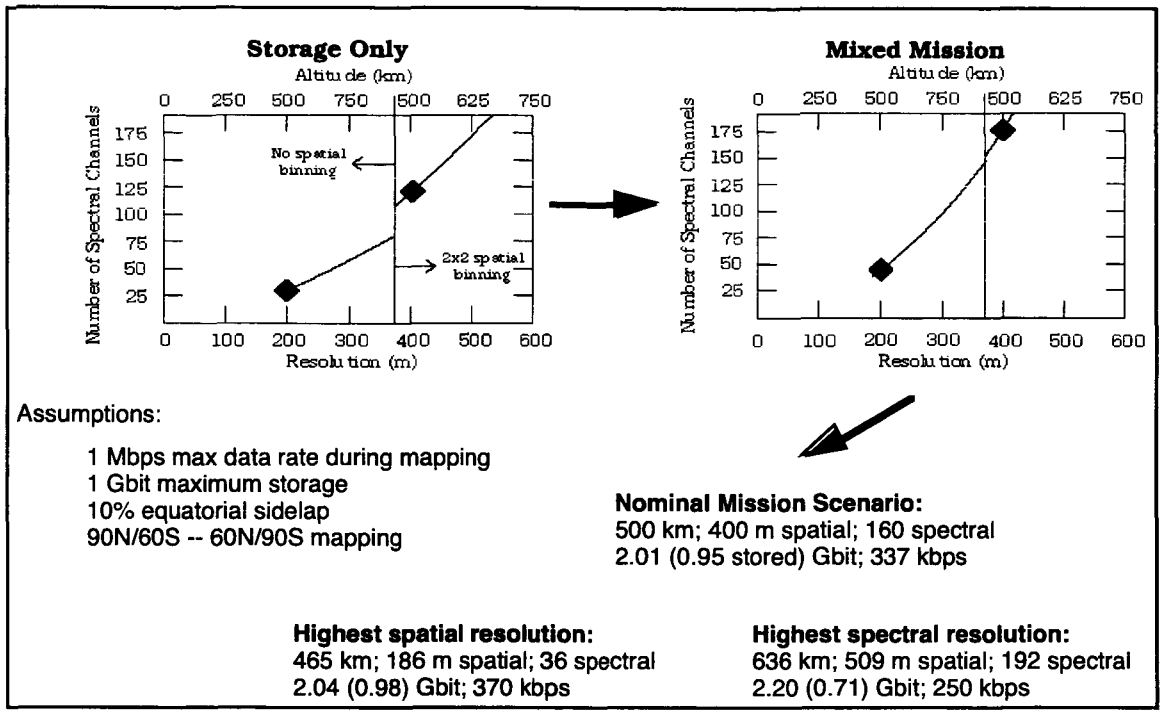

Figure 19. Strategies for far-side mapping. The mixed-mission scenario was selected for the nominal mission.

As shown in the figure, the nominal far-side scenario selected maximizes spectral resolution (160spectral channels) and reduces the spatial resolution to 400 m/p. Only 22% of the Moon is subject to the LOS scenario as is shown in table XVI. The storage-only scenario illustrated results in fewer spectral (or spatial) channels returned.

Differences in the two modes are shown specifically in table XVI.

TABLE XVI. COMPARISON OF RESULTS OF NEAR-SIDE AND FAR-SIDE MAPPING

AOS Mode		**LOS Mode**	
Spatial Resolution	200 m	Spatial Resolution	400 m
Spectral Channels	110	Spectral Channels	160
Telemetry Rate	926 kbps	Data Storage	0.91 Gbit
Total Data per Swath	3.67 Gbit	Percentage of Moon	22%
Percentage of Moon	78%		

The nominal global mapping strategy for MinMap is summarized in table XVII strategies.

TABLE XVII. MAPPING STRATEGY SUMMARY FOR GLOBAL MAPPING OF MINMAP. REGIONAL MAPPING DATA FROM AN ALTITUDE OF 100 KM ARE SHOWN BY THE NUMBERS AFTER THE BACKSLASH

Nominal orbital altitude	500 km
AOS/LOS resolution	200 m/400 m
% of Moon at lower resolution	22%
Number of spectral channels	110/160
Data per orbit	3.67 Gbit/2.01 (0.95) Gbit
Data rate	926 kbps/337 kbps
Swath length	4551 km (90N-60S/60N-90S)
Swath width	48.8 km (244 pixels)
Altitude tolerance	35 km
Pointing accuracy	±0.27°
Orbit plane accuracy	±0.73°

The global mission scenario derived from instrument capabilities and mission constraints has implications for absolute-pointing tolerances and for orbit-inclination tolerances that are necessary to ensure gore-free coverage. These tolerances are illustrated in figure 20.

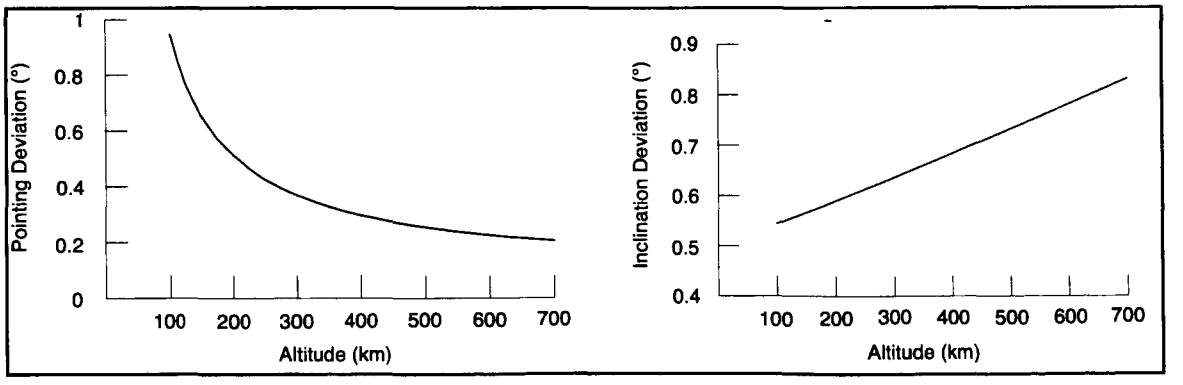

Figure 20. Derived tolerances for pointing deviation and orbit inclination. Pointing deviation is assumed worst case geometry with a 1% sidelap minimum tolerance. Orbit inclination (deviation from polar) is computed assuming a 1% polar overlap tolerance.

Regional High-Resolution Mapping Phase

Following the end of the global mapping phase, the Lunar Scout II spacecraft was to descend to an altitude of 100 km for the duration of the mission to acquire GRS data and high-resolution MinMap data. For the high-resolution phase, all spatial and spectral channels are used and data are collected and downlinked to the limit of the downlink capacity. For the far side, data are collected until the mass memory is full and the data are downlinked when the spacecraft is in the view of the DSN. The relevant parameters are shown in table XVIII. Note the 2 x 2 binning of the spatial pixels. This option allows more coverage, which was considered to be more important than higher spatial resolution. Ten percent of the lunar surface can be covered in the high-resolution mapping phase employing the options shown in the table. A greater percent could be covered by binning to a much greater degree in the spectral and/or spatial regimes.

TABLE XVIII. REGIONAL MAPPING PARAMETERS FOR THE IMAGING SPECTROMETER

Altitude	100 km
Spatial resolution	80 m (2 x 2 binning)
Spectral channels	192
Swath width	10.24 km
Swath length	250 km (162 s)
Compression	1:1
Data / swath	**0.92 Gbit**
Data rate	5695 kbps
Frame rate	19.3 fps
Number of swaths/orbit	2
Number of swaths/mission	1503
Lunar surface coverage	10%

Preliminary Mission Analysis

Overview

The Lunar Scout Program consists of two spacecraft launched approximately one year apart, each of which operate for one year. The two spacecraft work independently of each other except for a one-month period at the end of the first mission and at the start of the second mission when global gravity data is obtained. In order to evaluate the performance requirements for the Lunar Scout spacecraft and instruments, a "strawman" mission sequence was developed. Development of the proper mission requires iteration between the driving parameters of the integrated mission, some of which are shown in table XIX. The final mission will be developed to maximize the science return while at the same time minimizing the operational complexity and providing a cost-effective approach. In the following discussion, only a few of the driving parameters have been identified and studied to date; further detailed analyses are required.

TABLE XIX. MISSION DESIGN CONSIDERATIONS

Instruments/Operation	Spacecraft Design	Trajectory
Ground resolution	Data rate	Trajectory type
# of data channels	On-board data storage	Energy required (DV)
Swath length/width	Power profile	Launch window/opportunities
Swath overlap	Pointing accuracy	Transit time
Sun elevation angle	Pointing stability	Orbit altitude/orientation
% of surface coverage	Pointing knowledge	Orbit stability/maintenance
Instrument sequencing	Reliability	Lunar eclipse
Operational simplicity		

Instrument and Operational Considerations

Each of the instruments manifested on the two Lunar Scout spacecraft impose different operational constraints on the mission, spacecraft, and other instruments. Table XX provides an overview of the driving scientific measurement objectives and surface coverage requirements for both Lunar Scout spacecraft. The relative priorities shown were developed by LExSWG. These scientific measurement priorities were used extensively in the development of the preliminary mission profile and requirements development for the Scout spacecraft.

One of the major areas of concern of lunar orbital missions is the uncertainty of the lunar gravity field, including its magnitude and fluctuations. The lunar gravity field will have profound impacts on the spacecraft propellant loading and operations. Early refinement of the gravity field will greatly enhance the operations planning and spacecraft design. Developing a mission scenario, which refines the current gravity field knowledge early in the mission, is a primary goal for initial orbital operations. On the other hand, acquiring this data must be considered together with the other important science objectives. The mission development process must therefore balance scientific, spacecraft, operational, and risk considerations to develop the most cost-effective approach.

TABLE XX. MEASUREMENT OBJECTIVES FOR LUNAR SCOUTS I AND II

	Data returned	Coverage	LExSWG measurement priority
Lunar Scout I			
X-ray spectrometer	Major elements	Global	1
Neutron spectrometer	H, and other volatiles	Global	1
High resolution stereo camera	Imaging/topography	Global/regional	2, 4
Lunar Scout II			
Ge gamma-ray spectrometer	Major and minor elements	Global	1
Imaging spectrometer	Minerals at 0.35 - 2.4μ	Global/regional	3
Lunar Scout I and II			
Gravity	Global gravity	Global	2

The uncertainty of the lunar gravitational field establishes the priority of developing an operational gravitational model (produced from at least front-side gravity data if not global data) at the beginning of the lunar orbital operations. In order to obtain global gravity data, communications with the far side of the Moon is required. This can be achieved by carrying a subsatellite or by using both Scout spacecraft to provide the global coverage. The approach baselined for the Lunar Scout studies utilizes a two-spacecraft approach in which the spacecraft work together to develop the global gravity data. The decision for utilizing the two-spacecraft approach is not final, and further analysis is required to determine the best and most cost-effective approach. The two-spacecraft gravity data is obtained at the end of the Scout I mission and the beginning of Scout II. In order to enhance the gravity model at the beginning of the first mission, front-side data is obtained from Scout I alone.

Initiating the data-gathering sequences with the appropriate surface shadows is another important consideration of the initial operations. The arrival conditions must be chosen such that the initial spacecraft orbit at the Moon is in the proper orientation with respect to the Sun. The angle between the orbital angular momentum vector and the Sun (beta angle) is important in determining the periods of maximum Sun elevation angle. The Sun elevation angle (figure 21) is dependent on both the beta angle and the position of the spacecraft in orbit (latitude) relative to the Sun. As can be seen from table XXI, the HRSC requires low Sun elevation angles (~10° - 60°). MinMap and the XRS operate more optimally at high Sun elevation angles (~45° - 85° and ~30° - 90° respectively). The NS and GRS do not require proper Sun alignment because the excitation source is galactic cosmic radiation, not solar. Table XXI shows the required beta angle and the nominal operating altitude for the various instruments for both Lunar Scout spacecraft. The proper beta angle can be ensured by properly adjusting launch time and the time of flight to the Moon (table XXIV) (Ref.2).

TABLE XXI. INSTRUMENT OPERATIONAL CONSTRAINTS FOR LUNAR SCOUTS I AND II

	Optimum Sun Angle	Orbital Altitude
Lunar Scout I		
X-ray spectrometer	30° - 90°	100 km
Neutron spectrometer	n/a	100 km
Global imaging/topography	<15° - 60°	300 km
High resolution imaging	30°- 60°	100 km
Lunar Scout II		
Ge gamma ray spectrometer	n/a	100 km
Global imaging spectrometry	55° - 85°	500 km
High resolution spectrometry	45°- 85°	100 km
Lunar Scout I and II		
Gravity	n/a	100 - 300 km

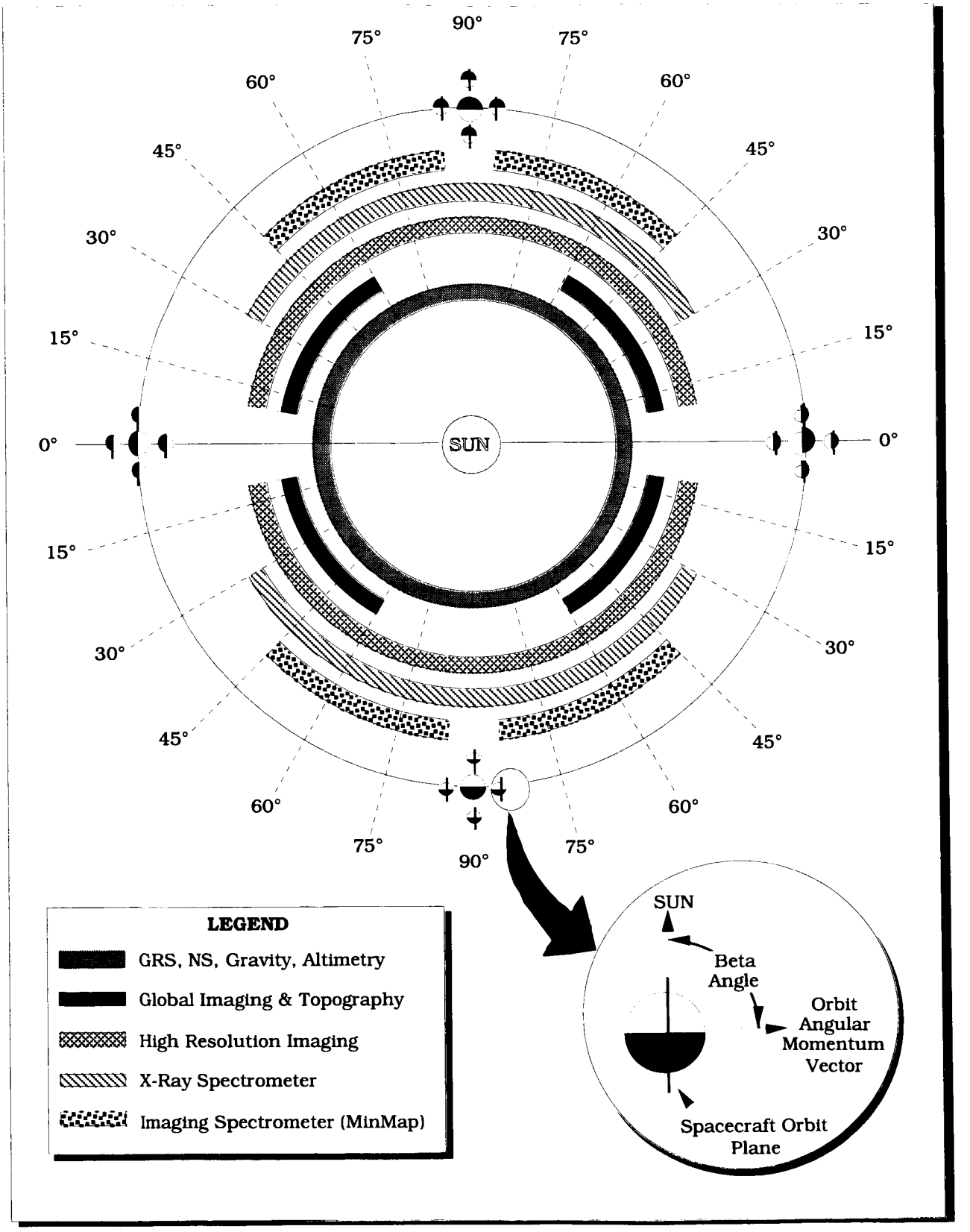

Figure 21. Instrument dependence on Sun (beta) angle.

The orbital operating environment of the instruments is divided into two distinct phases, representing the global and regional mapping, and is distinguished by the nominal operating altitude. The choice of the operating altitudes is driven by spacecraft, instrument, and operational constraints. Spacecraft and operational considerations include the energy management scheme, orbital maintenance, spacecraft subsystem capabilities (data to be stored, pointing stability, etc.), and communication links with Earth. Instrument considerations include the instruments' field of view, spatial resolution, ground coverage, and swath overlap. This interrelationship of some of these concerns is depicted in figure 22.

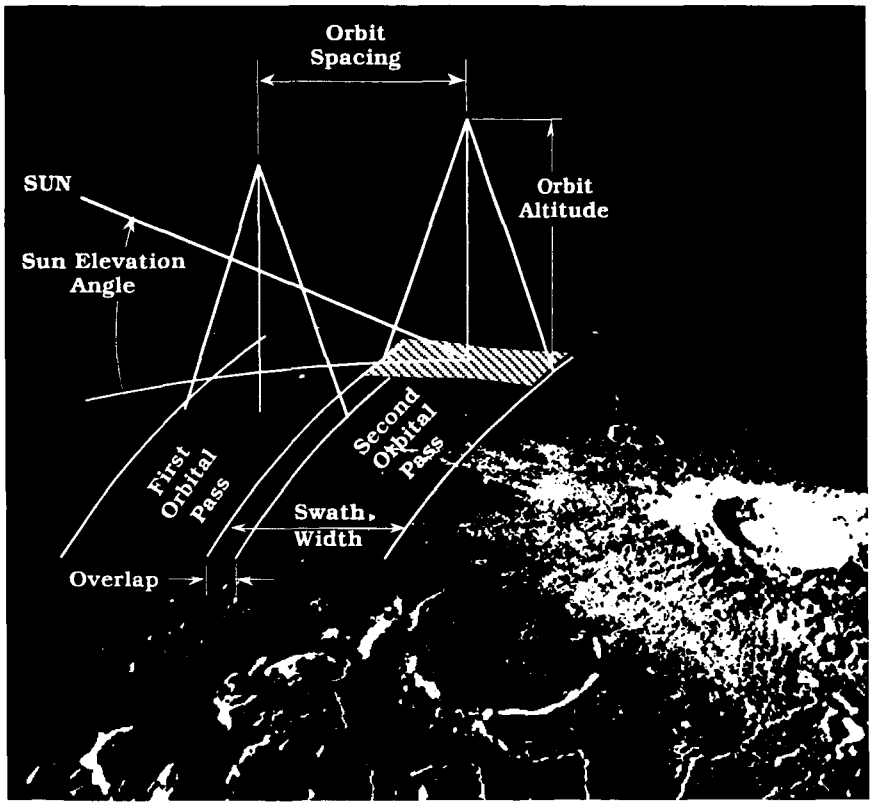

Figure 22. Lunar mapping considerations.

The final orbits for both Lunar Scout I and II were nominally chosen to be circular with an altitude of 100 km and a polar inclination. This selection was driven by the requirement to attain the highest resolution and signal-to-noise for all mapping instruments, and provide global access to any targeted region, yet maintain a low, gravitationally perturbed orbit.

The initial orbit of Lunar Scout II was chosen to be a highly elliptical orbit so that the spacecraft could serve as a relay between the Earth and Lunar Scout I during its LOS phase. This strategy allows the extension of gravity mapping to the far side of the Moon's sphere of influence, completing a global gravity map for the first time.

One of the objectives of Lunar Scout I is the acquisition of global imaging and topography data. This is achieved by using the three-axis stereo capability of the HRSC. The imagery is reconstructed from the nadir-looking line detector and the topography is computed by combining the information from the fore-, aft-, and nadir-looking detectors using the process of photogrammetry. The requirement for global coverage in a minimum amount of time early in the mission leads to the choice of a one-month global mapping phase. To ensure gore-free coverage, a nominal swath-to-swath sidelap of 10% is required, with a minimum tolerable of 1%. The Scout philosophy to minimize cost by imposing no (or only minimal) modifications to existing instruments leads to a mass memory storage constraint of 1 Gbit (10^9 bits) provided by the HRSC mass memory unit. In addition, all data taken by the HRSC must be stored and then downlinked at a later time. A maximum telemetry downlink rate of 1Mbps (10^6 bits per second) of science data is imposed by the capabilities of DSN (circa 1995). To compute maximum time available for downlink, a 60-second acquire and release time is built in. As shown in table XXII, a nominal global mapping altitude of 300 km satisfies all of these requirements and constraints as well as achieving both the highest nadir and the highest stereo resolution, minimizing the altitude-to-swath-width ratio (for photogrammetric stability), and allowing for a 10% tolerance in the orbital altitude. From this scenario, overall tolerances for both absolute pointing and orbital inclination are derived.

TABLE XXII. MISSION MAPPING PARAMETERS FOR LUNAR SCOUT I
(SEE ALSO MAPPING STRATEGIES)

Nominal orbital altitude	300 km
Altitude tolerance	30 km
Number of active line sensors	3
Nadir/stereo resolution	24 m/25.6 m
Data per orbit	0.74 Gbit
Downlink rate	558 kbps
Swath length	4551 km (90°N-60°S/60°N-90°S)
Swath width	42.4 km (3536 pixels binned by 2)
Stereo base length	103.8 km (18.9°)
Pointing accuracy	±0.37°
Orbit plane accuracy	=0.64°

One of the objectives of Lunar Scout II is the acquisition of global mineralogical composition data. This is achieved by maximizing the use of MinMap. Again, the requirement for global coverage in a minimum amount of time early in the mission leads to the choice of a one-month global mapping phase with a nominal 10% sidelap. The Scout philosophy to minimize cost through commonalty leads to the same mass memory storage constraint of 1 Gbit. However, this constraint only affects mapping on the far side during LOS since MinMap can, in principle, downlink data in real time (at the maximum DSN rate of 1Mbps). Consequently, a mixed-mission strategy is adopted for global mapping using MinMap that maximizes the spectral information at the highest spatial resolutions, with some loss in spatial resolution during far-side LOS mapping. As shown in table XXIII, a nominal global mapping altitude of 500 km satisfies all of these requirements and constraints and allows for a (less stringent) 7% tolerance in the orbital altitude (since the altitude is higher to begin with). Again, overall tolerances for both absolute pointing and orbital inclination are derived.

TABLE XXIII. MISSION MAPPING PARAMETERS FOR LUNAR SCOUT II
(SEE ALSO MAPPING STRATEGIES)

Nominal orbital altitude	500 km
Altitude tolerance	35 km
Resolution (AOS/LOS)	200 m/400 m
% of Moon at lower resolution	22%
# of spectral channels (AOS/LOS)	110/160
Data per orbit (AOS/LOS)	3.67 Gbit/2.01 (0.95) Gbit
Downlink rate (AOS/LOS)	926 kbps/337 kbps
Swath length	4551 km (90°N-60°S/60°N-90°S)
Swath width	48.8 km (244 pixels)
Pointing accuracy	±0.27°
Orbit plane accuracy	±0.73°

Trajectory Design Considerations

The design of the proper lunar trajectory is determined by several factors, including the required lighting conditions, the energy requirements, and operational requirements such as instrument sequencing and launch windows. Table XXIV provides a detailed explanation of the trajectory studies conducted for the Lunar Scout program (Ref. 2). The final energy budget is shown in tableXXIV.

TABLE XXIV. DELTA-V BUDGET FOR LUNAR SCOUTS I AND II

	Apoapsis (km)	Periapsis (km)	Minimum Delta-V (m/s) {a} Atlantic Pass	Minimum Delta-V (m/s) {a} Pacific Pass	Maximum Delta-V (m/s) {b}
Midcourse maneuvers {c}			50.0	50.0	50.0
Initial lunar orbit	300	300	816.9	773.8	1000.0
Orbital maintenance			0.0	0.0	0.0
Transfer orbit	300	300	40.3	40.3	40.3
Orbital maintenance			0.0	0.0	0.0
Final orbit	100	100	41.6	41.6	41.6
Orbital maintenance			100.0	100.0	200.0
Total			1048.8	1005.7	1331.8

Midcourse maneuvers {c}			50.0	50.0	50.0
Initial lunar orbit	7000	500	402.5	376.1	612.5
Orbital maintenance {d}			40.0	40.0	40.0
Intermediate orbit	500	500	387.5	387.5	387.5
Orbital maintenance			0.0	0.0	0.0
Transfer orbit	500	100	74.4	74.4	74.4
Orbital maintenance			0.0	0.0	0.0
Final orbit	100	100	78.2	78.2	78.2
Orbital maintenance			100.0	100.0	200.0
Total			1132.6	1106.2	1142.6

Delta-V's shown are for the 85° azimuth case. 95° result in similar Maximum Delta-V budgets.
{a} Orbital maintenance (circular orbits) for the "Minimum Delta-V" column is based on ±30 km deadband.
{b} Orbital maintenance (circular orbits) for the "Maximum Delta'V" column is based on ±15 km deadband.
{c} The TLI maneuver is done by the Delta II 7925. Midcourse maneuvers are done by the Lunar Scout vehicle.
{d} Orbital maintenance for 7000 x 500 km orbits based on ±10 km deadband for periapse with apoapse free.

Launch Window Design

A launch window strategy was developed for the Lunar Scout Program (Ref. 2). The mission requirements for Lunar Scout impose some restrictions on launch window because of lighting constraints and the need to map the gravity field for 30 days before starting other science measurements. The launch window strategy extended the launch window by using a technique that assumed a fixed launch azimuth and a variable launch time.

The Lunar Scout spacecraft were to be launched from Kennedy Space Center (KSC) on a Delta 7925. The Lunar Scout I spacecraft was to be placed into an inertially fixed parking orbit with a 300-km circular altitude, a 90° inclination, and a 90° longitude of the ascending node to meet a requirement for Sun angle to be 30° at 30 days after orbit insertion.

The Delta II can be launched from any azimuth, but the azimuth must be fixed during the launch window. A range safety issue restricts the allowable launch azimuths to lie outside the band of 85° to 95°. Because launch azimuth is fixed, it is necessary to vary trip time to increase the launch window. As trip time varies, the delta-V required for trans-lunar injection (TLI) and lunar orbit insertion (LOI) vary for each launch time. The primary determination for the launch window is the LOI delta-V. An LOI delta-V of 1000 m/s was assumed as the cutoff for the window. If no constraints were imposed on the inertial orientation of the orbiter, the launch window would be the same. The two constraints imposed on the inertial orientation of the Scout spacecraft shrink the launch window from the optimum launch day. Figures 23 and 24 depict the LOI and TLI launch windows, respectively. Delta-V requirements are shown in table XXIV.

Launch window considerations and calculations are described in detail in Ref. 2. It contains plots of launch window variations for both Scout I and Scout II and a summary of delta-V requirements.

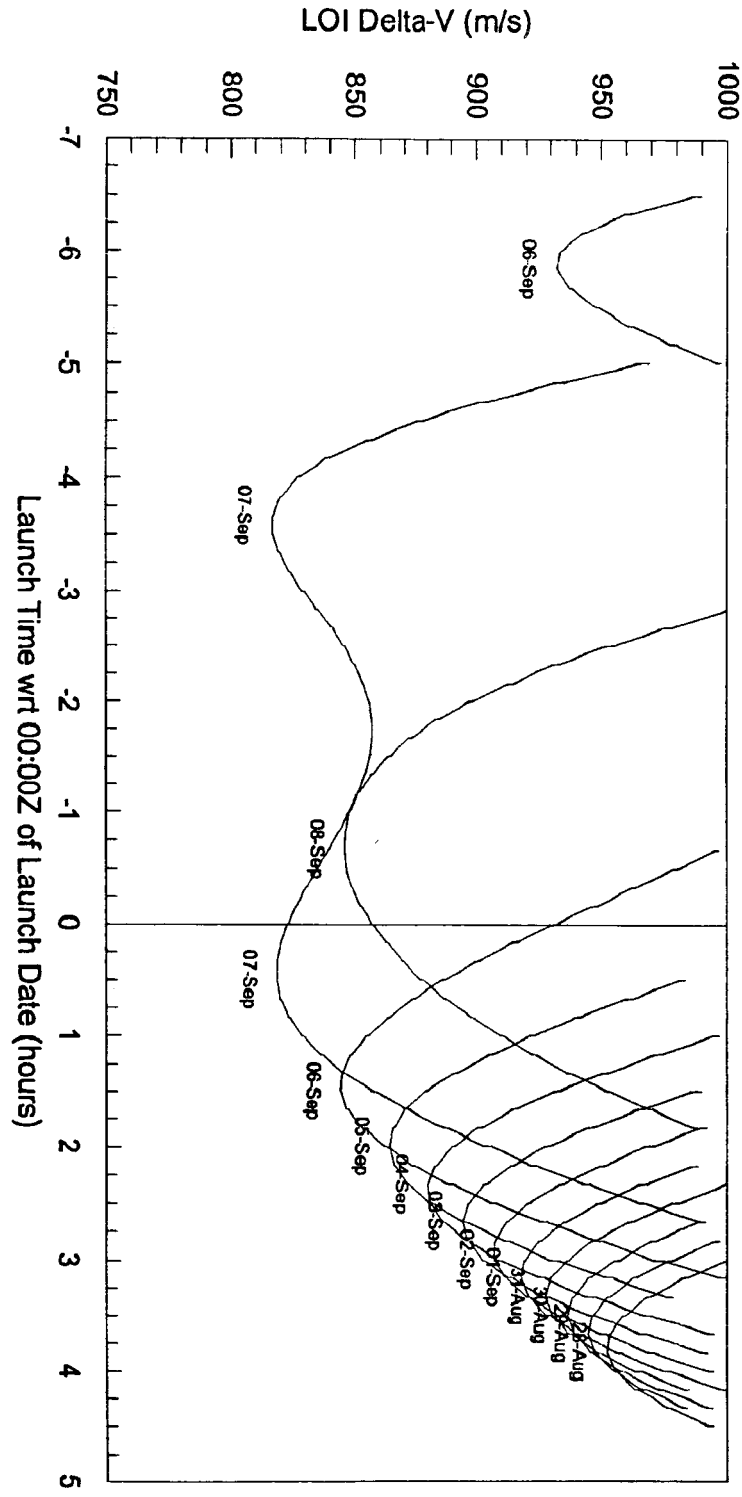

Figure 23. Scout launch window—LOI delta-V. Atlantic injection, 85° azimuth, single impulse LOI. Lunar data: LPO LAN=90.0 deg, LPO incl.=90.0 deg, lunar alt.=300 km at Epoch Sept. 12, 1996, 16:45Z. Earth data: EPO alt.=185 km, launch site lat. and long. 28.3°, -80.6°, Zero revs. before TLI. (See Ref. 2 for details.)

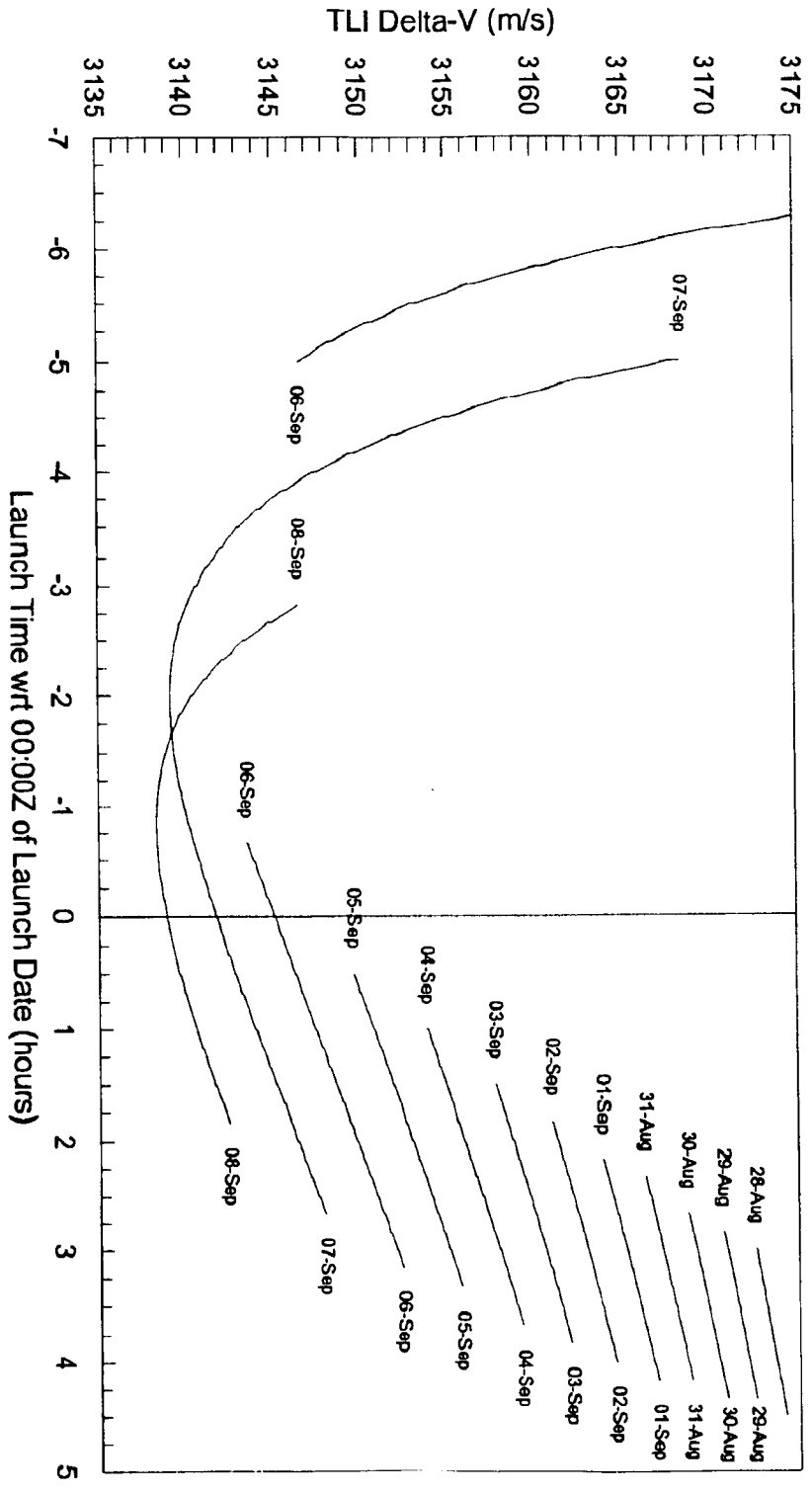

Figure 24. Scout I launch window—TLI delta-V. Parameters and factors as in figure 23. (See Ref.2 for details.)

Mission Summary

Figures 25 and 26 summarize the current mission plan for the Lunar Scout missions. The first Lunar Scout spacecraft will be launched from Cape Canaveral Air Force Station, Launch Complex 17, into a parking orbit of approximately 185 km altitude and 28.7° inclination. The Delta vehicle second and third stages can coast to any location around the parking orbit, up to one full revolution, before injecting the spacecraft into the lunar transfer trajectory. The length of coast does not affect the spacecraft mass capability. Injection is accomplished by re-ignition of the second stage, followed by spinup and firing of the third stage. The launch time and length of transit to the Moon are chosen to correspond to the appropriate lighting conditions at the Moon upon arrival. Figure25 shows a waning moon mission sequencing. This change was made after the initial mission studies were performed. The change from a waxing to waning Moon was made primarily to provide better backup mapping opportunities at the beginning of the global mapping phase. The change increases the number of high resolution mapping days by nearly 30%, while at the same time minimizing the "dead" periods at very low Sun angles when relatively little mapping occurs.

The lunar orbit insertion burn places the spacecraft into a 300-km circular polar orbit. Initial operations focus on vehicle testing and checkout along with conducting front-side gravity data collection. The data acquired will be used to develop an enhanced gravity model which is used for all future mission planning activities for both Scout spacecraft. During this initial 15-day period, the spacecraft is placed in a coarse-pointing mode in order to minimize the disturbances on the spacecraft, thereby enhancing the gravity data.

After the initial checkout and gravity mapping phase is completed, emphasis switches to obtaining the global data sets as produced from the HRSC and the XRS. This global mapping occurs for 50days when the Sun elevation angles vary from 60° to 10°.

After the global mapping has been completed, the spacecraft is lowered to its final 100-km circular orbit. During the remaining 320 days, high-resolution data collection occurs, including 30 days of global gravity mapping in conjunction with Lunar Scout II.

The launch of Lunar Scout II is timed such that the spacecraft arrives at the Moon during the last 30 days of the first Scout spacecraft mission. The timing of the second spacecraft is constrained to arrive at the Moon with local Sun angles of approximately 20°. In addition, the spacecraft is placed in a 7000-km x 500-km polar orbit in order to maximize the communication relay capabilities that the spacecraft will serve during the global gravity mapping phase. The choice of this arrival condition provides 30 days of vehicle checkout along with performing the two spacecraft global gravity mapping phase.

After the initial checkout and gravity mapping phase is completed, emphasis switches to obtaining the global data sets as produced from MinMap. This global mapping occurs for 30 days when the Sun elevation angles vary from 55° to 85°.

After the global mapping has been completed, the spacecraft is lowered to its final 100-km circular orbit. During the remaining 305 days, high resolution data collection occurs.

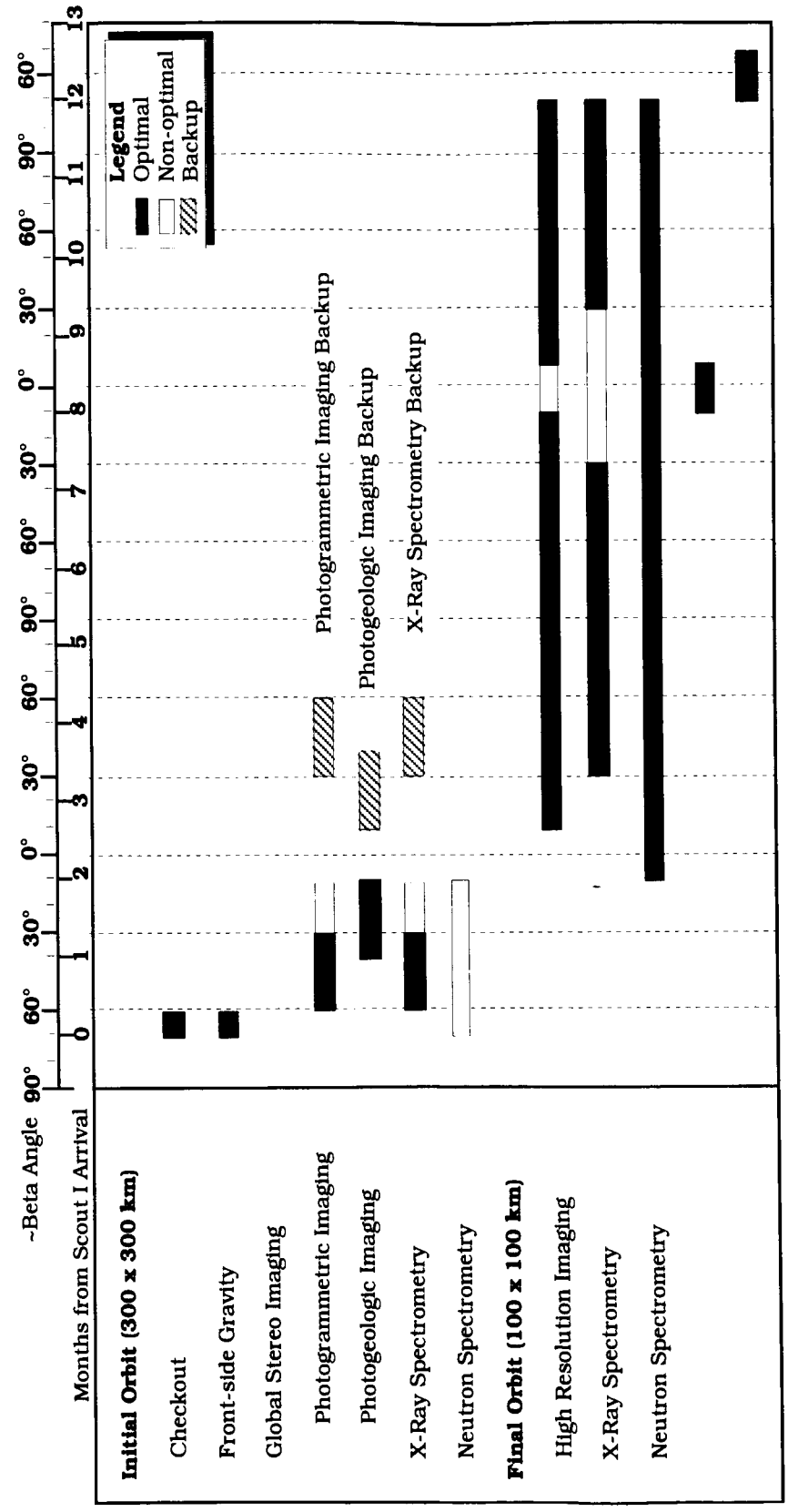

Figure 25. Lunar Scout I "strawman" mission profile.

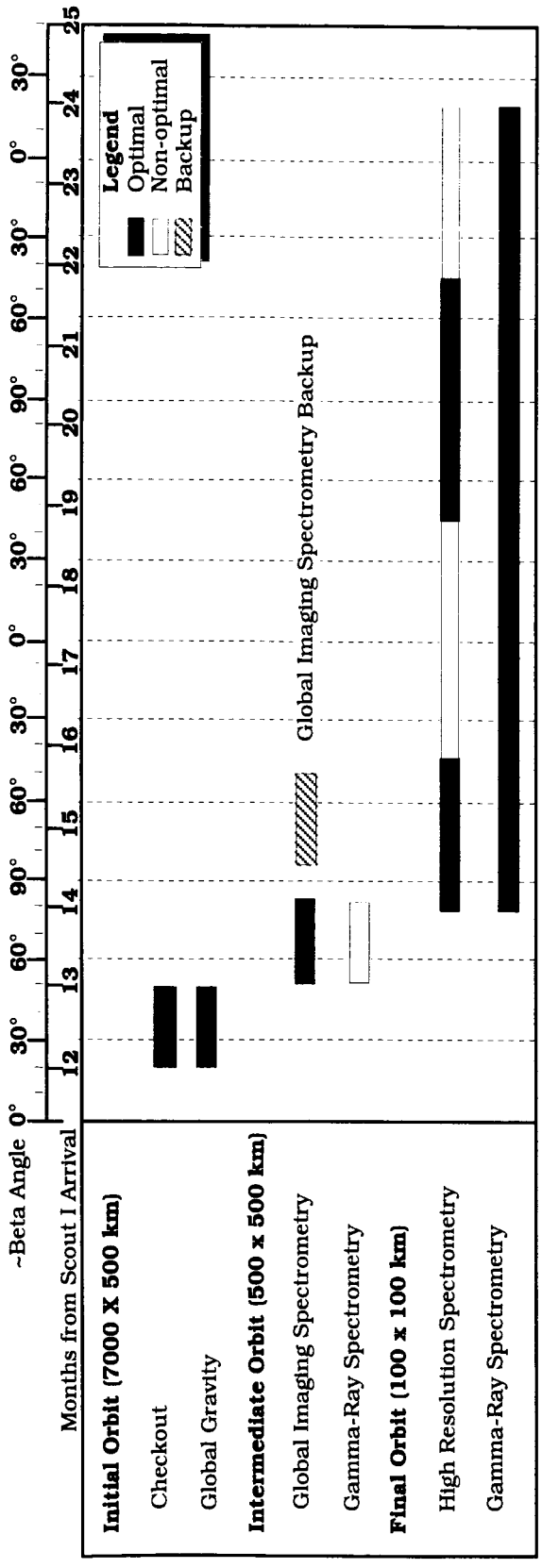

Figure 26. Lunar Scout II "strawman" mission profile.

Operations Concepts

Mission Operations Plan

The Mission Operations Plan governs the data acquisition, tracking, navigation, information management, spacecraft bus, and payload control functions. Final determination of the responsible organizations and facilities to perform mission operations will be made by no later than the Phase II start of the spacecraft bus award. A preliminary concept of the operations responsibilities is shown in figure 27.

Mission Operations are divided into several phases for each Scout mission:

Phase	0	-	Pre-launch support
Phase	I	-	Launch + one month (or until nominal mission status is achieved)
Phase	II	-	Through end of mission (11 month maximum)

In order to complete the global gravity mapping task, Phase II of the Scout I mission will overlap in time with both Phase 0 and Phase I of the Scout II mission.

The Lunar Scout Mission Operations Team (LSMOT), divided into the Mission Management Team (MMT) and the Mission Control Team (MCT), includes network, payload, spacecraft bus, integration and Scout Program Office personnel.

The MMT follows the mission from development through Phase I. At that time, the spacecraft has achieved lunar orbit and both spacecraft bus and payload are verified as operating nominally. The MMT will be located at the Lunar Scout Mission Control Center (LSMCC) for Phase I. They will participate in mission control after Phase I only if a contingency arises. The MMT includes the Scout Program Management and management representatives from the instrument module integrator, spacecraft bus provider, and instrument providers.

The MCT follows the mission from development through the end of the mission, conducting flight operations at the designated control facilities.

Designation of all team members and control facilities will be announced no later than Phase II start of the spacecraft bus procurement. A quarterly mission review will be held with all LSMOT members, either in person or by telecon.

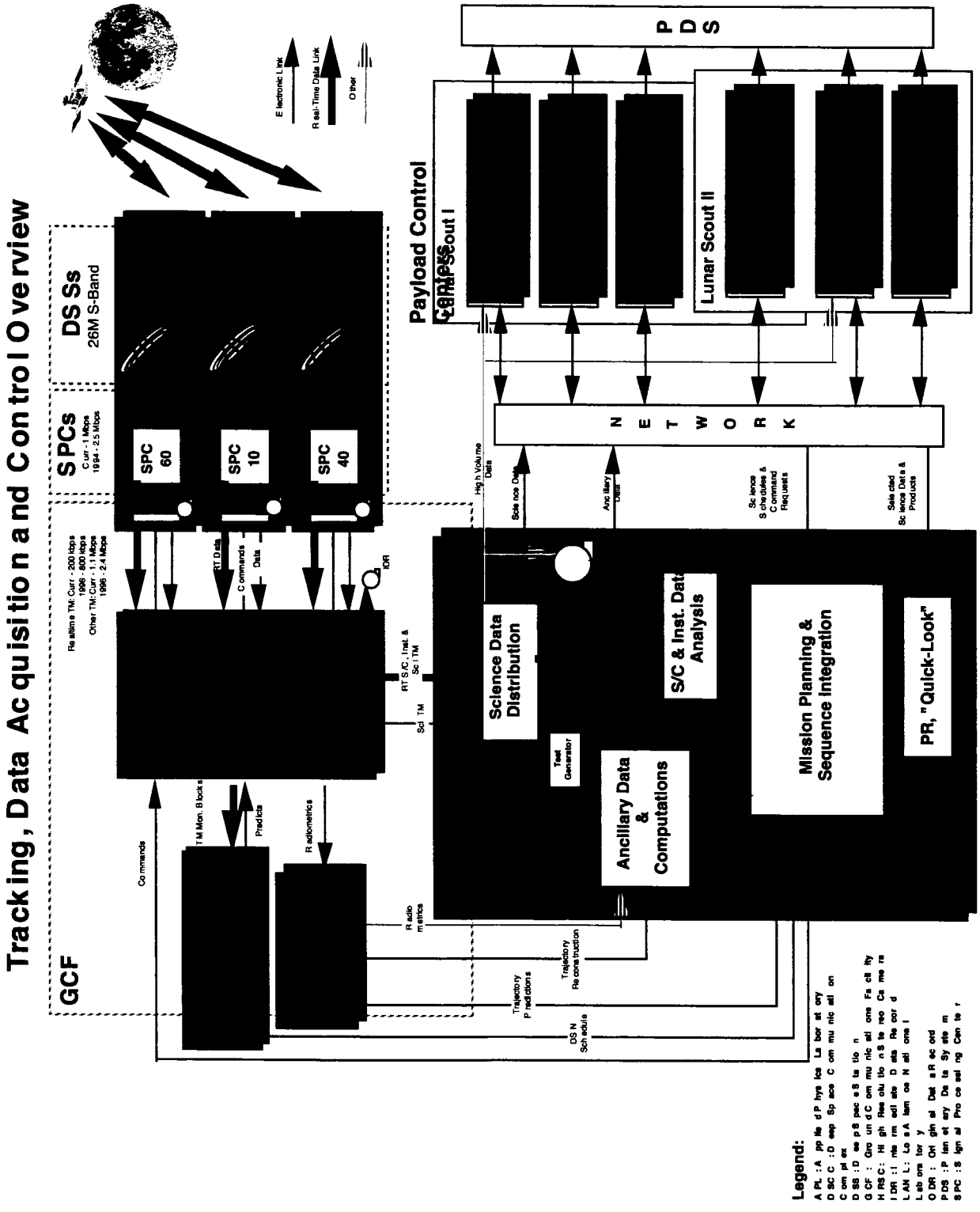

Figure 27. Tracking, data acquisition, and control overview.

Prelaunch Support

Preflight integrated simulations with all participating facilities are performed by the MCT with Scout Program oversight.

The following prelaunch activities at the launch site are supported by the MCT:

- Spacecraft and launch vehicle integration
- End-to-end testing
- Preflight integrated simulations
- Final payload acceptance test (may be at pad)
- Launchpad checkout
  - Final calibration of on-board instrumentation (engineering and scientific)
  - Detection and identification of faults since pad integration
  - Final verification of system operational readiness

Launch Operations

Launch operations control is at the Delta launch facility at Cape Canaveral, Florida. The spacecraft bus vendor will provide support to the McDonnell Douglas Commercial Delta Mission Director in the form of spacecraft status and launch readiness. The LSMCC will provide support to the Mission Director in the form of control center and network status. Mission operations control is passed to the LSMCC following completion of the TLI maneuver.

Telemetry, Tracking, and Navigation

The telemetry system receives, decodes, and transfers engineering and scientific data from the spacecraft to the LSMCC, located at Johns Hopkins University's APL, Laurel, Maryland. The tracking system generates radiometric data (i.e., antenna-pointing angles, spacecraft Doppler, and range data). The navigation system utilizes the radiometrics to reconstruct and predict the spacecraft's trajectory. The DSN has been baselined to perform these functions, utilizing these elements: (1) the Deep Space Communications Complexes (DSCCs) with locations at Goldstone, California; Canberra, Australia; and Madrid, Spain; (2) the Ground Communications Facility (GCF), operated by Jet Propulsion Laboratory (JPL), Pasadena, California; (3) the Network Operations Control Center (NOCC), located at JPL; and (4) the Multi-mission Navigation Team (MMNav), also located at JPL.

The DSCCs will be responsible for receiving and processing spacecraft telemetry once control has passed from the ground tracking network after launch. It is anticipated that the telemetry and tracking requirements of the Lunar Scout program can be accommodated by the DSN 26-m SBand subnet (DSN Stations DSS 16, DSS 46, and DSS 66). Telemetry are received, synchronized, demodulated, detected, decoded, encapsulated, and transmitted to JPL's Central Communications Terminal (CCT) via the GCF. All or a portion of the data stream is routed in real time to the LSMCC. This will consist of critical spacecraft and instrument telemetry and as much science data as is feasible. The remainder of the data stream will be transmitted to the LSMCC as time and bandwidth allow. The data are also recorded and stored at the CCT for possible recall by the mission control center.

All of the telemetry links must support data rates consistent with 1.0Mbps spacecraft downlink in accordance with the Lunar Scout Mission Plan, and must be operational no later than launch minus six months to support spacecraft testing and network and control center simulations. The DSN must be able to provide nearly continuous coverage over the mission lifetime (nominal two-year, one for each spacecraft, with an approximate one-month overlap), an "error free" link especially for highly compressed imaging data, and precision spacecraft tracking for both Scout missions.

The NOCC performs radiometric calibration, DSN sequence generation and scheduling, DSN monitor and control, DSN predicts generation, DSN telecon analysis, and DSN simulation. The DSN schedules will be coordinated with the LSMCC for mission planning purposes.

The MMNav receives the radiometric tracking data, processes it, and performs trajectory reconstruction and prediction. Its data products are routed to the LSMCC, for use by the mission planning team in actual maneuver analysis and design. The conditioned radiometrics will also be made available to the LSMCC for inclusion in the ancillary mission data.

Mission Control

The LSMCC is responsible for monitoring the status of all spacecraft bus and payload subsystems, commanding the spacecraft bus and payloads, coordinating mission planning during the mission, building mission data sets and routing them to the PIs, and maintaining the mission data archives.

Science Data Distribution

All science telemetry will be gathered, formatted, and distributed by the LSMCC. Electronic links will be established between the LSMCC and each Payload Control Center (PCC) for transferring instrument engineering, health and status data. Individual science data sets will be constructed for each PI and made available by electronic means, when practical. In the cases of very large science data quantities, distribution may be accomplished by physical transfer of high-density media (i.e., CD-ROM). Science data will be made available in a timely manner and consistent with agreements made between the Lunar Scout Program and the PIs.

Data Analysis

The spacecraft bus vendor is responsible for all spacecraft bus subsystem monitoring and any engineering data analysis necessary to ensure and maintain spacecraft bus subsystem health. This responsibility includes extracting spacecraft attitude information as part of the science support data. The instrument providers are responsible for instrument monitoring and any subsystem health data analysis. These functions will reside in the LSMCC. Both teams forward command requests to the Mission Planning and Sequence Integration team.

Ancillary Data

Additional information necessary for science data analysis by the PIs will be collected or computed by LSMCC. This includes the spacecraft attitude and instrument-pointing data, spacecraft and planetary ephemerides, spacecraft and instrument commands, and other pertinent data. These data sets will be made available to the PCCs by electronic means.

Project Data Archive

The LSMCC will construct and maintain an archive of all science and ancillary data from the Lunar Scout missions. This will be done in such a manner as to ensure safety and integrity of the data until transfer to the Planetary Data System has been completed.

Mission Planning and Sequence Integration

All spacecraft commands will be identified in the Lunar Scout Software, Command and Control Data Requirements Document. A premission command and control sequence plan for the spacecraft will be generated, including provisions for safing and reactivation, for all phases of the mission. This plan will be used during integrated simulations.

During actual mission operations, planning is performed at LSMCC by members of the MCT (except in contingency cases where the expertise and decision-making authority of other persons are deemed necessary). This includes integrating schedules and command requests from spacecraft, instrument and science teams into a sequence timeline, computing spacecraft maneuvers, coordinating DSN scheduling, and constructing uplink command loads.

Payload Control

The PCCs will transmit payload command requests and science schedules to LSMCC for command load integration and will support LSMCC with science products required for public relations or "quick-look" analyses. The PIs are responsible for the first level of science data reduction and processing. After initial processing and formatting is completed, the data is placed in the Planetary Data System for dissemination to the scientific community.

Mission Studies

Photogrammetry

Taylor Lawrence, Lawrence Livermore National Laboratory

The HRSC will produce data for compilation of a global geodetic net early in the Lunar Scout I mission. Parameters for both the global mapping phase and the lower altitude regional mapping phase are shown in table XXV. The selections for the global phase were based on the requirement to obtain global data as early as possible (in one month) while meeting data storage (1 Gbit) and downlink (1Mbps) constraints. For the regional mapping phase at an altitude of 100 km, 26% of the lunar surface can be covered at the 4 m/p resolution level over the course of the mission while again maintaining the same storage and downlink constraints.

TABLE XXV. HRSC AND MISSION PARAMETERS FOR BOTH THE GLOBAL AND REGIONAL MAPPING PHASES

HRSC Parameters:		
Entrance pupil	3.125 cm	
Focal length	175 mm (f/5.6)	
Stereo separation	18.9°	
Pixel size (IFOV)	7μm (40μrad)	
Mission Parameters:	**Global Mapping**	**Regional Mapping**
Orbital altitude	300 km	100 km
Nadir/stereo resolution	24 m/25.6 m	4 m/4.24 m
Swath length	4551 km	172 km
Swath width	42.4 km	20.7 km
Stereo base length	104 km	34 km
Data compression	10:1	6:1
Data per orbit	0.74 Gbit	0.82 Gbit
Data rate	558 kbps	7416 kbps
Months of mapping	1	8.3
Total compressed data	26 Gbytes	348 Gbytes
Surface coverage	100%	26%

The photogrammetric reconstitution of the images and generation of map products can be divided into three main tasks: (1) determination of conjugate points in the three image strips (nadir-, fore-, and aft-panchromatic channels); (2) local, regional, and global photogrammetric point determination; and (3) digital terrain model (DTM) generation and rectification (Ref. 3, 4).

The determination of conjugate points in the image strips is a necessary prerequisite for any further three-dimensional evaluation of the data (Ref. 5). In order to have sufficient information for DTM

generation, a large number of conjugate points must be identified in the stereo data sets. An added degree of complexity is introduced by having to identify the same object point in three image strips. The stability of three-axis photogrammetry justifies this addition. To determine the object points, a combination of matching techniques must be applied, including both automated and interactive approaches. This process can be very computational and manpower intensive, but advances in image processing software capabilities will shorten this process eventually.

The photogrammetric point determination (Ref. 6), which includes the reconstruction of the exterior orientation of the Scout spacecraft, represents the next step in processing the data once the conjugate points are identified. This process is based on the principle of bundle adjustment. The three-dimensional coordinates of object points and the parameters of the exterior orientation (spacecraft position and attitude) are simultaneously determined in a least squares adjustment from the following input data (the observables):

- Image coordinates of conjugate points
- Elements of the interior orientation (the geometry of the camera mount)
- Control information such as the location of ground control points or other lower resolution terrain information
- Information concerning the exterior orientation parameters (in order?)

A major problem associated with the photogrammetric point determination in the case of a planetary mission is the definition of an absolute coordinate system. This task has to be solved by using non-photogrammetric data such as the ground control information, existing DTMs, or highly accurate absolute information about the spacecraft position and attitude. Since high-fidelity control information is not known over a large portion of the lunar surface (especially the lunar far side), the *absolute* accuracy of the point determination depends highly on precise *absolute* measurements of the exterior orientation parameters. A study is currently underway to determine the anticipated accuracy of the point determination given nominal spacecraft observations and ways to increase the accuracy of these observations. Preliminary results using analytical tools developed for a terrestrial three-axis photogrammetry experiment to be flown on the Space Shuttle (STS-55) in April 1993 [the MOMS-02/D2 experiment (Ref. 7)] indicate that for the global mapping parameters listed in table XXV, and with spacecraft position measurement accuracy of 10 m and attitude measurement accuracy of 0.01° latitude and longitude, accuracy of 10 m can be achieved with an elevation accuracy of 23 m (Ref. 8).

From the image coordinates of the conjugate points and the orientation parameters, the three-dimensional coordinates of the matched points are calculated. A regular digital terrain model is derived using appropriate interpolation techniques. Photoclinometry (shape from shading) can also be incorporated into this process to further refine the DTM. Ultimate map products will then be produced which include orthoimages, contour maps, shaded relief maps, perspective views and profiles, and slope maps.

Cartographic data processing is closely connected and interrelated with parts of the photogrammetric processing. Individual scenes and data sets must be combined into a mosaic by converting to a particular map projection, radiometric normalization, and image enhancement to achieve best visual presentation in the final map products. Graphical processing such as the inclusion of color

information and the generation of contour lines must also be accomplished. The digital approach also offers new possibilities for the visualization of scientific findings in three dimensions.

With global resolution on the order of 20 m plus geodetic control approaching 100 m, and regional resolution of 4 m over one-quarter of the lunar surface, the maps that can be produced from these data will be the foundation for the development of future lunar exploration strategies.

Lunar Trajectory Interpolation for HRSC Stereo Mapping

Gregg Barton, The Charles Stark Draper Laboratory

Background

The HRSC is a "push broom" line-scanner stereo camera with three focal plate arrays. The photogrammetric reconstitution process discussed above is based on the principle of "bundle adjustment" where the determination of the surface object points and the reconstruction of the exterior orientation parameters from the three-line imagery are done simultaneously. The exterior orientation parameters are only calculated for the orientation points that are introduced at certain time intervals. In between, the parameters of every line are expressed as functions of the parameters of the neighboring orientation points. The HRSC team and the Technical University of Munich and Technical University of Berlin workers, based on Earth observations, have shown that a 3rd order polynomial function approximates the parameters (or the trajectory) between orientation points quite well for short arc lengths.

Objective

The goal of this study was to assess how far apart the orientation points can be placed in a lunar environment before the polynomial does not accurately predict the orbit trajectory. The farther the orientation points are placed apart, the greater will be the stability of the least squares solution due to fewer free parameters and the higher the elevation accuracy in the terrain maps.

Methodology

A prime consideration in this assessment was to accurately model the disturbing accelerations for a spacecraft in a low circular polar orbit. The truth model must represent a realistic trajectory in order to accurately assess the capability of an approximated function to interpolate the trajectory between known states. It was anticipated that the 3rd order Lagrange polynomial (equation 1) would have difficulty predicting the higher-order gravity-induced harmonics found at the Moon, especially for the long arc distances. Therefore, several gravity models were tested in order to provide a stressful environment and conservative estimate for the high frequency harmonics. The models included Konopliv's 75 x 75 spherical harmonic model (Ref. 9) and several variations of a 5 x 5 spherical harmonic model with point mascons on the lunar surface (Ref. 10). The maximum interpolation errors allowed between the truth model and the 3rd order polynomial were arbitrarily set to be 1/10 of a ground pixel, or approximately 2 m.

$$P_4(t) = \sum_{i=0}^{4} P(t_i) \prod_{\substack{j=0 \\ j \neq i}}^{4} \frac{t - t_j}{t_i - t_j} \quad \text{3rd Order Lagrange Polynomial} \quad (1)$$

It was anticipated that the interpolation performance could be improved when expressing the position coordinates in a non-inertial frame (proven in Ref. 11). Therefore, Sullivan (Ref. 11, 12) described the position of each orientation point in a local "local vertical local horizontal" (LVLH) frame relative to a reference circular orbit. This should not complicate the external parameters in the bundle equations since the vectors can be transformed from absolute inertial to relative LVLH quite easily. In Sullivan's analyses, the interpolation errors between the orientation points are relative errors expressed in a rotating frame—not absolute position differences.

The goal was to investigate the feasibility of increasing the arc length distances from 2 to 4 km used in Earth-based observations up to 20 to 40 km for lunar observations. The feasibility assessment initially evaluated arc distances of 2, 4, 10, 20, and 40 km between orientation points for a spacecraft in a 300-km circular polar orbit. Later, 100 and 400 km arcs were added due to the better than expected performance of the interpolation. The ascending node was initialized to 340° to place the trajectory over a large mascon to ensure large acceleration disturbances.

Results

The maximum interpolation errors for each arc length using the mascon gravity model are summarized in table XXVI (Ref. 12). In each case, the maximum error occurred over the large mascon. The 3rd order polynomial does quite well in interpolating the orbit between orientation points, assuming gravitational disturbances only. For arc lengths of 40 km or less, the maximum errors are below 1/4 mm. The arc lengths can be extended to 400 km and still meet the 2 m constraint.

TABLE XXVI. MAXIMUM INTERPOLATION ERRORS
FOR 3RD ORDER LAGRANGE POLYNOMIAL
(5 X 5 SPHERICAL HARMONIC GRAVITY MODEL WITH POINT MASCONS)

Arc length (km)	Maximum error (mm)
2	0.01
4	0.01
10	0.01
40	0.22
400	1407.

Table XXVII summarizes the sensitivity of the interpolation errors to the coordinate frames (rotating versus inertial) as a function of the arc lengths. In this sensitivity assessment, the mascon truth model was replaced with Konopliv's 75 x 75 spherical harmonic gravity model. This allowed comparison of the modeling of the gravity fields to the coordinate frames and a comparison with similar analyses performed by Condon (Ref. 13). The Lagrange polynomial provides approximately two orders of magnitude smaller interpolation errors for the rotating coordinate frame when compared to the inertial. This is not surprising since the rotating frame removes the circular arc freeing the interpolation to the perturbations.

TABLE XXVII. MAXIMUM INTERPOLATION ERRORS
FOR 3RD ORDER LAGRANGE POLYNOMIAL
(75 X 75 SPHERICAL HARMONIC GRAVITY MODEL)

Arc length (km)	Maximum Error (mm)	
	Inertial Frame	LVLH Frame
4	1.3×10^{-3}	3×10^{-5}
40	13.	0.18
100	500.	6.9
400	127,500	1147.

The high-frequency effect of the gravity model on the interpolation can be assessed when comparing tables XXVI and XXVII. For arc lengths of 40 and 400 km, the mascon model has peak errors approximately 22% higher than the pure spherical model. This has been attributed to the dynamics associated with the large mascon. Outside of the influence of this mascon, the 75 x 75 spherical model had larger interpolation errors due to the higher frequency content.

Conclusions

This analysis assessed the interpolation performance of a 3rd order Lagrange Polynomial in predicting the orbit trajectory between known state positions. In order to provide a stressful gravity environment to assess the interpolation capability, several lunar gravity models were tested for the high frequency content. The point mascon model proved to be approximately 22% more stressful for the interpolation when the spacecraft was over the mascon. Outside the influence, the higher order spherical model had larger interpolation errors. The 3rd order Lagrange Polynomial has shown to be quite effective for interpolating the orbit trajectory assuming only gravity-induced disturbances. The maximum interpolation errors were approximately two orders of magnitude smaller when expressing the position using relative LVLH coordinates instead of absolute inertial. The relative local-vertical coordinates improve the performance because the interpolation scheme can work on the perturbations rather than the nominal orbit itself. When using the LVLH frame, the maximum interpolation errors were sub-millimeter for orientation distances 40 km or less and below 2 m for 400-km arc lengths.

Lunar Scout Gravity Mapping

Gregg Barton, The Charles Stark Draper Laboratory

Introduction

A primary objective of the Lunar Scout Program was global gravity mapping for both scientific and improved navigation purposes. The Lunar Scout Program consisted of two spacecraft to satisfy programmatic (engineering and science) requirements (Ref. 14). The global gravity mapping objective can be accomplished quite easily using the two spacecraft when their missions overlap. At the end of the first Scout's primary mission, the second Scout would be inserted into a temporary 500 by 7000-km elliptic polar orbit to serve as a far-side tracking orbiter relay before completing its mission objectives at a lower orbit. During the overlap period, Scout I's perturbed velocity at a low 100-km polar orbit is measured by radiometric Doppler from both the Earth-based DSN and ScoutII, to extract a precise global gravity map. This is the two-spacecraft option, and it has some geometric implications.

Two-Spacecraft Geometry Options

Objective

The goal of this study was to provide a sensitivity assessment of (1) the global tracking coverage of the two-spacecraft geometry, and (2) the duration of the tracking. The purpose was not to recommend a particular geometric configuration but to show the sensitivity of the surface coverage relative to the parametric variations. The two-spacecraft geometry can only be optimized when it is known what measurement direction is most needed to improve the gravity coefficients with the highest uncertainty.

Methodology

The two-spacecraft tracking assessment is based on a comparison of the total availability and the direction of the observations for all the measurement opportunities from both the Earth-based DSN and the Scout II tracking relay. For each measurement observation, the downrange, vertical, and crosstrack components were accumulated into equi-area lunar surface bins and displayed in the form of mesh plots. This allowed a simple visual and statistical means to evaluate the sensitivity of the tracking coverage to the two-spacecraft geometry and the duration of tracking. The two-spacecraft geometry was defined in terms of (1) the wedge angle between the orbits, (2) the placement of Scout II's line of apsides, and (3) the period of Scout II's elliptic orbit. The variations in the tracking duration were limited to 14-, 28-, or 42-day opportunities.

Results

Several example mesh plots from the general trend analysis performed by Sauer (Ref. 15) are shown in figure 28. The plots in the figure document the availability of the vertical observations for Earth-only DSN tracking, Scout II relay, and the combination of the two using equal weighting. The frames of the equi-area mesh plots place the lunar limbs at 90° and 270° longitude and the equator at 0 on the Z-axis. North and South poles are +R and -R, respectively.

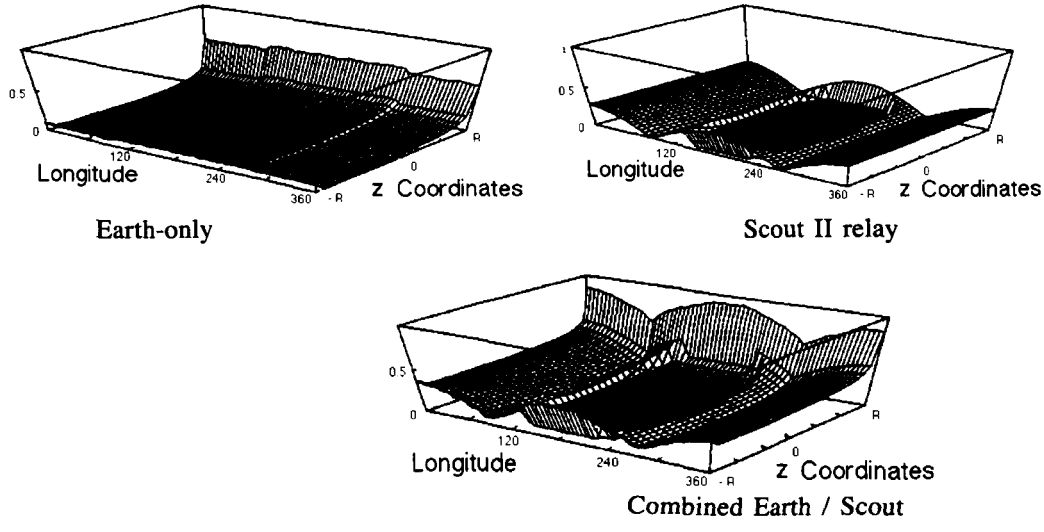

Figure 28. Vertical measurement opportunities. Wedge angle = 30°, Apsides angle = - 40°, 42-day tracking

The Earth-only plot shows the lack of coverage on the back side and the increased availability as the line-of-sight approaches nadir. As expected, using the DSN and a polar Scout I orbit generates no vertical measurements near the lunar limbs (±90° lunar longitude). The Scout II relay shows relatively even global coverage with a slight bias towards the northern hemisphere (to be addressed later). The superposition of the two forms the combined coverage. Because of the polar orbit, the poles show more measurement opportunities than the equator since the poles are traversed on every orbit. The bin widths were sized to contain five orbital passes each and averaged so that the resonances between Scout I and II were removed. Table XXVIII summarizes the parametric variations analyzed in the general trend analysis found in Reference 15. References 16-18 document the detailed analyses performed on each of the parametric variations. A summary of the sensitivity analyses follows.

TABLE XXVIII. PARAMETRIC VARIATIONS - GENERAL TREND ANALYSIS

Parameter	Variations
Wedge angle	0, 30, and 90°
Scout II apsides angle	0 and -40°*
Scout II orbit period	500 x 7000 km only
Tracking duration	14, 28, and 42 days

*Natural line of apsides = -40°

Wedge Angle—At a 0° wedge angle, all the measurement information is in the in-plane and no out-of-plane information is available. At the other end of the spectrum, a 90° wedge places most of the information in the out-of-plane. Sauer arbitrarily selected a 30° wedge angle as baseline to add some crosstrack information at very little expense to the in-plane information. Figure 29 shows the sensitivity of the downrange, vertical, and crosstrack measurements based on the percentage change to the 30° reference wedge (Ref 18). The Scout II natural line of apsides (-40°) was used in this case. The figure shows that the out-of-plane is more sensitive than the in-plane and that significant gain is made in the crosstrack at very little expense to the in-plane for small wedge angles. For the in-plane, the figure shows that the vertical is more sensitive to the wedge angle than the downrange component, and at about 60° wedge angle, significant degradation in the vertical channel is beginning to occur. Note, the non-zero line of apsides kept the in-plane components from being non-zero at the 90° wedge angle.

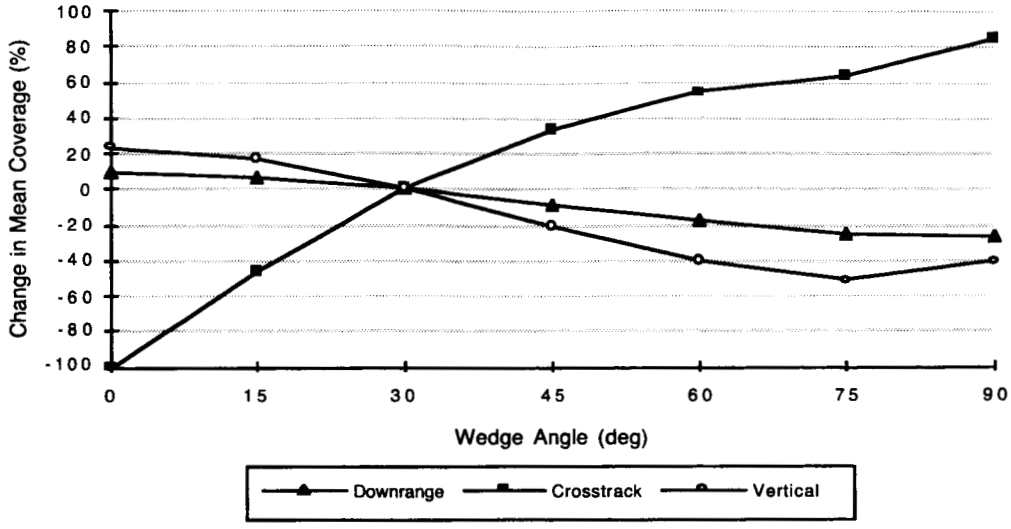

Figure 29. Surface coverage vs. wedge angle.

Scout II Apsides Angle—The rotation of the line of apsides only emphasizes one hemisphere over the other since shifting the line of apsides away from the equator biases the data to the hemisphere containing the Scout II apoapse. Obviously, a 0° apsides angle is desired for balanced North/South distributions (ignoring occultations), but fairly large apsides angles can be tolerated without significant reduction of measurement opportunities in the opposite hemisphere. Therefore, Reference 15 recommended using the natural line of apsides. The parametric sensitivity of the line of apsides placed 10° on either side of the natural line of apsides is shown in table XXIX (Ref. 17). A 10° shift away from the equator shows a degradation in the total performance in all three components. Conversely, a 10° shift toward the equator shows the opposite. Total variations in the coverage for 10° shifts are under 10%. However, there are no overriding reasons to add the additional delta-V budget to move the line of apsides away from the natural.

TABLE XXIX. CHANGE IN COVERAGE VS. LINE OF APSIDES ROTATION.

Line of Apsides	Change in Coverage (% of Nominal*)		
	Crosstrack	Vertical	Downrange
-30°	5.85	8.21	3.61
-50°	-6.27	-7.04	-3.84

*Natural line of apsides = -40°

Tracking Duration / Scout II Orbit Period—For the first 14 days of tracking, the analysis assumed that the Scout II apolune rotated across the far side, providing measurement opportunities not available from Earth-based stations. The second 14 days provided two-spacecraft tracking data on the near side, however, at a different perspective than the DSN. If another 14 days are added, then

additional data is accumulated over the far side to fill in any holes left from the first 14 days. The quantity and size of the holes is dependent on what level of resolution is needed in the tracking data. Table XXX summarizes the far-side coverage based on the bin widths, surface coverage, and the desired gravity model order. Reference 15 assumed that the equi-area bins were five orbits wide and, as a result, essentially no gaps in the coverage occurred. In Reference 16, the equi-area bins were varied between 1, 2, and 3 orbits in width. If the gravity modeler only needs 98-km resolution, then one far-side pass provides 100% theoretical coverage. (Of course, a second pass is still useful.) However, if a modeler prefers to have the tracking data at the highest possible resolution, then over 21% of the far side is not covered. When a second far-side pass (42-day coverage) is added, then theoretically 100% coverage occurs as long as Scout II's orbit period is not in resonance with the lunar rotation period. Otherwise, the coverage will be identical to the first and no new data will be added. The highest resolution tracking coverage will provide data at about 2.5x the resolution of the projected order of the required lunar gravity model.

TABLE XXX. FAR-SIDE COVERAGE VS. BIN WIDTH

Bin Width (deg)	Equator Surface Coverage (km)	Equivalent Model Order	Far-Side Gaps (%)
1.08*	32.7	167	21.5
2.16	65.4	83	3.0
3.24	98.1	56	0.06

*1 orbit

Conclusions

A sensitivity assessment on the global tracking coverage to the two-spacecraft geometry of the Lunar Scouts and the duration of the tracking was investigated. The purpose was not to recommend a particular geometric configuration but to show the sensitivity of the surface coverage to the parametric variations. The wedge angle shifts the coverage between the in-plane and out-of-plane measurements. In light of not knowing which measurement component to emphasize, it is recommended that a small wedge angle ($\approx 30°$) be used to add some crosstrack information at little expense to the in-plane information. The Scout II apsides angle does not appear to be an important parameter in terms of the surface coverage. Thus, the "natural" line of apsides angle should be used. Extending the tracking duration past 28 days doubles the amount of data collected on the far side. If the spacecraft orbit is not placed in resonance with the Moon's rotation rate, then the additional pass will fill in the remaining 21.5% of the far-side gaps. However, placing the spacecraft in resonance will increase the perturbation amplitude and increase the ability to extract the higher frequency coefficients.

Gravity Field Extraction

Objective

The goal of this study was to estimate the ability of the Lunar Scout mission to extract the lunar gravity spherical harmonic expansion coefficients from the global tracking data and to show the sensitivity of the harmonic coefficients to the radial, downrange, and crosstrack velocity

perturbations. The preceding discussion of the two-spacecraft option evaluated the sensitivity of the global tracking coverage to the geometry of the Scouts but did not recommend a specific geometry since it was not known what direction would provide the greatest amount of information to improve the gravity coefficients with the highest uncertainty. This study determined the general direction in which the induced gravity field harmonic motion maximizes the velocity perturbations. Thus, defining the mission to measure the velocity perturbations along the optimum direction will maximize the amount of information used to extract the gravity coefficients. However, this assumes equal weighting of information across the frequency spectrum and does not distinguish which harmonic terms in the best-to-date gravity model really need the most information.

Methodology

The downrange, crosstrack, and radial velocity perturbations can be expressed in the form of an approximate Fourier time series. This is extremely valuable in that it allows a harmonic spectral analysis of the velocity perturbations. The Fourier spectral analysis methodology is developed from Kaula's (Ref. 19) expression for transforming the gravity-induced Keplerian element perturbations into a harmonic series. Rosborough et al. (Ref. 20) enhanced the approach by transforming the position perturbations from Keplerian space into the downrange, crosstrack, and radial components of the spacecraft and simplified the expression for small eccentricity (order zero). Wagner (Ref. 21) expanded the methodology to include velocity perturbations. The methodology is limited to linear perturbations and cannot be used in cases where the spacecraft is in deep resonance or in a frozen orbit with the Moon's gravity.

The gravity field and an error assessment can be analyzed from the Fourier spectrum using tracking data from any of the three components. The approach requires long continuous tracking arcs to observe and extract all the resonant frequencies. Therefore, the sensitivity of the coefficients to the velocity perturbations in each axis can be assessed separately for all the harmonic frequencies and provide a simple methodology for selecting the optimum measurement direction.

Results

On the basis of the work performed by Rosborough and Wagner, Musoff (Ref. 22) derived a Fourier time series approximation for the downrange, crosstrack, and radial velocity perturbations for a lunar orbiter in a near-circular polar orbit. In this analytical analysis, the Fourier expressions for the velocity perturbations were compared to each other on a term-by-term basis. Equations 2 and 3 are the ratios of the terms of significant difference. Equation 2 forms the sensitivity of the radial to the downrange component and equation 3 is for the crosstrack to the radial.

$$V_{radial}/V_{downrange} = \frac{l(k^2+2)-1}{k(l+k^2)} \tag{2}$$

$$V_{crosstrack}/V_{radial} = \frac{m(k^2-1)(k-1)}{2(l(k^2+2)-1)} \tag{3}$$

where: V = Velocity perturbation
k = kth Fourier series harmonic
l = Gravity coefficient degree
m = Gravity coefficient order

The expressions derived for the radial and downrange velocity perturbations by Musoff show that the same frequency relationship occurs for the in-plane coefficients. However, the out-of-plane velocity perturbation proved to have an entirely different frequency content. Musoff deduced that the crosstrack perturbations have frequency pairs at $k = \pm 1$. Unless the data arc is sufficiently long to separate out the coefficients for the $k = \pm 1$ terms, a Fourier series expansion similar to the radial and downrange cannot be written. In his memo, Musoff assumed that the crosstrack frequency pair could be dissociated and wrote a separate expression for each. He then arbitrarily selected the k=-1 expression and formed the ratio shown in equation 3. Note, the order of the harmonic (m) is not explicitly shown in the in-plane ratio (radial-downrange), but is included in the out-of-plane component. The significance of this phenomenon is not understood at this time.

The sensitivities of the downrange to the radial velocity components and the inverse are shown in figures 30 and 31. The perturbation ratios are shown in the mesh plots for every combination of degree and harmonic from 2 up to 50. The figures have been set up so that the unity breakpoint is clearly visible. The white region represents the area where the perturbation sensitivity is below unity, or less sensitive. Figures 30 and 31 show that the perturbation sensitivity of the radial and downrange components are approximately split on the degree-harmonic diagonal. The radial component is more sensitive for high degrees at low harmonics while the downrange component shows the inverse. Therefore, for low harmonic frequencies, the radial component will be better at extracting the coefficient degrees when the degree is higher than the harmonic. In this region, on average, the radial is approximately 2x more sensitive than the downrange component as predicted by Wagner (Ref. 21). But, as the harmonic frequency is increased, the sensitivity of the radial begins to fall and the downrange velocity perturbation can become quite effective for extracting the degree of the coefficient, especially for low degrees.

Figures 32, 33, 34, and 35 summarize the sensitivity of the crosstrack to the radial velocity perturbation (and the inverse) as a function of the coefficient order, degree, and harmonic frequency. Since the crosstrack perturbation has added a third independent parameter, a single mesh plot cannot display the full spectrum. Figures 32 and 33 show the sensitivity of the perturbations to the coefficient order and harmonic frequency for a fixed coefficient degree of 30. Figures 34 and 35 reverse the degree and order. The figures show that the crosstrack component can be significantly more sensitive for extracting the gravity coefficients in all but the lowest harmonic and order. But, as discussed earlier, the crosstrack perturbations have a frequency pair that may not be separable unless long, continuous tracking arcs are available.

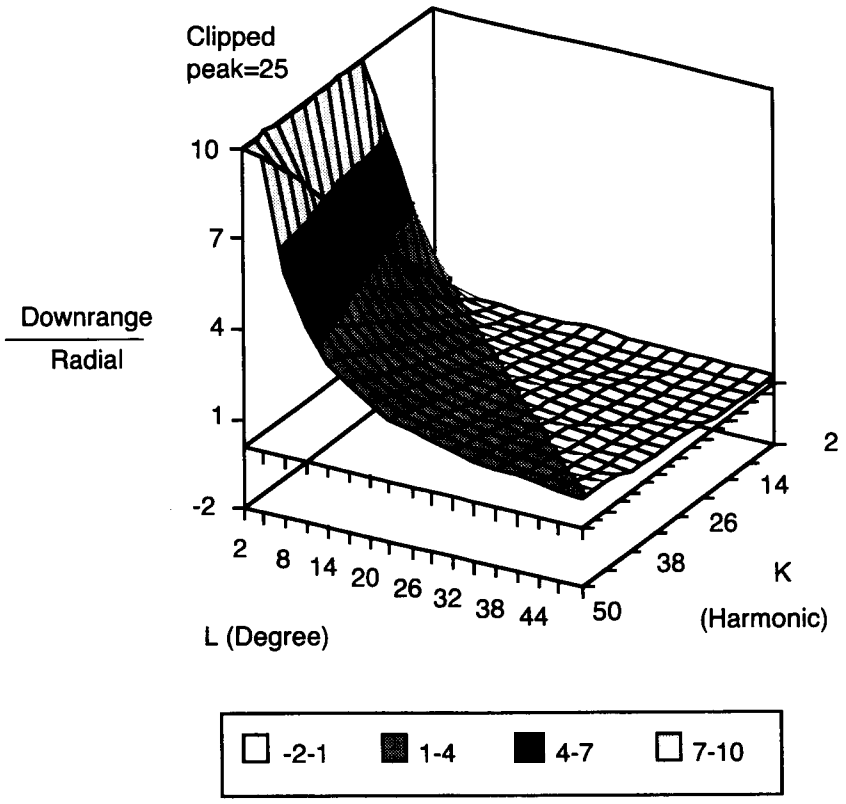

Figure 30. Downrange/radial velocity perturbation sensitivity.

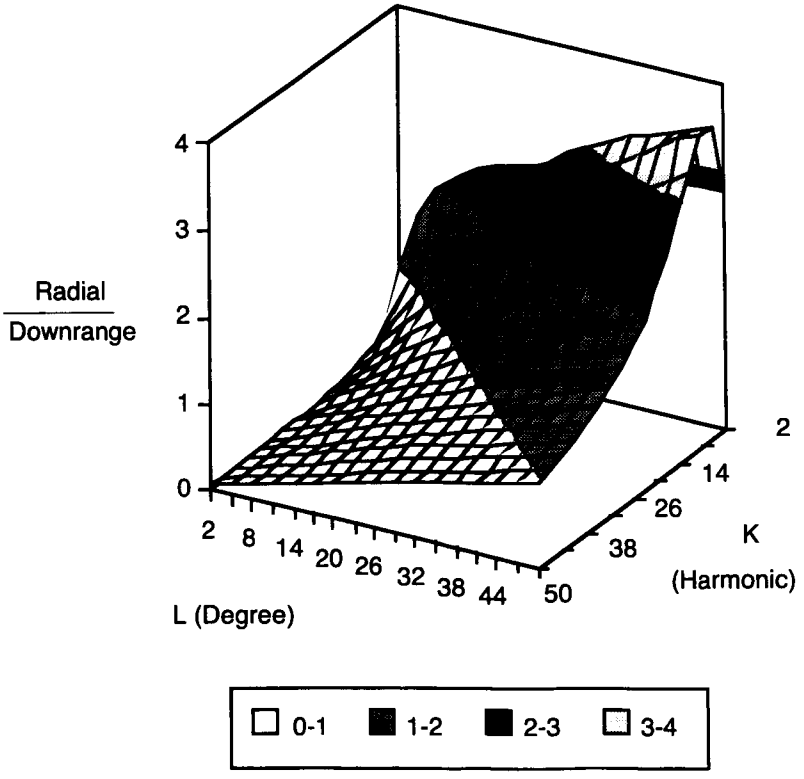

Figure 31. Radial/downrange velocity perturbation sensitivity.

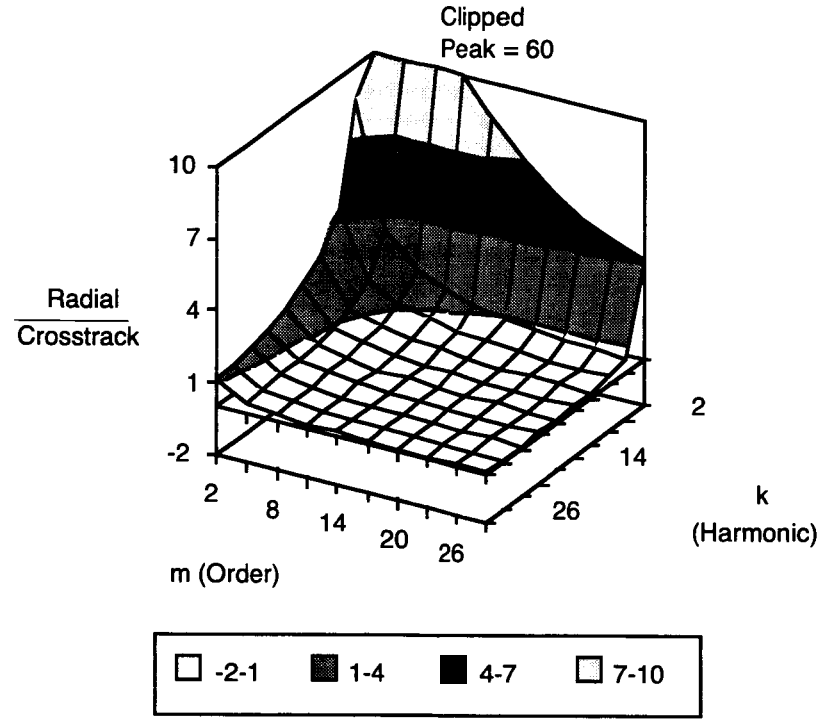

Figure 32. Radial/crosstrack perturbation sensitivity (degree 30).

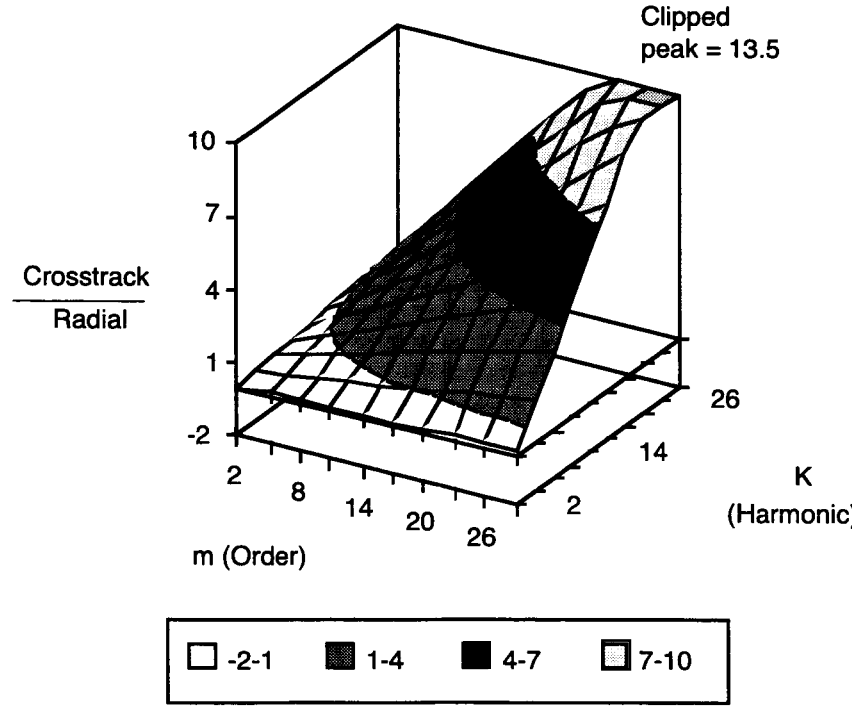

Figure 33. Crosstrack/radial velocity perturbation sensitivity (degree 30).

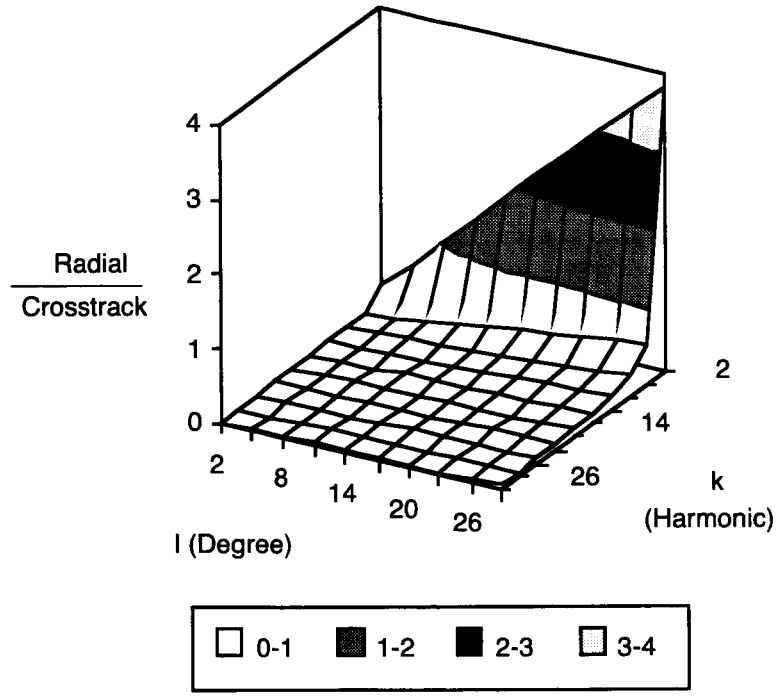

Figure 34. Radial/crosstrack perturbation sensitivity (order 30).

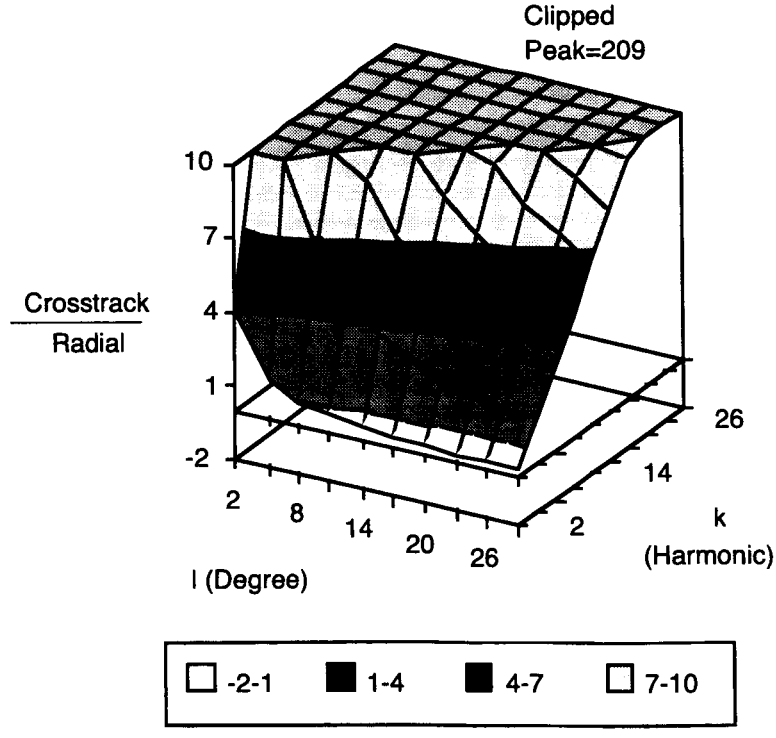

Figure 35. Crosstrack/radial perturbation sensitivity (order 30).

Musoff's general sensitivity trends emphasizing the crosstrack velocity perturbations agree with Wagner's results for Mars. In his analysis, Wagner computed the error spectra in the velocity perturbations assuming the a priori error knowledge follows the Balmino (Ref. 23) gravity model for coefficient terms up to 18 and the Balmino power law (k/l^2) for higher degrees. As a major point, Musoff did not include a priori knowledge in his analytical study. Wagner shows that the errors in the crosstrack velocity perturbations based on a harmonic analysis using the linear perturbation theory are significantly less than the other two components and will produce gravity field coefficients with the least errors. However, for the same Mars Observer polar circular orbit, Rosborough and Lemoine (Ref. 24) presented a gravity sensitivity study using direct orbit calculations rather than the linear perturbation theory. The velocity perturbations are computed as the difference in the mean orbit and the actual trajectory, so it is difficult to compare qualitatively the results from the Fourier time series with the direct orbit calculations. Rosborough et al. did show that the two methods generally have good comparisons except for orbits in deep resonance. As a minor point, the direct orbit calculations used the Balmino power law to estimate the coefficients for all degrees and orders. Rosborough et al. recorded that the radial velocity perturbations were the most sensitive to the gravity field. This appears to directly contradict Wagner's results. The graphs in the Rosborough et al. study (appear to) show that the in-plane and out-of-plane velocity perturbations are of the same character whereas the Fourier series developed in this and Wagner's analysis indicate a different qualitative appearance should exist between the two.

Davis (Ref. 10) discovered that several sets of coefficients pairs separated by a degree of 2 occurred when estimating the harmonic coefficients for a lunar orbiter in near-circular polar orbit. In his thesis, Davis evaluated the ability to extract harmonic coefficients up to a degree and order of 8 from a gravity truth model based on 5 x 5 spherical harmonic model in combination with surface mascons. The coefficient pairs had an extremely high correlation that inhibited the ability for the estimation routine to converge quickly. Davis assessed the ability to break the pairs by parametrically varying the observation geometry and measurement types. The assessment showed that the out-of-plane measurements provided the greatest sensitivity for breaking the coefficient pairs. However, there were multiple pairs of coefficients that could not be broken and appeared to be an artifact of the polar orbit. Davis suggested that the mapping mission consider including multiple inclinations to help break the pairs.

Conclusions

Using the results of Rosborough et al. and Wagner, a Fourier time series expression was derived for the circular orbit downrange, crosstrack, and radial velocity perturbations. For long, continuous tracking arcs, the approximate expressions indicate that, generally, the crosstrack perturbations are more sensitive to the lunar gravity field. However, the crosstrack velocity perturbations have frequency pairs that may not be separable unless very long arc lengths are available. Davis has confirmed that coefficient pairs with very high correlations do exist and inhibit the ability to extract the harmonic terms. For the in-plane components, the sensitivity appears to be split between the degree of the coefficient and the harmonic frequency. The radial component is more sensitive for high degrees at low harmonics while the downrange component shows the inverse. While the Fourier analysis has shown that the crosstrack perturbations generally provide the greatest amount of information for extracting the gravity coefficients as a whole, the analysis did not take into account the a priori knowledge available in the best-to-date lunar gravity field (Ref. 9, 25). A spectral analysis of this model should provide insight to the specific coefficients that need the most information.

The results of the general sensitivity analytic analysis were compared to similar analyses found in the literature. Two contradicting articles on the sensitivity of the out-of-plane velocity perturbations pertaining to the Mars gravity field were found. Until the out-of-plane issue is resolved, it seems prudent to include a small wedge angle between the two orbit planes to allow some out-of-plane information at very little cost to the in-plane information being gathered. If possible, multiple inclinations should also be used to break the harmonic pairs.

The goal of maximizing the gravity information extracted from the velocity perturbation can be accomplished by (1) measuring along the maximum perturbation, (2) increasing the measurement precision, or (3) increasing the perturbation amplitude by placing the orbiter in deep resonance. This report has addressed the first approach. Approach 2 is more of a hardware issue and will be dependent on items such as clock stability, carrier frequency, and signal-to-noise ratios. Approach 3 assumes some a priori knowledge is known to predict the deep resonant frequencies and the bandwidth. Of course, each approach can be used separately or in combination with the others. It is recommended that future mission planning investigate the feasibility of including Approach 3.

Co-Orbiting Satellite Options

Objective

The goal of this study was to assess the feasibility of using a co-orbiting subsatellite instead of the dual Scouts to perform global gravity mapping of the Moon. Due to budgetary constraints or unforeseen circumstances, a cancellation or delay of Scout II would jeopardize the successful completion of the global gravity mapping objectives. As an alternative, Scout I could transport and deploy a small subsatellite into either the elliptic orbit (500 x 7000 km) or a near-identical co-orbit with the Scout. This study will investigate the feasibility and address the problems associated with tracking a co-orbiting subsatellite (e.g., orbit and formation lifetimes).

Methodology

A co-orbiting subsatellite offers the advantages of long tracking arcs for extracting the gravity coefficients where the measurement observables are dependent on the co-orbit geometry. The subsatellite is assumed to be a freeflyer. Therefore, it is imperative that the subsatellite be placed in a mapping orbit that exceeds a 30-day tracking lifetime (no formation-keeping burns). The analysis considered two configurations of the Scout and its subsatellite—co-planar and offset. Traditionally, co-orbiting gravity mapping is performed with two satellites in co-planar orbits. In this arrangement, only the downrange measurements can be made. However, satellite placement is simple, and interpretation of the results may be easier because both satellites fly over the same gravity field. Also considered was an offset configuration that yields both crosstrack and downrange information. The wedge angle was arbitrarily set to 1.08° between the ascending nodes of the orbits and was equivalent to the Moon's rotation after one complete orbit of the Scout. If the subsatellite is nominally 60 km in front of the Scout, then the out-of-plane observability at the equator is 30°.

Orbit Lifetimes—A prediction of the orbit lifetime was assessed by simulating the subsatellite's motion using Konopliv's (Ref. 9) 75 x 75 gravity model and recording the instantaneous periapse for orbit decay. The orbiter was initialized with conic circular velocity in a 100-km polar orbit and evaluated for a one-month tracking period. A parametric analysis evaluated the sensitivity of the orbit lifetime to the initial ascending node in increments of 30°.

Formation Lifetimes—A theoretical prediction in the lifetime of the formation was assessed by comparing the separation distance between the Scout and the subsatellite, assuming both spacecraft were initialized with equal energy. In order for the satellites to not drift apart, the total energy (kinetic + potential) must be identical. If the energies are different, then there will be a secular change in the downrange separation over time. However, even with the same energy, the satellites are not necessarily in identical orbits and some separation will occur, mostly in the downrange direction. The equi-energy state is acquired by adjusting Scout's velocity to match the energy of the subsatellite's orbit. The analysis assumes perfect gravity knowledge and subsatellite placement to evaluate the theoretical capability. To assess the sensitivity of the performance of the equi-energy formation flying to the initial gravity conditions, both the offset and co-planar configurations parametrically varied the initial ascending node in 30° increments.

The ability to predict the equi-energy state is dependent on the following three parameters. Each was parametrically studied to assess the impact and sensitivity to maintain formation for 30 days (co-planar and offset) without station-keeping burns.

Gravity Modeling Errors - The potential energy calculated for each satellite is based on an imperfect knowledge of the Lunar gravity field and therefore will only be an approximation. The effects of the gravity modeling uncertainties were assessed by computing the equi-energy velocity using an imperfect gravity model (16 x 16 truncated Konopliv gravity model) and comparing the resulting motion to the actual orbit after one month. The truth model is based on the full (75 x 75) gravity model (Ref. 9). The parametric study assessed the sensitivity of the gravity modeling errors to the initial ascending node in 30° increments as before.

Velocity Insertion Errors - Precise energy control requires precise velocity delivery or burn execution capability. To determine the sensitivity of the formation to the velocity errors for a 30-day mission, a small delta-velocity error was inserted into the Scout's equi-energy velocity. The parametric study assessed the sensitivity of the velocity insertion errors for varying initial ascending nodes as before. The gravitational potential and orbiter states were assumed to be known exactly.

Navigation or State Uncertainty Errors - The lack of knowledge of the states of the two orbiters will make the desired equi-energy condition difficult to achieve. This assessment will evaluate the sensitivity of the equi-energy to the navigation uncertainties. Typically, the DSN can only determine position within ±100m and velocity to within ±0.1 m/second after a front-side tracking pass. With state uncertainties of this magnitude, it would seem impossible to achieve equi-energy. However, these state uncertainties do not necessarily mean that energy is not known. In most navigation problems, total energy is actually known quite accurately. The difficulty arises when the separate kinetic and potential energy components are sought. In other words, the orbiter state error will be correlated (high and slow, or low and fast) such that the total energy is the same. Since only energy is of concern, the actual position and velocity errors are not critical. After separation, the DSN can determine the total energy of each active orbiter quite accurately. With same beam tracking, the DSN can determine the relative energy between the two orbiters directly. Thus, it is not unreasonable to assume that relative energy can be measured precisely. The issue becomes: When matching equi-energy states, how much burn error is introduced due to errors in the navigation states?

The equation, $\Delta V \approx \Delta E/v$, relates the velocity change to the relative energy difference and the orbiter velocity. Sullivan (Ref. 26) assumed that the energy difference is known but the orbiter velocity is approximate, and derived equation 4 that relates the delta-V (burn) error to the velocity change as a function of the state velocity uncertainty. The magnitude of delta-velocity (ΔV) is dependent on

the required change in energy, velocity (v) is based on orbital mechanics, and delta-V is dependent on the measurement capability. Therefore, equation 4 can assess the equi-energy sensitivity to the navigation uncertainties.

$$\delta\Delta V = \left(-\frac{\delta V}{v}\right)\Delta V \tag{4}$$

Results

Orbit Lifetimes—The "quick-look" investigation concluded that the maximum orbit decay expected over one month is approximately 28 km. Sullivan's periapse altitude graph records a minimum of 72 km which is more than sufficient to ensure that impact will not occur with the lunar surface.

Formation Lifetimes—The formation assessment predicted that the equi-energy theoretical performance can be quite good. In the worst case scenario, Sullivan predicted that the subsatellite would not drift by more than ±1 km and ±18 km for the co-planar and offset geometries, respectively. As expected, the offset case is higher due to not flying the same orbit.

Gravity Modeling Errors—Sullivan reported that the downrange separation did not change more than 3 km from the equi-energy case, suggesting that gravity modeling is not a limiting factor. This assumes that lunar gravity knowledge is known to a spherical harmonic order/degree of 16, and the higher frequencies represent lack of knowledge.

Velocity Insertion Errors—Sullivan concluded that the additional separation error in the formation after one month was roughly proportional to the velocity error and independent of initial ascending node. Table XXXI lists the maximum formation errors (differences in the separation of the spacecrafts compared to the equi-energy performance) to two different velocity errors. The table concludes that at least one formation-keeping burn would be necessary when velocity is controlled to only ±0.01 m/sec. But, if the velocity is controlled an order of magnitude better, the spacecrafts could free-fly in formation. This latter figure is a very tight requirement on burn accuracy, possibly requiring a low thrust capability.

TABLE XXXI. MAXIMUM FORMATION ERRORS AFTER 1 MONTH

Velocity Error (m/s)	Co-Planar (± km)	Offset (± km)
0.01	72	87
0.001	8	25

Navigation Errors—Sullivan reports that for a 100-km orbit and typical S-band velocity measurement precision (0.1 m/sec), velocity changes on the order of 10 m/sec will have burn errors less than 0.001 m/sec. Velocity errors of this magnitude are not a problem to formation lifetimes as was demonstrated in table XXXI.

Conclusions

Using a subsatellite for the observer in the gravity mapping phase of the Lunar Scout mission is both possible and practical. Achieving the desired insertion velocity appears to be the most difficult problem. Assuming that small burns can be used to control velocity to within ±0.001 m/sec, it appears quite possible to place Scout I and its subsatellite in equal energy orbits which would require no formation-keeping burns during the course of the month long mission.

The only way to get crosstrack data is to use an offset formation. The maintenance of this formation is slightly more difficult, but even doing one burn would not prevent gathering the long data arcs necessary to make use of the crosstrack data. The offset is more difficult to attain and maintain, but does provide valuable crosstrack information.

Radiometric Tracking Power Requirements

Objective

The goal of this study was to provide a first-cut feasibility assessment on the RF transmission power requirements for the two-spacecraft and co-orbiting gravity mapping geometries. The purpose of this study was not to perform a system trade study to determine the most cost-effective gravity mapping approach. The study also did not consider the option of using a laser ranging system as proposed by GSFC (Ref. 27) for co-orbiting satellites. The intent was to compare the power transmission requirements as a function of the RF methodologies for the different gravity mapping geometries under consideration by the Lunar Scout Program Office.

Methodology

The best method for extracting a global gravity map would be to directly measure the spacecraft accelerations due to the gravity wave perturbations. However, a spacecraft in free-fall cannot measure gravity induced accelerations with any on-board instrumentation. Therefore, the next best approach is to measure the gravity-induced velocity perturbations over a finite time span to infer the local accelerations. The spacecraft's velocity perturbations are easily measured both on the near and far side of the Moon by Doppler radiometrics from a second orbiting spacecraft either in co-orbit or in a high elliptic relay orbit (Ref. 28). Lunar Scout baselined the latter using the overlapping Scout missions. However, the former was not considered as an option because of the budget constraints of launching more than one Scout mission. In either case, the subsatellite or the second Scout can act either as an active or passive target in either a co-orbit or an elliptical tracking orbit, depending on the most cost-effective design.

A passive target reflects the radar signal back to the sender. This method is the simpler and potentially cheaper of the two in that it does not require communication hardware on the target spacecraft. However, the technique can require massive amounts of power on the sender spacecraft for nominal transmission distances. Sauer (Ref. 29) proposed using equation 5 to compute an estimate of the transmission power for passive range measurements assuming a tracking threshold less than 1/3. The range measurements are used since Doppler is a free measurement with range and both are needed for global navigation.

$$P_T = \frac{9}{2}\frac{N_o B_n}{G^2}\left(\frac{4\pi R}{\lambda}\right)^4\left(\frac{\lambda^2}{4\pi\sigma}\right) \tag{5}$$

where: N_O ≡ Receiver noise power density (w/Hz)
R ≡ Range between spacecraft (m)
B_n ≡ Bandwidth of the tracking loop (Hz)
λ ≡ Wavelength of carrier signal (m)
G ≡ Antenna Gain (nd)
σ ≡ Effective radar cross-section of target (m^2)

For an active system, both spacecraft require power generation, signal transmission, and an antenna system. However, this may not add additional cost to the dual Scout mission since both Scouts will carry the standard communication system. For RF tracking purposes, the signal can be either one-way or two-way between the sender and target. For a one-way system, the sender spacecraft continuously broadcasts a time-tagged signal on a known carrier frequency and requires an ultrastable oscillator and an accurate clock for precise navigation. For two-way systems, the target spacecraft receives the RF signal from the sender on one frequency and re-transmits it on another, thus requiring the target to have both a transmitter and receiver. There are many RF strategies for initiating and relaying the signals so it is not a given which is the sender and target spacecraft. To simplify the feasibility study, Sauer proposed using equation 6 as an estimate of the transmission power requirement for active measurements assuming a 13 dB tracking threshold. The equation is based on a one-way range measurement to be consistent with the passive system, and it also approximates the power needed on both ends of a two-way system.

$$P_T = 8.91 \frac{N_o B_n}{G_T G_R} \left[\frac{2K\tau R}{\lambda \sigma_\tau} \right]^2 \qquad (6)$$

where: G_T ≡ Transmission antenna gain (nd)
$1/\tau$ ≡ Chipping rate (1/s)
G_R ≡ Receiver antenna gain (nd)
K ≡ Empirical constant (m/s)
σ_τ ≡ Standard deviation of the tracking loop error (m)

Results

The results of the active RF transmission power feasibility assessment are summarized in figures 36 and 37 with the power requirements graphed as a function of the range to the target. Figure 36 shows the estimates for the co-orbiting satellites and figure 37 shows the estimates for an elliptic relay orbit. Both cases assume L-band global positioning system (GPS) frequency with omni-antennas. The co-orbit and elliptic orbit relays require less than 0.1 mW and 200 mW, respectively. These estimates should not be a problem for the power generation system design assuming a 2.5x factor between power transmission to power generation.

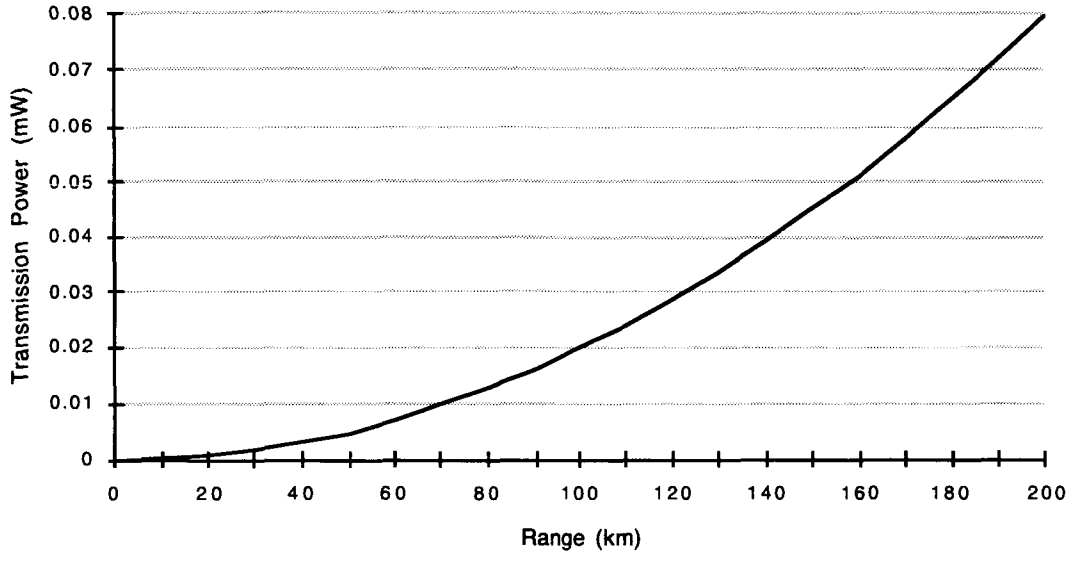

Figure 36. Active target transmission power estimates: co-orbiting satellites.

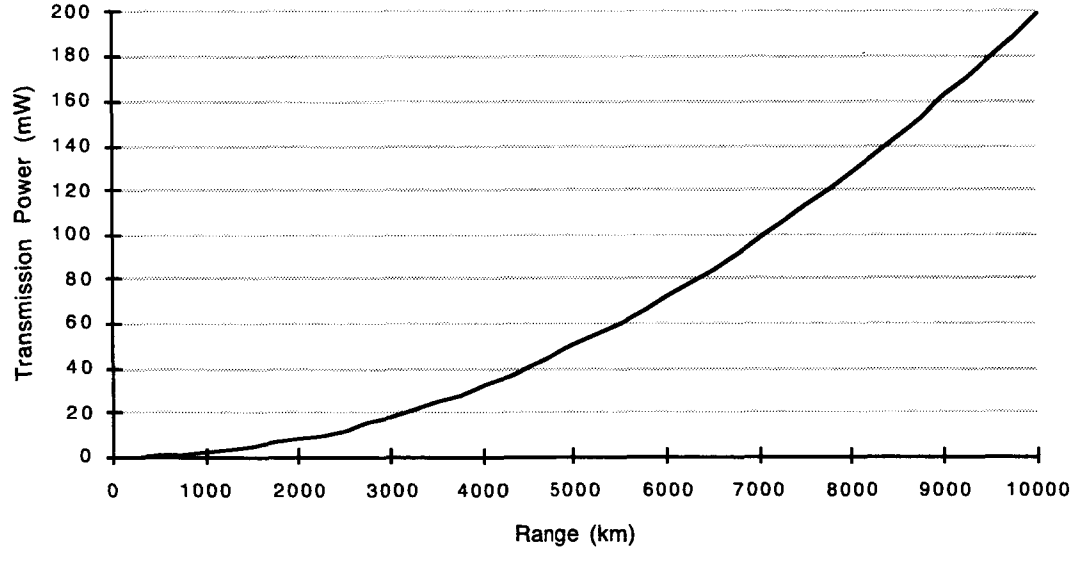

Figure 37. Active target transmission power estimates: 500 x 7000 km elliptical relay orbit.

Figure 38 summarizes the results for a passive target which is assumed to have a side reflectance length equivalent to a one-meter corner cube. The figure shows that the power requirements for a typical co-orbiting range are totally unrealistic using omni-antennas. Note, the scale has changed from milliwatts used in figures 36 & 37 to watts.

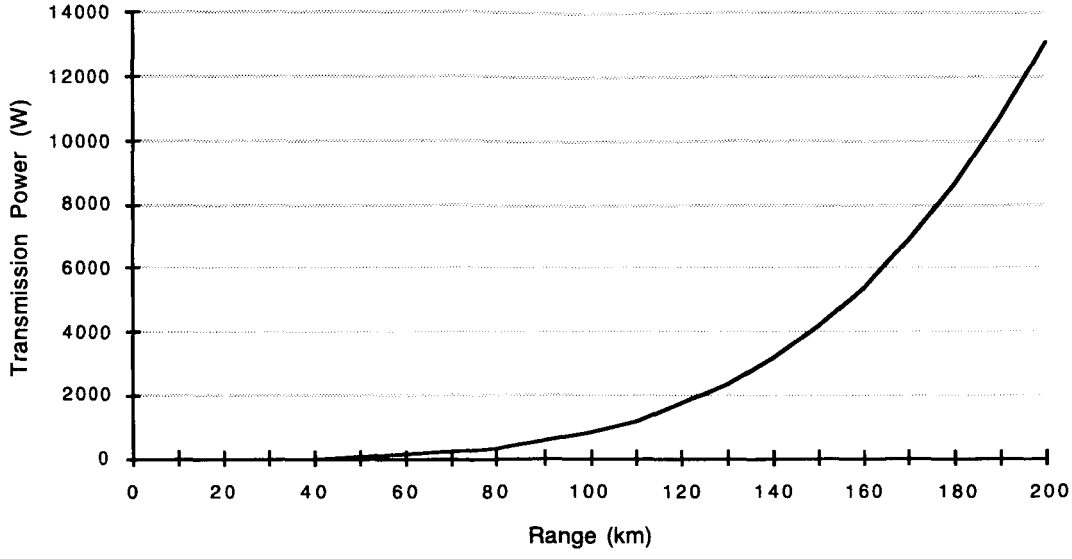

Figure 38. Passive target transmission power estimates.

The power transmission requirements can be reduced somewhat on the passive co-orbiting satellites by either changing the reflector size or using directional antennas. Sauer shows the sensitivity of the transmission power as a function of the reflector size in Reference 29. Figure 39 shows the sensitivity of the power as a function of the antenna gain. At a gain of approximately 30 (equivalent to 3 m directional antenna), the power generation estimates are still as high as 15 watts. Results from Sauer and figure 39 demonstrate that passive targets are unsuitable for gravity mapping using radiometrics.

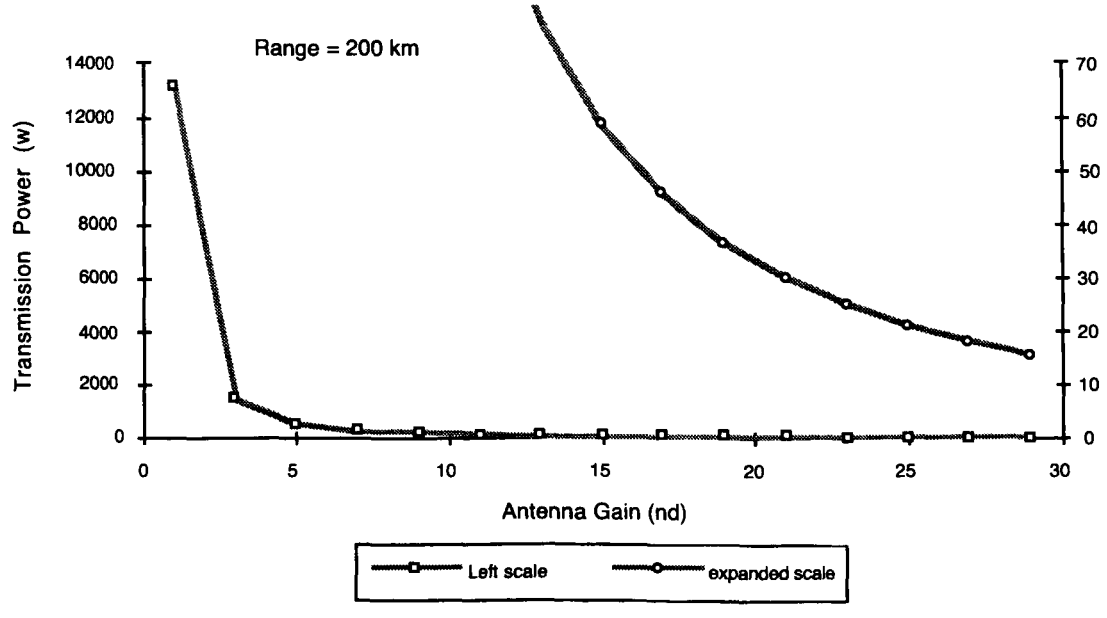

Figure 39. Passive target transmission power cost vs. antenna gain.

Conclusions

A first-cut feasibility assessment was performed on the RF transmission power requirements for the two-spacecraft and co-orbiting gravity mapping geometries. The passive target approach proved to be an unsuitable option even for co-orbiting satellites. The estimated power for an active RF system was less than a 1/5 watt for the dual Scout 500 x 7000-km elliptic relay orbit. The active co-orbiting satellite power estimate was submilliwatt.

References

1. Workshop on Early Robotic Missions to the Moon, Lunar and Planetary Institute, Houston, Texas, February 1992.

2. Wagner, Lynn A., Jr. and Sponaugle, Steve, "Lunar Scout Mission Description and Mission Assessment Document," JSC-26445, NASA, December 1993.

3. Hofmann, O., Navé., P., Ebmer., H., "DPS--A Digital Photogrammetric System for Producing Digital Elevation Models and Orthophotos by Means of Linear Array Scanner Imagery," *Photogrammetric Engineering and Remote Sensing*, Vol. 50, pp. 1135-1142, August 1984.

4. Albertz, J., Ebner, H., Heipke, C., Neukum, G., and Scholten, F., "The Camera Experiments HRSC and WAOSS on the MARS 94 Mission," *Int. Arch. of Photogrammetry and Remote Sensing*, Vol. 29, Part I, 1992.

5. Panton, D. J., "A Flexible Approach to Digital Stereo Mapping," *Photogrammetric Engineering and Remote Sensing*, Vol. 44, pp. 1499-1512, December 1978.

6. Heipke, C., Kornus, W., Strunz, G., Thiemann, R., and Colomina, I., "Automatic Photogrammetric Processing of Spot Imagery for Point Determination, DTM Generation and Orthoprojection," *Int. Arch. of Photogrammetry and Remote Sensing*, Vol. 29, Part III, 1992.

7. Ebner, H., Kornus, W., and Strunz, G., "A Simulation Study on Point Determination Using MOMS-02/D2 Imagery," *Photogrammetric Engineering and Remote Sensing*, Vol. 57, pp. 1315-1320, October 1991.

8. Kornus, W., Private Communication, 1993.

9. Konopliv, Alex S., "A 75th Degree and Order Lunar Gravity Field Based Upon Lunar Orbiters I Through V," Jet Propulsion Laboratory, unpublished results.

10. Davis, John H., "Lunar Gravitational Field Estimation and the Effects of Mismodeling Upon Lunar Satellite Orbit Prediction," Master of Science Thesis, MIT, CSDL-T-1180, June 1993.

11. Sullivan, Wendy I., "Coordinate Options for Lagrange Polynomial Trajectory Interpolation," The Charles Stark Draper Laboratory, ESB-93-585, LMI-93-022, August 16, 1993.

12. Sullivan, Wendy I., "Lunar Trajectory Interpolation Accuracy Using Lagrange Polynomials," The Charles Stark Draper Laboratory, ESB-93-416, LMI-93-014, June 29, 1993.

13. Condon, Gerald, "Polynomial Curve Fit of Lunar Trajectory Segments," JSC/ET4 Memorandum, ET4-93-12, August 12, 1993.

14. Drake, Bret, "Lunar Scout Program - Preliminary Mission Analysis (Rev 1)," NASA JSC Lunar Scout Program Office, April 1993.

15. Sauer, Birgit, "Scout II Gravity Mapping Mission: Measurement Information vs Orbital Geometry," The Charles Stark Draper Laboratory, ESB-93-462, LMI-93-015, June 29, 1993.

16. Sauer, Birgit, "Lunar Scout Gravity Mapping Mission: Surface Coverage Gaps," The Charles Stark Draper Laboratory, ESB-93-511, LMI-93-018, July 23, 1993.

17. Sauer, Birgit, "Lunar Scout Gravity Mapping Mission: Apsides Angle Study," The Charles Stark Draper Laboratory, ESB-93-539, LMI-93-019, July 29, 1993.

18. Sauer, Birgit, "Lunar Scout Gravity Mapping Mission: Wedge Angle Study," The Charles Stark Draper Laboratory, ESB-93-556, LMI-93-021, August 3, 1993.

19. Kaula, W. M., Theory of Satellite Geodosy, Blaisdell Publishing Co., 1966.

20. Rosborough, G. W., Tapley, B.D., "Radial, Transverse, and Normal Satellite Position Perturbations Due to the Geopotential," *Celestial Mechanics*, 40 (1987), pp. 409-421.

21. Wagner, C.A., "Geopotential Orbit Variations: Applications to Error Analysis," *Journal of Geophysical Research*, Vol. 92, No. B8, pp. 8136-8146, July 10, 1987.

22. Musoff, H., "Satellite Velocity Perturbations Due to the Moon Gravity Potential," The Charles Stark Draper Laboratory, ESB-93-481/Rev 1, LMI-93-016, July 20, 1993.

23. Balmino, G., Moynot, B., Vales, N., "Gravity Field of Mars in Spherical Harmonics Up to Degree and Order Eighteen," *Journal of Geophysical Research*, Vol. 87, pp. 9735-9746, November 1982.

24. Rosborough, G. W., Lemoine, F.G., "Sensitivity Studies of Mars Orbiters for Mars Gravity Recovery," *The Journal of the Astronautical Sciences*, Vol. 39, No. 3, pp. 327-357, July-September 1991.

25. Konopliv, Alex, et al., "A High Resolution Lunar Gravity Field and Predicted Orbit Behavior," Paper AAS 93-622, AAS/AIAA Astrodynamics Specialist Conference, Victoria, B.C., Canada, Aug. 16-19, 1993.

26. Sullivan, Wendy I., "Scout I Gravity Mapping Mission: Co-orbiting Subsatellite Options," The Charles Stark Draper Laboratory, ESB-93-675, LMI-93-025, October 1, 1993.

27. Abshire, James B., "Lunar Scout Laser Ranging System for Lunar Gravity Measurements," Goddard Space Flight Center Briefing, October 10, 1991.

28. Ridenoure, Rex W. (ed.), "Lunar Observer - A Comprehensive Orbital Survey of the Moon: Mission and System Definition Summary," JPL D-8607, Jet Propulsion Laboratory, California Institute of Technology, Pasadena, CA, April 15, 1991.

29. Sauer, Birgit, "Lunar Scout Gravity Mapping Mission: Radiometric Tracking Power Requirements," The Charles Stark Draper Laboratory, EGB-93-623, LMI-93-024, August 31, 1993.

Appendix A

Contents

Tables **Page**

A-1 POLAR ORBIT, SINGLE REVOLUTION, LATITUDE RANGE =±20 DEGREES A5

Figures

Page

A-1 The Position Vectors for the Central Body and 75 x 75 Gravity Model Propagations are Reinitialized in the Lunar Equatorial Region A2

A-2 Crosstrack and Downtrack Deviation of the Central Body Position Vector With Respect to the 75 x 75 Gravity Model Reference Trajectory A3

A-3 Longitudes Where Central Body and 75 x 75 Gravity Model Position Vectors Are Set Equal to Each Other To Initialize a One Rev Propagation and Computation of Crosstrack and Downtrack Deviation Angles (and Arcs) A4

A-4 Crossrange Deviation Angle (Top Plot) and Arc Distance (Bottom Plot) A6

A-5 Crossrange Deviation Angle (Top Plot) and Arc Distance (Bottom Plot) A7

Appendix A - Lunar Scout: Crossrange Movement For Evaluation Of Swath Width Overlap of the Lunar Scout Spacecraft

Author: Gerald L. Condon, NASA Johnson Space Center

Introduction

This study provides a look at the crossrange and downrange of a central body coasting propagation of the Lunar Scout as compared with a coasting propagation employing a 75 x 75 lunar gravity model (obtained from the Jet Propulsion Laboratory). The purpose of this study is to determine if the spherical harmonics in the 75 x 75 lunar gravity model perturb the coasting orbit enough to cause a gap in the swath of a German High Resolution Stereo Camera (HRSC) being used to provide a digital geodetic map of the lunar surface. Any gap in the swath would result in gores or missing pieces of the digital lunar map. A maximum crossrange variation of 0.06° is baselined for the project. This variation or error is the amount of out-of-plane angle that occurs when a central body (spherical planet) propagation is compared to a reference trajectory generated using the 75 x 75 lunar gravity model. The groundtrack of the central body propagation reflects only the angular rotation of a spherical moon. The groundtrack of the reference trajectory (75 x 75 gravity model) reflects the angular rotation of the Moon in addition to the orbital effect of a matrix of spherical (zonal, sectoral, and tessoral) harmonic coefficients. If the crossrange position/angle error, due to perturbations in the coasting trajectory caused by the lunar potential model, is less than 0.06°, then it can be combined with position/angle errors due to camera pointing uncertainty and still remain within the swath width of the camera itself. This would guarantee gore-free data.

A downrange error comparison between position vectors for the central and 75 x 75 gravity models is also included in this study as a point of interest. The downrange error, however, will not affect any requirements regarding the swath width or orientation knowledge accuracy of the camera mapper.

For both the crosstrack and the downtrack angular deviations (between the central body and the reference trajectory), a crosstrack and downtrack deviation arc is also included. The deviation arc is the arc distance along the lunar surface resulting from the deviation angle.

Approach

A 300-km altitude circular polar orbit was propagated using the 75 x 75 lunar gravity model to establish a reference trajectory. The 28.5-day orbit propagation was begun at the lunar equator at a right ascension of zero degrees. The 28.5-day propagation ensured that, given the 27.322-day sidereal rotation period, a polar orbit starting atascending nodes spanning the lunar globe would be realized. Since the swath overlap is the smallest in the region of the equator, the crossrange error data was computed only in the region of -20° to 20° latitude.

The reference trajectory was generated using a 10-second integration step size and a 75 x 75 lunar gravitational potential model. As the spacecraft, in the reference trajectory, passed through the lunar equator (from the southern to the northern hemisphere), the initial state for a central body propagation was set to be equal to that of the reference trajectory. The process of state reinitialization was repeated every revolution. The central body propagation provided a comparison to the 75 x 75 gravity propagation. The out-of-plane crosstrack and the in-plane downtrack angles were computed using the central body and the 75 x 75 gravity position vectors, for a particular point in time in the reference trajectory (see figure A-1).

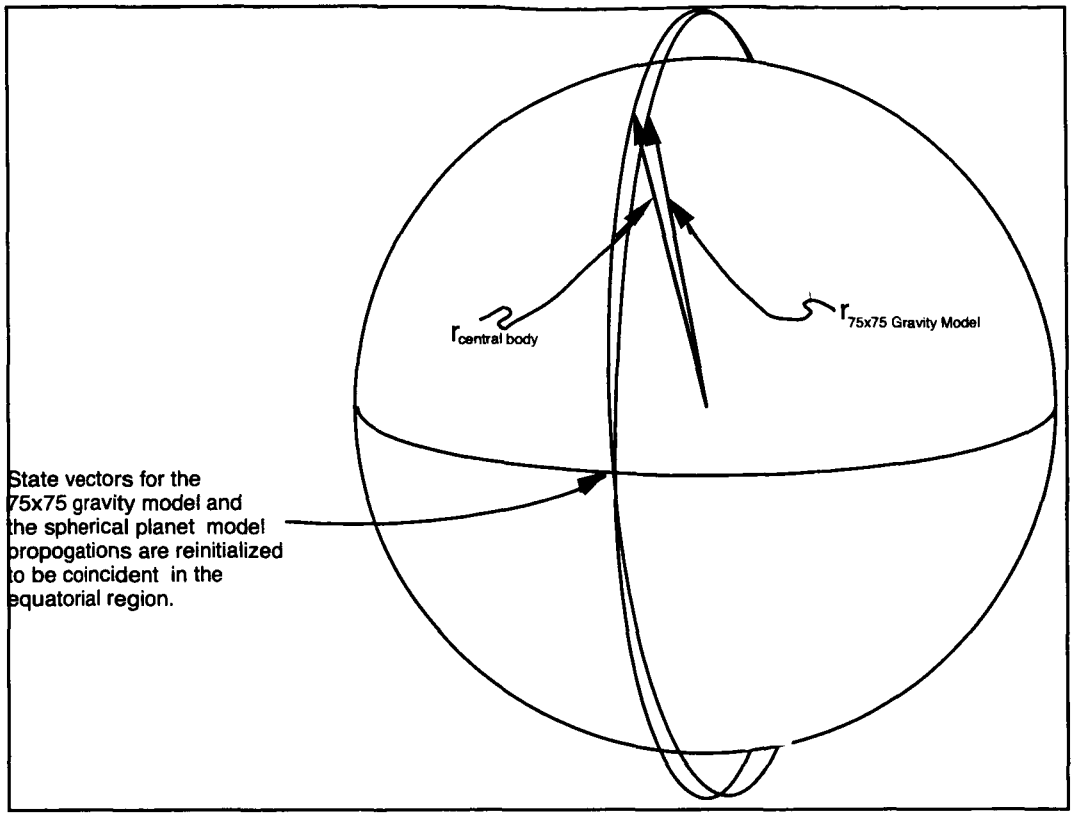

Figure A-1. The position vectors for the central body and 75 x 75 gravity model propagations are reinitialized in the lunar equatorial region.

The out-of-plane or crosstrack angle is computed using the central body propagation position vector and the 75 x 75 gravity model position and velocity vectors (see figure A-2).

$$\theta = \frac{\pi}{2} - \phi \tag{A1}$$

where

$$\hat{i}_{plane_{75}} = unit(\bar{v}_{75} \times \bar{r}_{75})$$

$$\phi = \cos^{-1}\left[\hat{r}_{central} \bullet \hat{i}_{plane_{75}}\right]$$

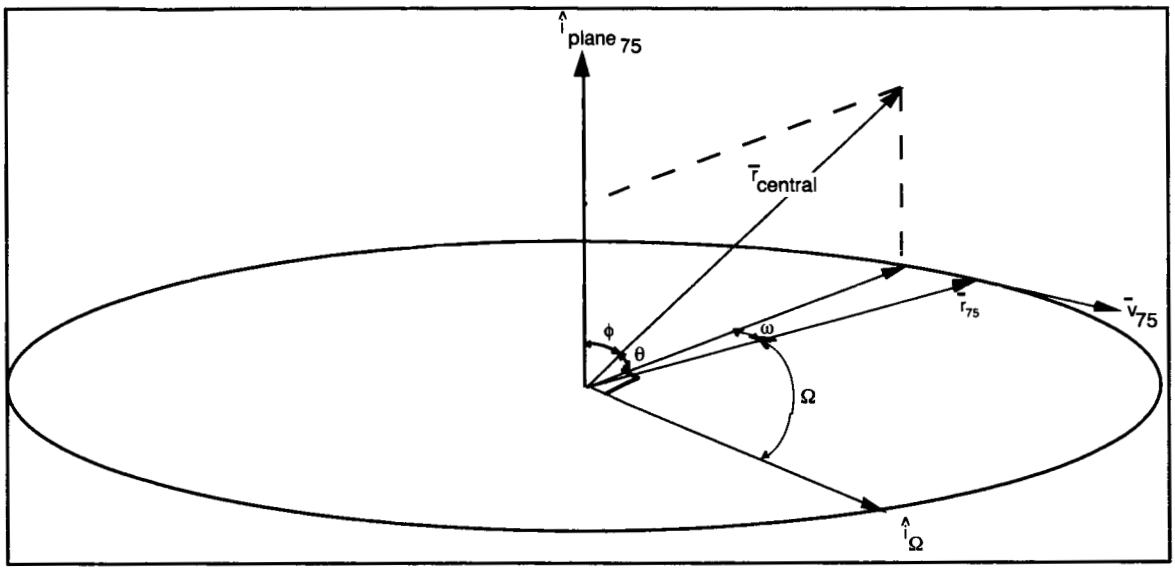

Figure A-2. Crosstrack and downtrack deviation of the central body position vector with respect to the 75 x 75 gravity model reference trajectory.

The longitude of the ascending node for the entire 28.5 days of reference trajectory propagation is shown in figure A-3. The 1-rev polar trajectory segments, which begin at the lunar equator, span all longitudes.

The in-plane or downtrack angle is computed as

$$\omega = \frac{\pi}{2} - \Omega \tag{A2}$$

where

$$\Omega = \cos^{-1}\left[\hat{r}_{75} \bullet unit\left[\bar{r}_{central} \times \hat{i}_{plane\,75}\right]\right]$$

The diagram in figure A-2 shows the crosstrack (out-of-plane) and downtrack (in-plane) deviation that the central body position vector possesses with respect to the plane (and position) of the 75 x 75 gravity model reference trajectory. Note that the actual reference trajectory is polar. The diagram is oriented horizontally for ease of viewing.

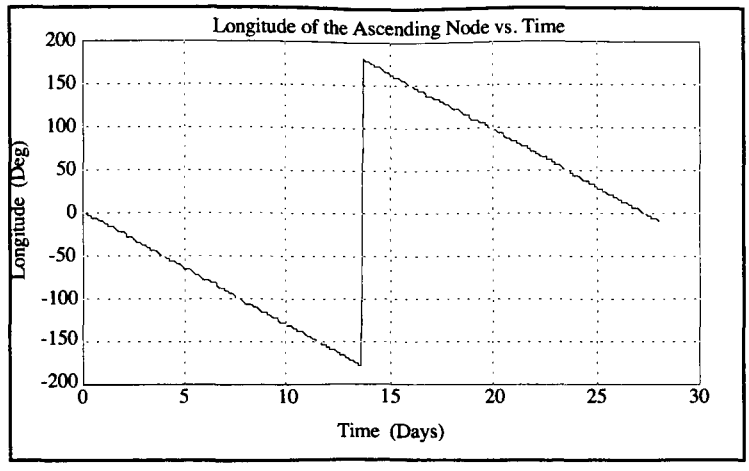

Figure A-3. Longitudes where central body and 75 x 75 gravity model position vectors are set equal to each other to initialize a 1-rev propagation and computation of crosstrack and downtrack deviation angles (and arcs).

The crosstrack and downtrack deviation angle and arc distance plots for a single rev central body propagation are included after the Conclusions in table A-1 and figures A-4, A-5.

Results and Discussion

The maximum crosstrack deviation occurs at about 170° longitude and at about -10° longitude and has a value of 0.026° (theta) or 781 m arc distance (see figure A-4). The crosstrack deviation arc is simply the amount of arc distance on the lunar surface that corresponds to a given deviation angle. The 0.026° of crosstrack deviation angle falls within the 0.06° maximum crosstrack deviation tolerance as specified by the Lunar Scout Project Office. There is a symmetry to crosstrack deviation that is 180° apart. The mean crosstrack deviation is -2.05e-05° or -0.62 m. There appears to be no monotonically increasing growth in the crosstrack deviation as a function of lunar longitude. The standard deviation for the crosstrack deviation angle (arc distance) is 4.33e-3° (131.36 m).

The maximum downtrack deviation, for the 1 rev case, is an angle of 0.285° (omega) or an arc distance of 8641 m and occurs at about -160° longitude (see figure A-5). The downtrack deviation does not seem to have the same type of 180° longitudinal symmetry that the crossrange deviation has. The standard deviation for the downrange deviation angle (arc distance) is 2.99e-2° (908.13 m). The downtrack deviation has been included as a point of interest as there is no downtrack deviation maximum tolerance set by the Lunar Scout Project Office.

Conclusions

The maximum crosstrack deviation angle of 0.026° does not exceed the maximum tolerance of 0.06° as specified by the Lunar Scout Project Office. Based on the results of this study and the accompanying assumptions, the swath of the lunar camera mapper spacecraft will always overlap. There will be no gores in the data due to the lunar gravitational potential perturbing the spacecraft's orbit enough to cause the swath of the camera not to overlap in certain areas.

TABLE A-I. Polar Orbit, Single Revolution, Latitude Range = +20°

Statistical Parameters

Polar Orbit
Latitude Range +/-20°
28.5-Day Reference Orbit Propagation

1 Revolution

Mean Crosstrack (Out of Plane) Angle	=	-2.04857e-05°
Standard Deviation of Crosstrack Angle	=	0.00433038°
Maximum Crosstrack (Out of Plane) Angle	=	0.0257457°
Mean Crosstrack (Out of Plane) Arc	=	-0.621411 m
Standard Deviation of Crosstrack Arc	=	131.357 m
Maximum Crosstrack (Out of Plane) Arc	=	780.966 m
Mean Downtrack (Out of Plane) Angle	=	0.0057231°
Standard Deviation of Downtrack Angle	=	0.0299378°
Maximum Downtrack (Out of Plane) Angle	=	0.284858°
Mean Downtrack (Out of Plane) Arc	=	173.603 m
Standard Deviation of Downtrack Arc	=	908.127 m
Maximum Downtrack (Out of Plane) Arc	=	8640.82 m

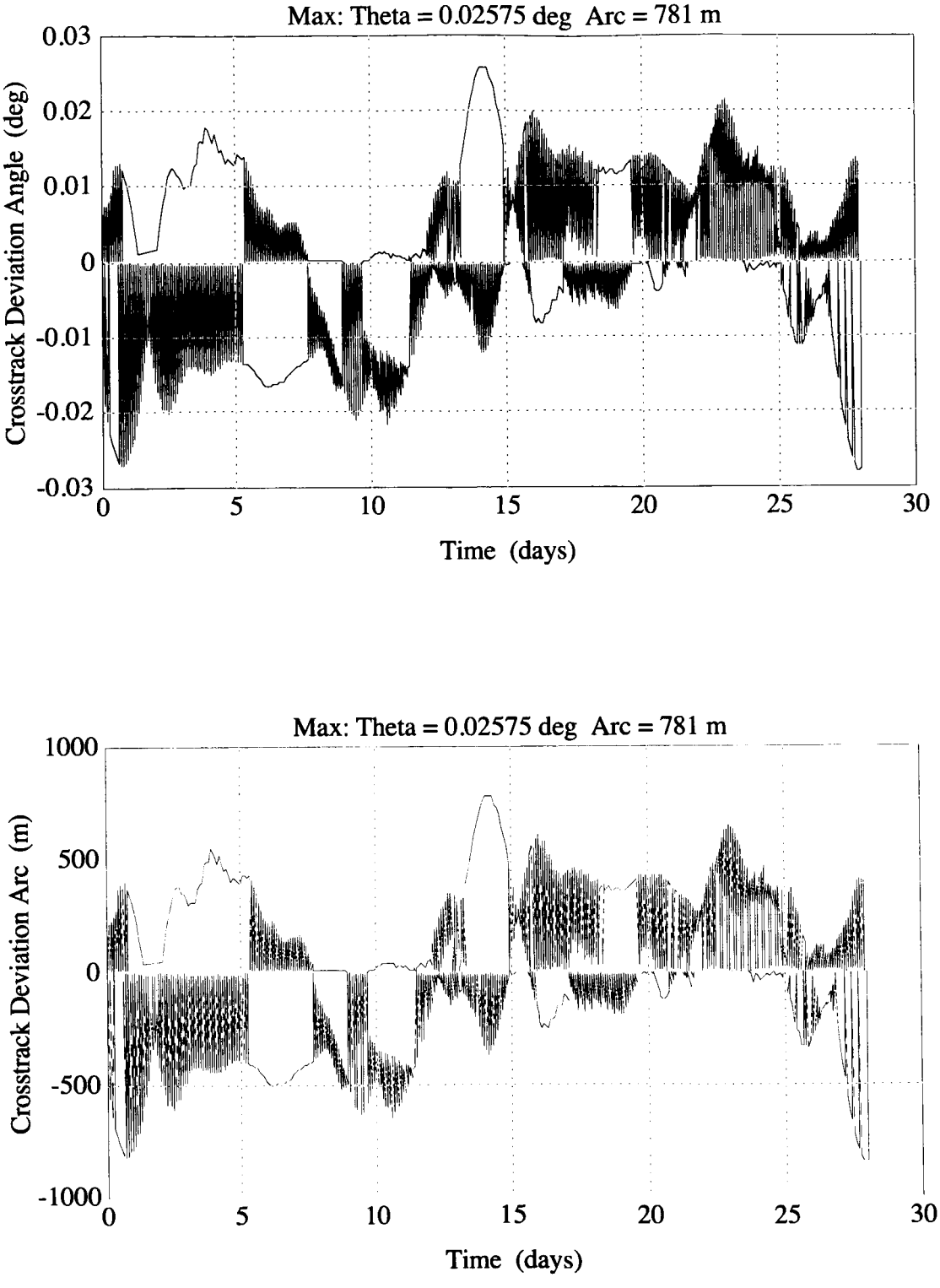

Figure A-4. Crossrange deviation angle (top plot) and arc distance (bottom plot).

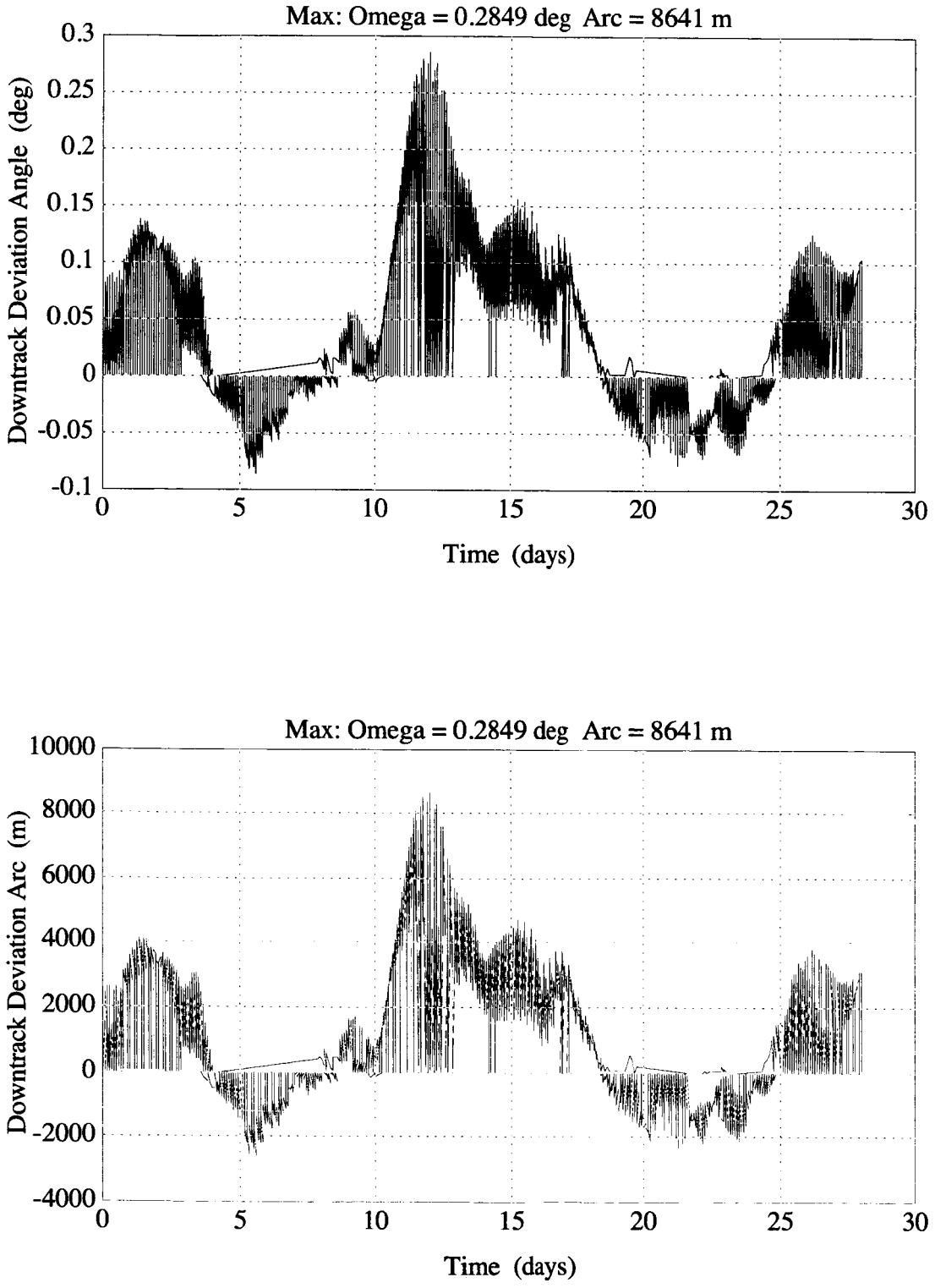

Figure A-5. Crossrange deviation angle (top plot) and arc distance (bottom plot).

Appendix B

Contents

Figures

		Page
B-1	Polar and 30 Degree Inclined Truth Model Trajectories	B2
B-2	Curve Fit of Reference Trajectory Arc Segment	B3
B-3	Cartesian and Spherical Elements for a One Rev Polar Spacecraft Reference Orbit Trajectory with a 340 Degree Ascending Node	B5
B-4	Position Errors for a 500-Second Polar Spacecraft Orbit Trajectory with 2nd, 3rd, and 4th Order Curve Fits	B6
B-5	Position Errors for a 1 Rev Polar Spacecraft Orbit Trajectory with 2nd, 3rd, and 4th Order Curve Fits	B7
B-6	Position Errors for a 1 Rev Polar Spacecraft Orbit Trajectory for 3rd Order Curve Fits Using Cartesian Elements and Using Spherical Elements	B7
B-7	Cartesian and Spherical Elements for a One Rev 30 Degree Inclined Spacecraft Reference Orbit Trajectory with a 340 Degree Ascending Node	B8
B-8	Position Errors for a 30 Degree 1 Rev 340 Degree Ascending Node Reference Trajectory	B9
B-9	Maximum Position Error as a Function of Integration Step Size	B9

Appendix B - Polynomial Curve Fit of Lunar Trajectory Segments

Author: Gerald L. Condon, NASA Johnson Space Center

Introduction

This study provides a comparison of position errors that occur when a polynomial curve fit is applied to varied lengths of segments of a lunar trajectory (Ref. 1). The Lunar Scout mission will attempt to create a digital geodetic map of the lunar surface using a German High Resolution Stereo Camera (HRSC). As a part of the photogrammetric reconstitution process, a series of time-tagged exterior orientation parameters, calculated at discrete orientation image points, are simultaneously combined in a least squares approximation. In between the orientation image points, the exterior orientation parameters are expressed as functions of adjacent orientation images. The Germans currently plan to model these functions as 3rd order polynomial curve fits. It is desirable to make the interval distance between orientation images large, while maintaining a position error below a specified 1 meter tolerance, as this enhances the stability of the least squares approximation. In the case of this study, the problem is to assess how far apart the orientation images can be spaced so that a polynomial curve fit accurately (within 1 meter) models the reference lunar orbit trajectory or truth model. The position error is the difference between the position on the reference trajectory for a given time and the polynomial curve fit value of the position, for that same time. A one-revolution (8256 second) coast arc was considered for both the polar (90° and the 30°inclined orbits. A subset of the 1-rev circular polar reference trajectory, the first 500 seconds only, was also used.

Approach

Generate Truth Model Trajectory

The polynomial curve fit results are to be compared against a reference trajectory or "truth model" which uses a 75 x 75 lunar spherical harmonic gravity model (obtained from the Jet Propulsion Laboratory). For this study, the position vectors generated by this gravity model are known as the true position. The truth model trajectory is a 1-revolution 300-km circular polar lunar orbit with a node at 340° west longitude (see figure B-1). It was anticipated that large perturbations in the sectoral and tessoral harmonics of the 75 x 75 gravity model should occur for a polar orbit with this node, so it was chosen as a more stressful case. A 30° inclined reference trajectory was also generated for use in this study.

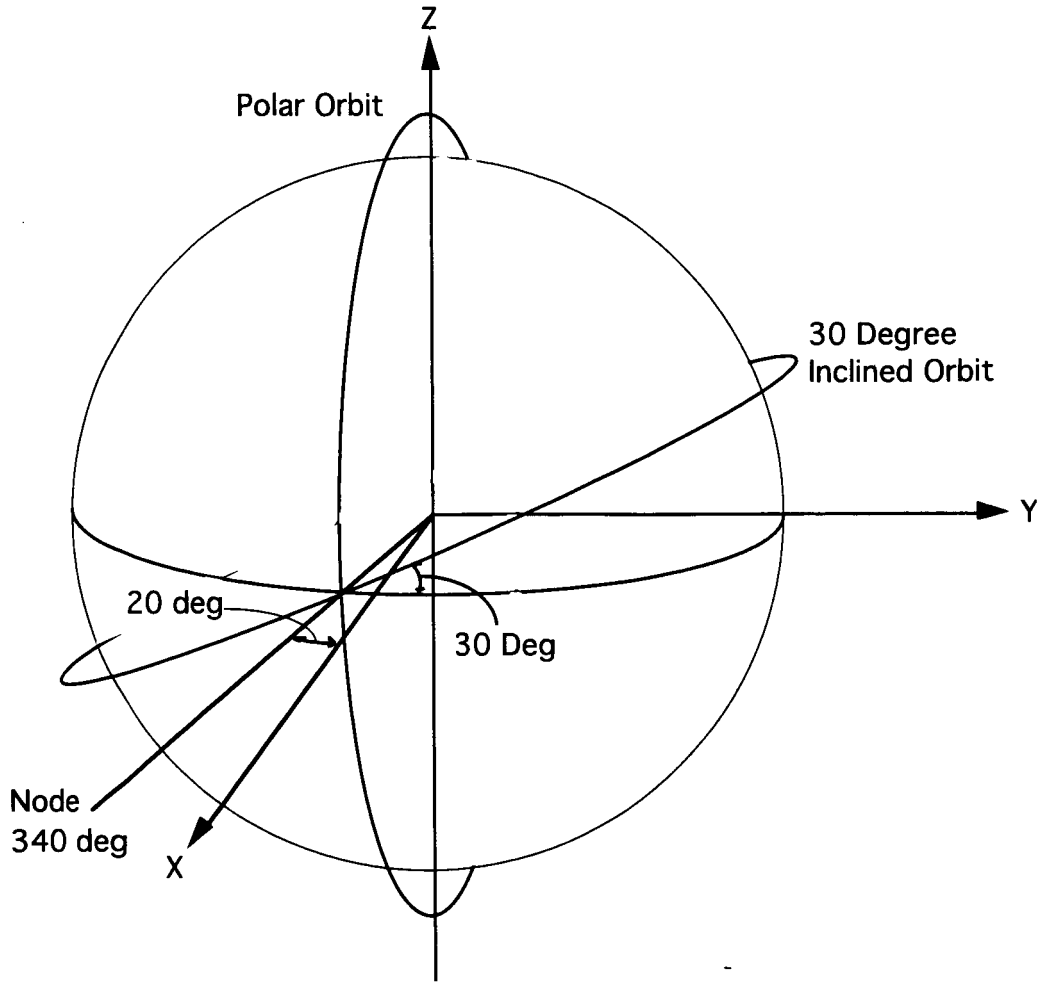

Figure B-1. Polar and 30° inclined truth model trajectories.

Select Polynomial Curve Fit Routine For Comparison Against Truth Model

Curve fitted trajectory arc segments varied in length from 2km to 100 km. Arc lengths specified for study were 2, 4, 10, 20, and 40 km. Arc lengths of 60, 80, and 100 km were added to generate a reasonable envelope of data on both the high and low sides of the specified maximum orientation image arc length of 40 km.

Though a 3rd order fit was of prime interest, a 2nd and a 4th order fit were also included to provide error trend information dependent on the order of the fit. The anchor points for the curve fit are the orientation images. The number of orientation images required is determined by the order of the curve fit (e.g., a 3rd order fit would require four anchor points or orientation images). Figure B-2 shows a section of the reference trajectory or truth model being curve fit with a 3rd order polynomial using the indicated orientation image points as anchor points for the curve fit.

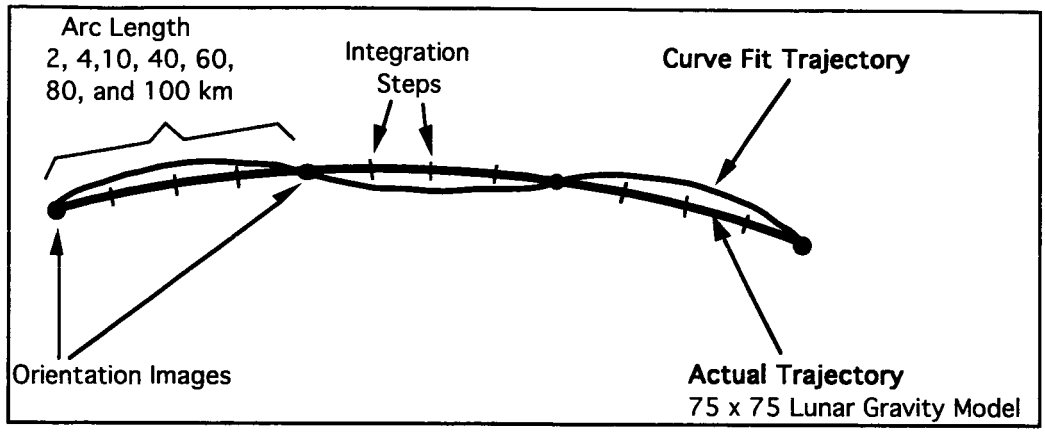

Figure B-2. Curve fit of reference trajectory arc segment.

Two curve fit approaches were used in this study to assess any effect of curve fitting technique on position error. One technique used is a Lagrange polynomial approach as proposed by the Germans. Equation B-1 represents the interpolated position as a function of time using the Lagrange interpolation.

$$P_n(t) = \sum_{i=0}^{n} P(t_i) \prod_{\substack{j=0 \\ j \neq i}}^{n} \frac{t - t_j}{t_i - t_j} \tag{B-1}$$

A matrix-vector approach also assessed was a Vandermonde matrix approach (equation B-2).

$$\begin{bmatrix} 1 & t_0 & t_0^2 & \dots & t_0^n \\ 1 & t_1 & t_1^2 & \dots & t_1^n \\ 1 & . & . & & \\ 1 & . & . & & \\ 1 & t_n & t_n^2 & \dots & t_n^n \end{bmatrix} \begin{bmatrix} P_0 \\ P_1 \\ . \\ . \\ P_n \end{bmatrix} = \begin{bmatrix} P(t_0) \\ P(t_1) \\ . \\ . \\ P(t_n) \end{bmatrix}$$

The interpolated position as a function of time, P(t) is obtained by inverting the square matrix (equationB-3).

$$\begin{bmatrix} P_0 \\ P_1 \\ . \\ . \\ P_n \end{bmatrix} = \begin{bmatrix} 1 & t_0 & t_0^2 & \dots & t_0^n \\ 1 & t_1 & t_1^2 & \dots & t_1^n \\ 1 & . & . & & \\ 1 & . & . & & \\ 1 & t_n & t_n^2 & \dots & t_n^n \end{bmatrix}^{-1} \begin{bmatrix} P(t_0) \\ P(t_1) \\ . \\ . \\ P(t_n) \end{bmatrix} \tag{B-3}$$

The position coefficients ($P_0, P_1, P_2, \ldots$) are computed to determine the position as a function of time (equation B-4).

$$P(t) = P_0 + P_1 t + \ldots + P_n t^n \qquad \text{(B-4)}$$

In the matrix-vector or matrix inversion approach, inversion of the square matrix would only have to be done once for an entire 1-rev trajectory if the integration step size remained exactly the same throughout the trajectory (no machine error). To determine if this process was sensitive to machine error, interpolations were performed for cases where the square matrix was only inverted once and for cases where the square matrix was inverted for every interpolated trajectory segment. In the single matrix inversion approach, the position coefficients would only be calculated once and the interpolation process would consist merely of performing the operations in equations B-3 and B-4.

Cartesian vs. Spherical Interpolation

It has been suggested that interpolation of spherical elements would produce a smaller position error than interpolation of Cartesian elements. A comparison of position error was performed for interpolations using both Cartesian elements (x, y, and z) and spherical elements (radius magnitude, latitude, and longitude). In each case, the output was expressed in Cartesian coordinates to provide a common basis of comparison. Output was also expressed in terms of downrange, crossrange, and radial components.

Position Error Sensitivity to Integration Step Size

Part of this study addresses the sensitivity of position error to the integration step size. For this study, a nominal integration step size of 0.3223035 seconds was used. This step size was chosen because it provided four interior integration steps for the minimum arc distance between orientation images (2km). This allows for at least three position error comparisons between each orientation image. The diagram in figure B-2 shows the actual curve fit approach used for a 2-km arc (between orientation images), using the integration step size of 0.3223035 seconds. Note that a 3rd order fit requires four reference or anchor points (as depicted in the diagram). A 2nd and a 4th order fit would require 3 and 5 anchor points, respectively.

Results and Discussion

Matrix Inversion vs. Lagrange Polynomial Curve Fitting Techniques

For all cases studied, there was excellent agreement in results between the matrix inversion and the Lagrange polynomial curve fitting techniques. For a constant integration step size, the matrix inversion approach is less computation intensive. There is only one matrix inversion executed to obtain the polynomial coefficients used in the curve fit (see equation B-3). These coefficients could be reused for each successive trajectory segment being fitted. The Lagrange polynomial approach uses 24 multiplication and 4 division operations to compute the 4 coefficients used in a 3rd order polynomial curve fit. If the integration step size were variable, the matrix inversion operation in the matrix inversion approach would have to be executed each time a new set of coefficients is computed.

Cartesian vs. Spherical Curve Fits

For the 1-rev polar orbit, curve fits of the Cartesian elements were more well-behaved than curve fits of the spherical elements. The poor behavior occurs when curve fitting is attempted across discontinuities in the spherical elements. Figure B-3 shows the Cartesian and the spherical elements for a 1-rev polar trajectory. The Cartesian elements are continuous and well-suited for curve fitting. With the spherical elements, however, the longitude abruptly changes from -20° to 160° longitude at about 2100 seconds. One way to bypass this problem is to block out data in the region of these discontinuities. For this study, data was blocked out for the spherical curve fitting in the region where the latitude is greater than 80° or less than -80°. This helped to alleviate the spikes in position error.

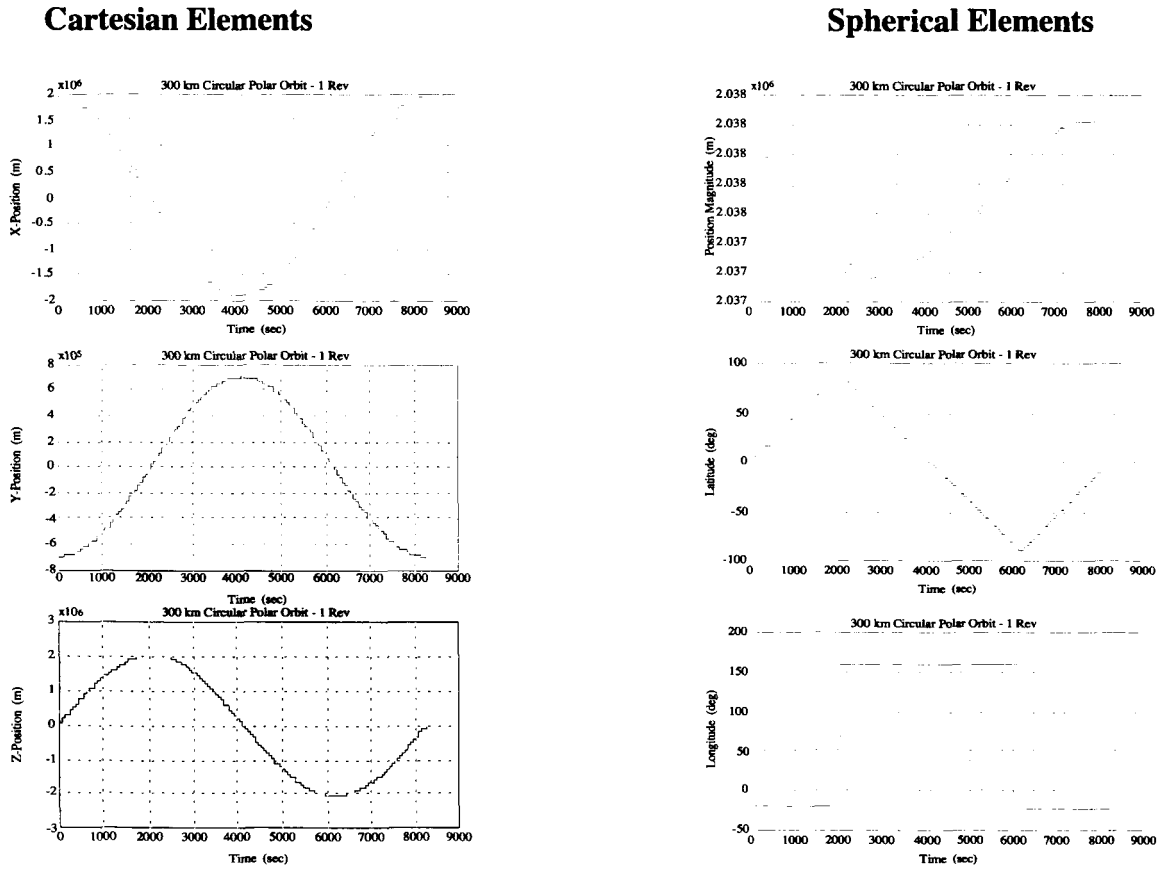

Figure B-3. Cartesian and spherical elements for a 1-rev polar spacecraft reference orbit trajectory with a 340° ascending node.

Position errors for a 500-second polar trajectory were computed for a 2nd, 3rd, and 4th order curve fit of both Cartesian and spherical elements (see figure B-4). There are no spherical element discontinuities in this region. The plots of the 500 second trajectory (figure B-4) show that, indeed, the position errors due to curve fitting the spherical elements are smaller than those of the Cartesian elements.

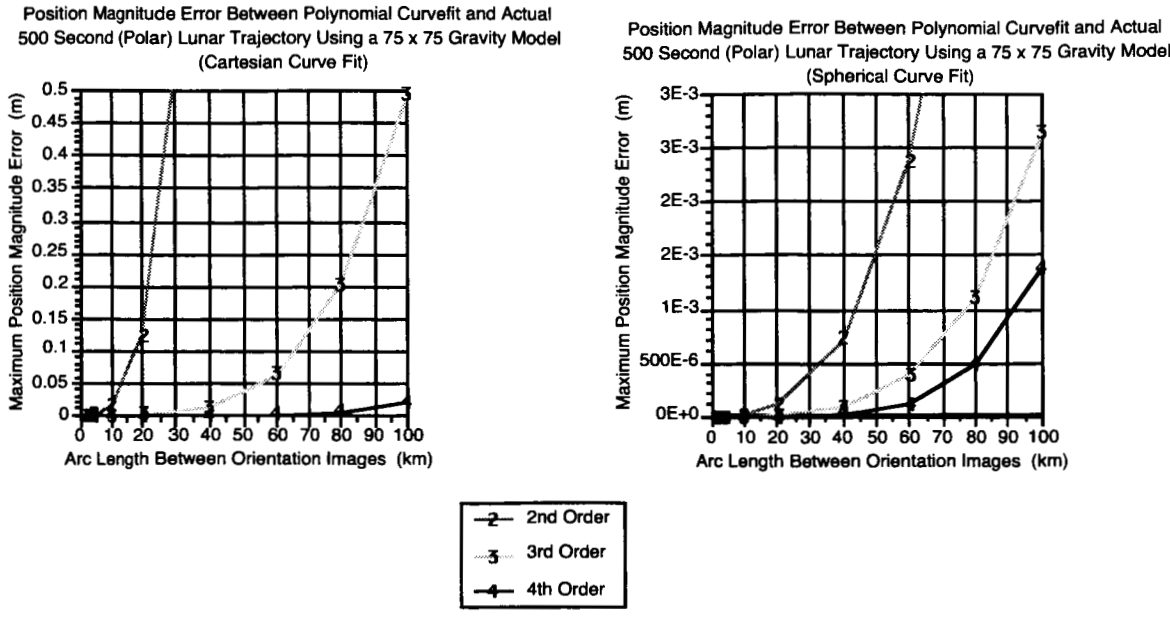

Figure B-4. Position errors for a 500-second polar spacecraft orbit trajectory with 2nd, 3rd, and 4th order curve fits.

There was excellent agreement between the various types of curve fitting approaches used [i.e., matrix inversion or Vandermonde matrix approach (cycled or non-cycled) or the Lagrange polynomial approach]. Given a constant integration step size, all approaches yielded essentially the same position error values. The position error was not affected by the method of curve fitting used.

The precision of the numbers used in the generation of the reference trajectory is of particular importance. A single precision (8-digit accuracy) reference trajectory was initially used and proved to be inadequate as it caused the curve fit position errors to be erroneously large. This problem was solved when a double precision reference trajectory was used.

The position errors obtained from the Cartesian curve fit of a 1-rev polar reference trajectory with a -20° ascending node (see figure B-5) agreed very closely with the position error sampling of the first 500 seconds of the same reference trajectory. The maximum position error magnitude remained consistent whether sampling either the first 500 seconds or an entire revolution of the circular polar reference trajectory.

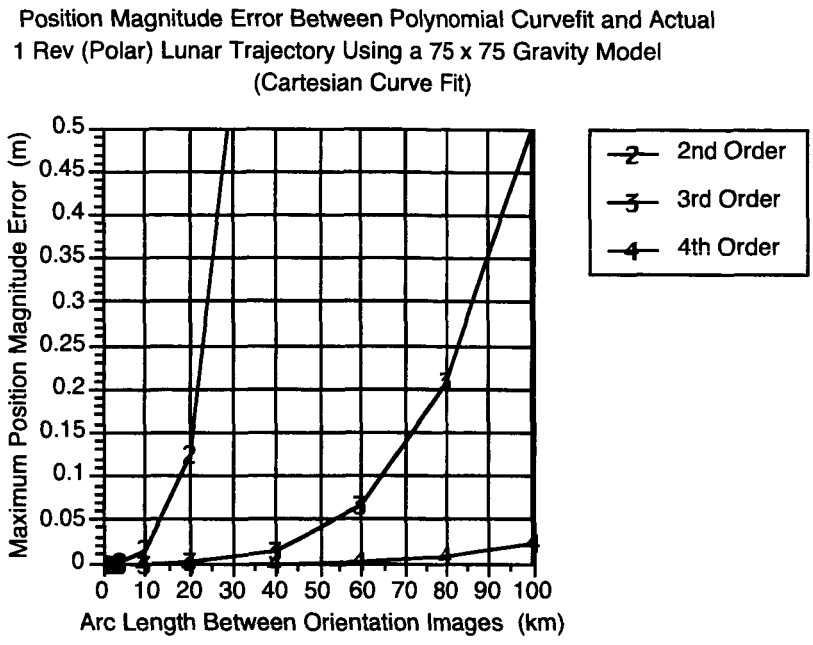

Figure B-5. Position errors for a 1-rev polar spacecraft orbit trajectory with 2nd, 3rd, and 4th order curve fits.

The 3rd order Cartesian and spherical element curve fit position errors for the above mentioned reference trajectory or truth model are shown in figure B-6. The position errors for the 3rd order curve fit based on spherical elements are normally large in the region of the longitude discontinuity and are reduced by imposing a 20° longitude range (latitudes > 80° or < -80°) where the position errors are set to zero. The spherical position errors can be further reduced by increasing this range. This is not necessarily desirable since portions of the data are blocked out and a full 1-rev sample of the reference trajectory is not used. For position determination using the above mentioned techniques, it is desirable that the reference trajectory elements be continuous.

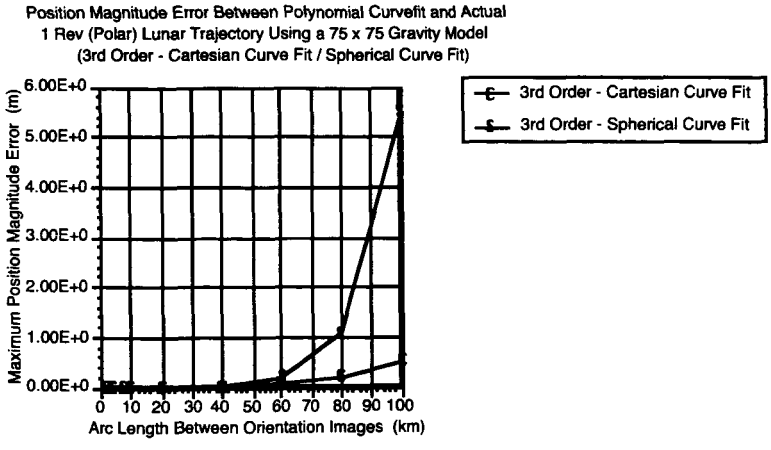

Figure B-6. Position errors for a 1-rev polar spacecraft orbit trajectory for 3rd order curve fits using Cartesian elements and using spherical elements.

In the case of a single rev 30° inclined circular reference trajectory with a 340° ascending node (see figure B-7), the longitude discontinuities (found in the polar reference trajectory) are eliminated. Further, the latitude, though not discontinuous in either case, has a more gentle transition in the case of the 30° inclined reference trajectory. The position errors for Cartesian and spherical element curve fits could be more efficiently compared with the absence of discontinuities in all of the elements.

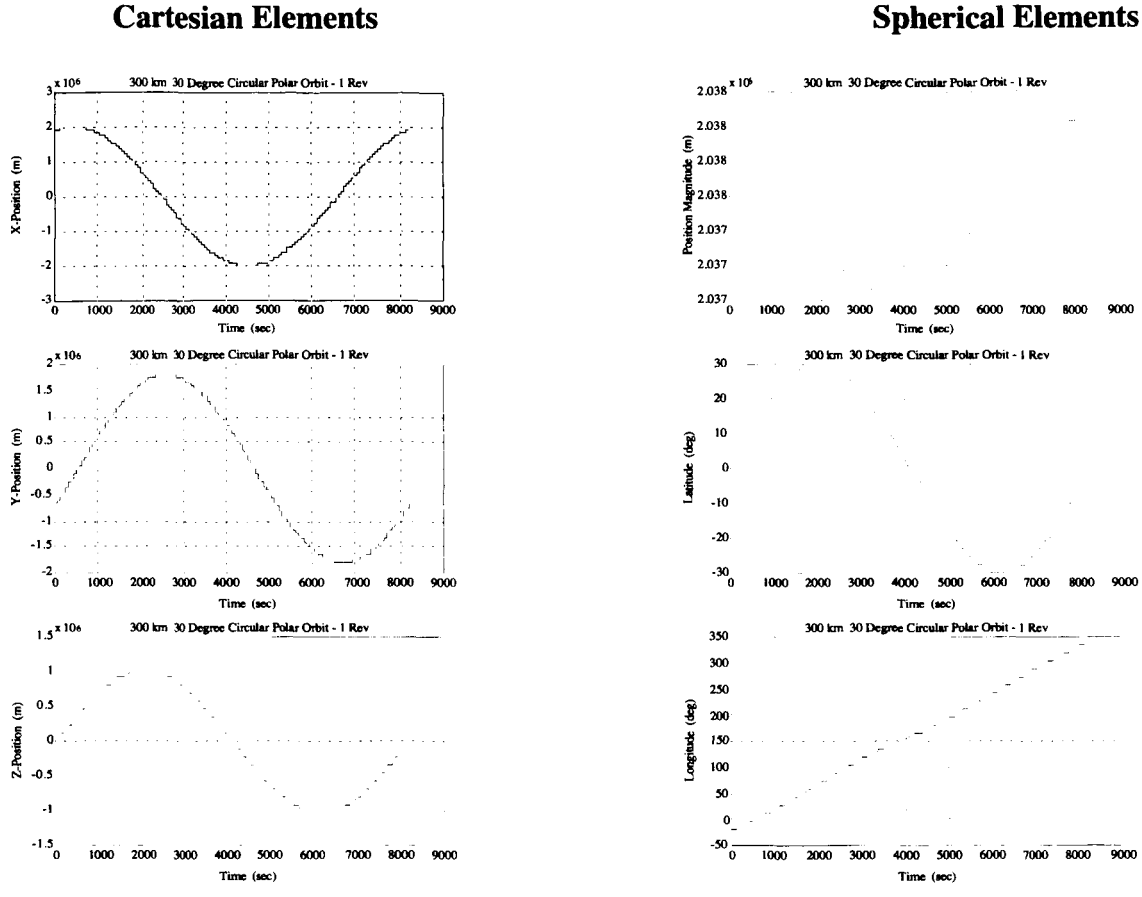

Figure B-7. Cartesian and spherical elements for a 1-rev 30° inclined spacecraft reference orbit trajectory with a 340° ascending node.

Both the Cartesian and spherical curve fit approaches fall below the 1 m position error tolerance for up to a 100-km arc length between orientation images (figure B-8). For the Cartesian element fit, the maximum position error is about 0.5 m at a 100-km arc length and 0.75 m for the spherical element fit. For the 3rd order technique, the Cartesian element fit produced smaller maximum position errors than the spherical element fit. This was also the case for the 4th order techniques. The 2nd order fits, however, showed lower maximum position errors for the spherical element fits versus the Cartesian element fits.

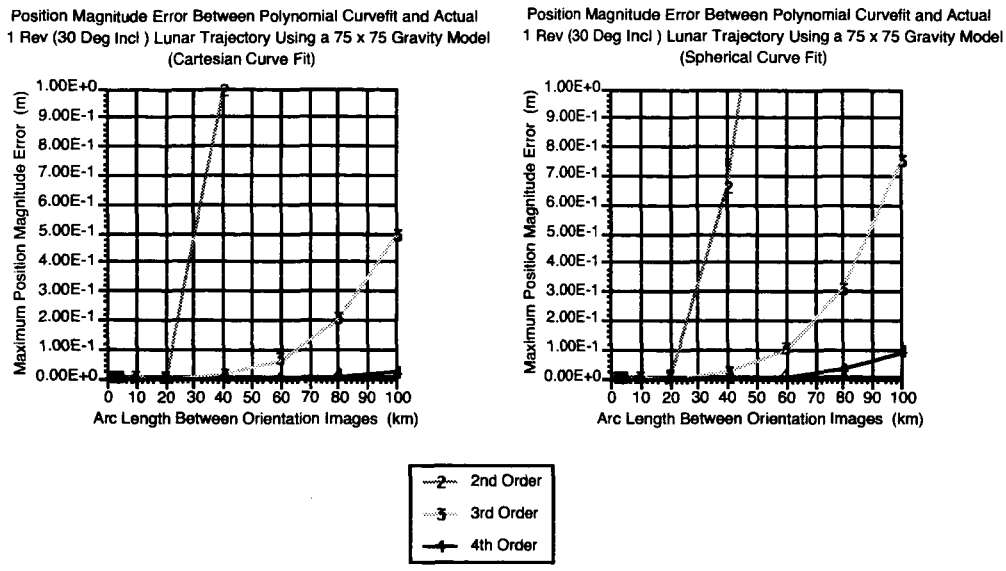

Figure B-8. Position errors for a 30° 1-rev 340° ascending node reference trajectory.

Position Error Sensitivity to Integration Step Size

The plots in figure B-9 show the maximum position error as a function of integration step size for a 500 second circular polar reference trajectory. For the selected 2-, 40-, and 80-km arc length between orientation images, the position error magnitude for 0.080-, 0.161-, and 0.322-second integration step sizes are very consistent. The integration step size for these cases does not affect the position error magnitude. The 0.322-second step size was used to generate the reference trajectories in this study. Based on the results of this part of the study, the position error magnitudes would not noticeably be reduced by employing a smaller integration step size.

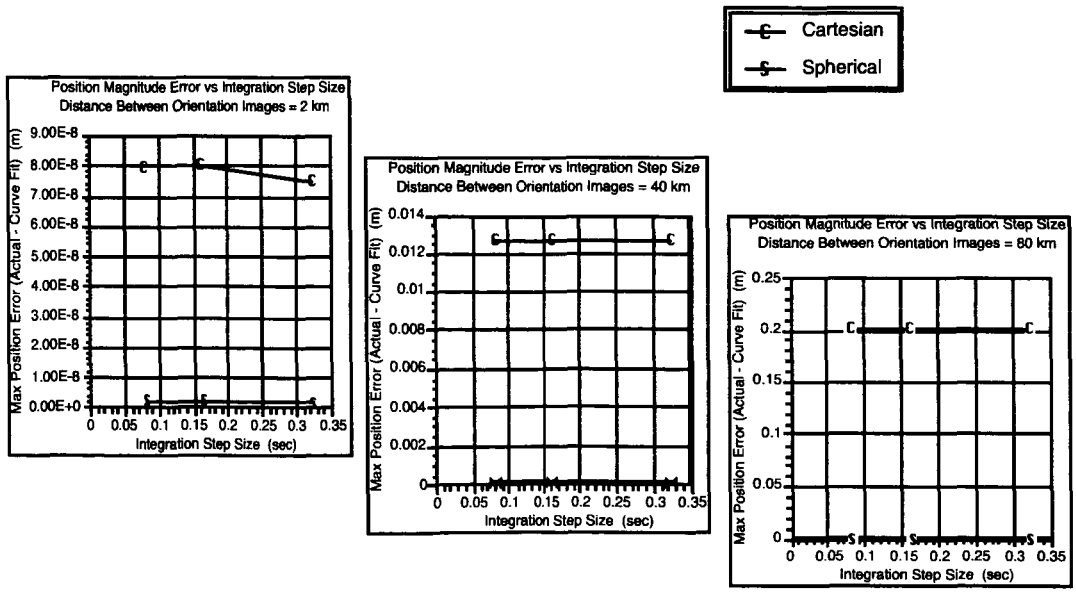

Figure B-9. Maximum position error as a function of integration step size.

Plots of the various position parameters are included in the Conclusion below for two cases. The first case is for a 40-km orientation image arc length with a Cartesian element curve fit of a 1-rev circular polar reference trajectory. The second case is also for a 40-km orientation image arc length with a Cartesian element curve fit of a 1-rev circular 30° inclination circular polar reference trajectory. The orbit altitudes for both trajectories are 300 km.

Conclusions

The 3rd order polynomial curve fit produces a position error less than the 1 m specified tolerance for arc distances between orientation images up to 100 km. Curve fitting the Cartesian elements of a reference trajectory or truth model is satisfactory to provide the required position magnitude errors. The spherical elements would produce a smaller position error if a lower order polynomial curve fit (i.e., 2nd order fit) were used. Also, for the integration step sizes examined, there is no significant effect of integration step size (of a reference trajectory) on position error.

Case 1:
- 40-km Orientation Image Arc Length
- Cartesian Element Curve Fit
- 1-Rev Circular 300 km Polar Reference Trajectory

Case 2:
- 40-km Orientation Image Arc Length
- Cartesian Element Curve Fit
- 1-Rev Circular 300-km 30° Inclined Reference Trajectory

Case 1

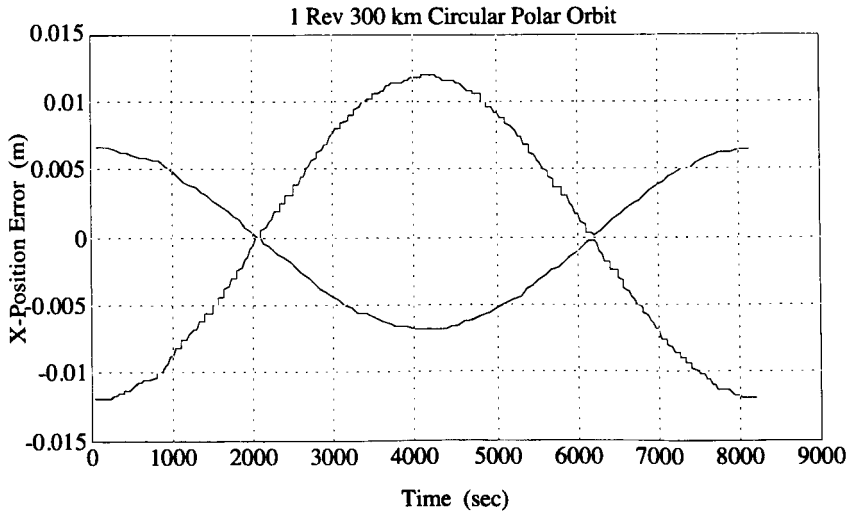

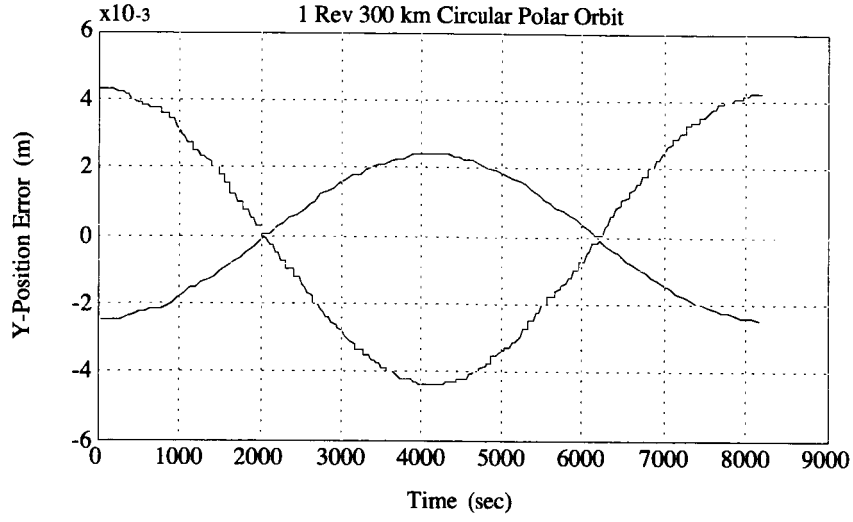
x10-3
1 Rev 300 km Circular Polar Orbit
Y-Position Error (m)
6
4
2
0
-2
-4
-6
0
1000
2000
3000
4000
5000
6000
7000
8000
9000
Time (sec)

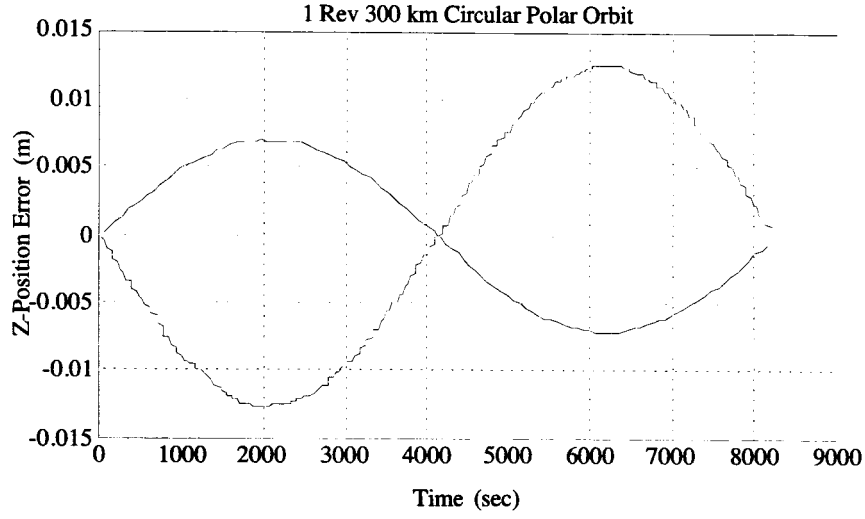
1 Rev 300 km Circular Polar Orbit
Z-Position Error (m)
0.015
0.01
0.005
0
-0.005
-0.01
-0.015
0
1000
2000
3000
4000
5000
6000
7000
8000
9000
Time (sec)

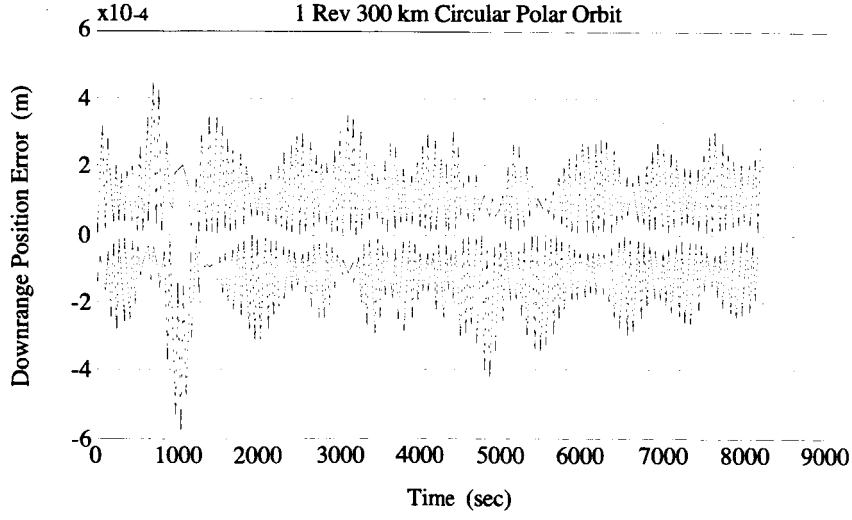
x10-4
1 Rev 300 km Circular Polar Orbit
Downrange Position Error (m)
6
4
2
0
-2
-4
-6
0
1000
2000
3000
4000
5000
6000
7000
8000
9000
Time (sec)

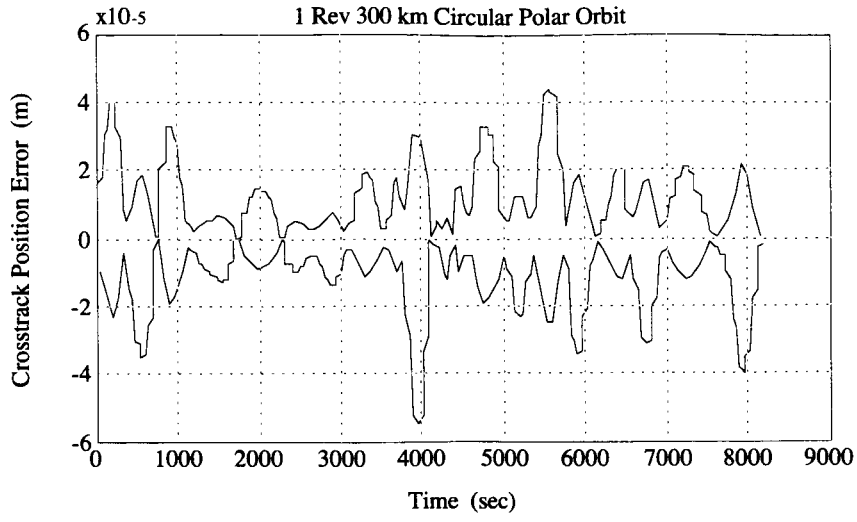
x10-5
1 Rev 300 km Circular Polar Orbit
Crosstrack Position Error (m)
6
4
2
0
-2
-4
-6
0
1000
2000
3000
4000
5000
6000
7000
8000
9000
Time (sec)

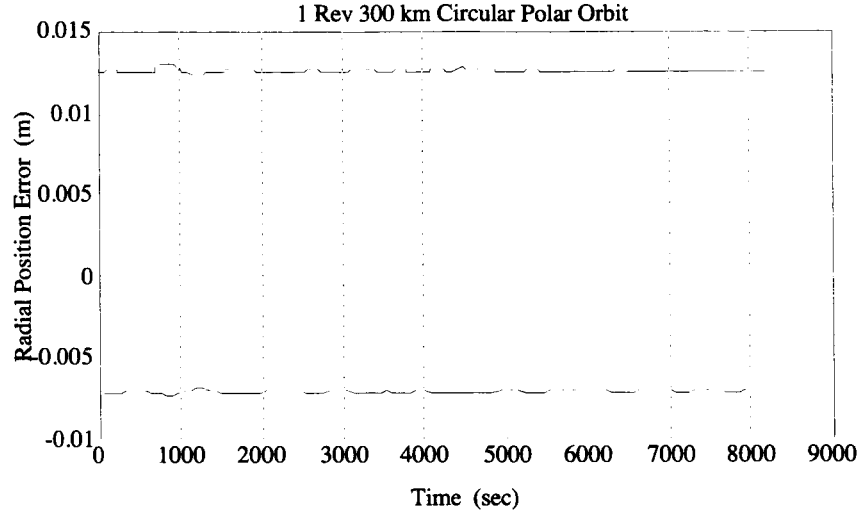
1 Rev 300 km Circular Polar Orbit
Radial Position Error (m)
0.015
0.01
0.005
0
-0.005
-0.01
0
1000
2000
3000
4000
5000
6000
7000
8000
9000
Time (sec)

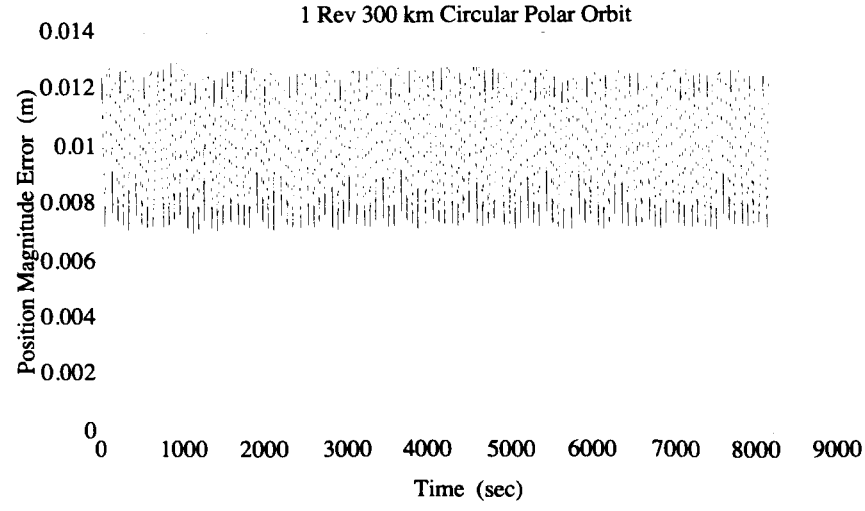
1 Rev 300 km Circular Polar Orbit
Position Magnitude Error (m)
0.014
0.012
0.01
0.008
0.006
0.004
0.002
0
0
1000
2000
3000
4000
5000
6000
7000
8000
9000
Time (sec)

Case 2

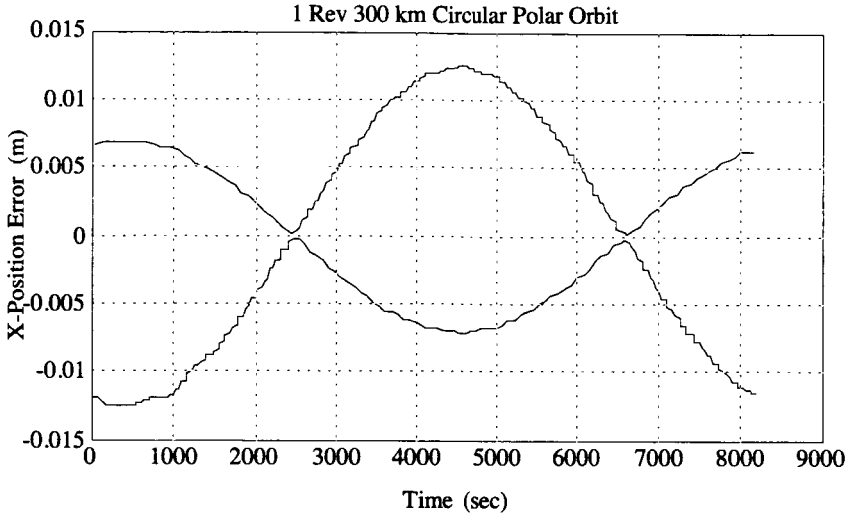
1 Rev 300 km Circular Polar Orbit
X-Position Error (m)
0.015
0.01
0.005
0
-0.005
-0.01
-0.015
0
1000
2000
3000
4000
5000
6000
7000
8000
9000
Time (sec)

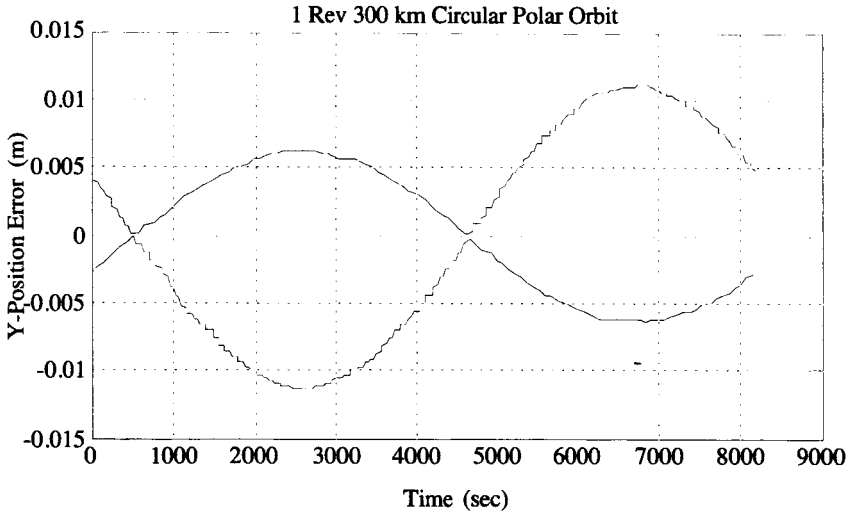
1 Rev 300 km Circular Polar Orbit
Y-Position Error (m)
0.015
0.01
0.005
0
-0.005
-0.01
-0.015
0
1000
2000
3000
4000
5000
6000
7000
8000
9000
Time (sec)

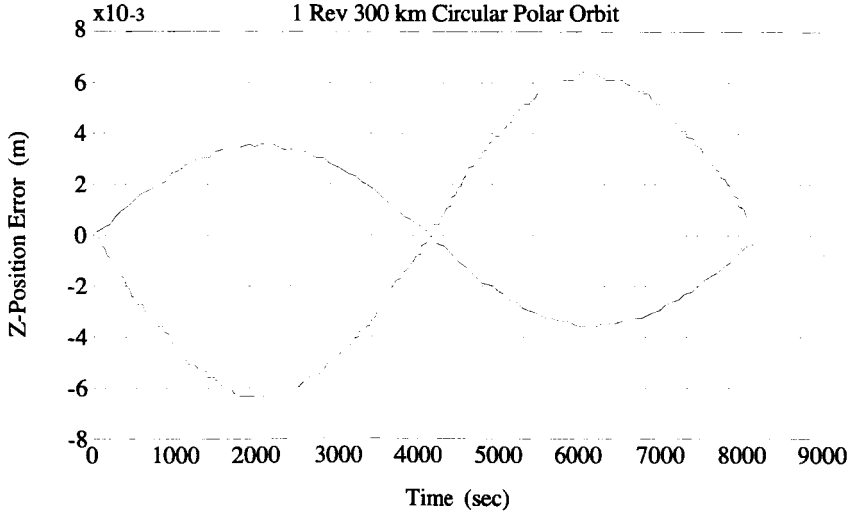
x10-3
1 Rev 300 km Circular Polar Orbit
Z-Position Error (m)
8
6
4
2
0
-2
-4
-6
-8
0
1000
2000
3000
4000
5000
6000
7000
8000
9000
Time (sec)

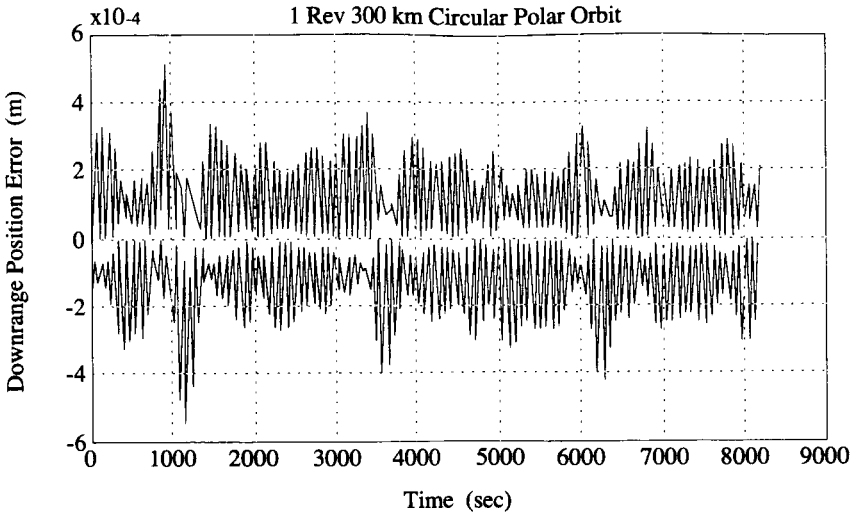
x10-4
1 Rev 300 km Circular Polar Orbit
Downrange Position Error (m)
6
4
2
0
-2
-4
-6
0
1000
2000
3000
4000
5000
6000
7000
8000
9000
Time (sec)

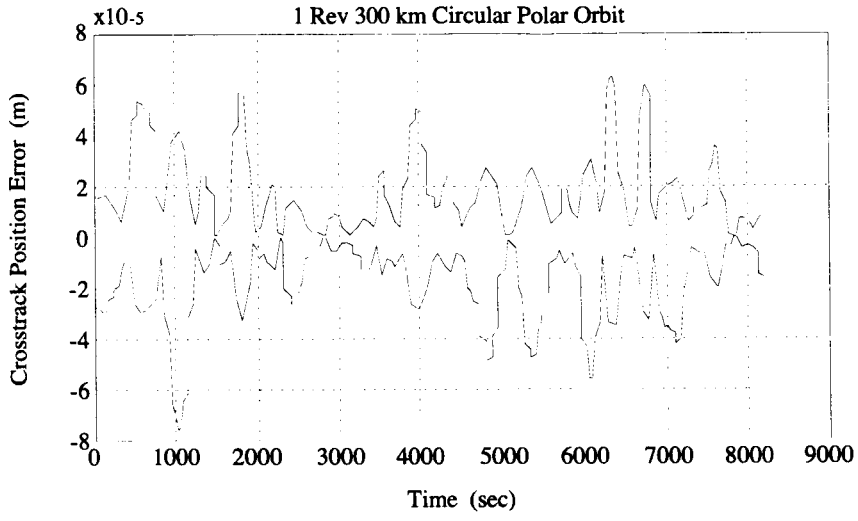
x10-5
1 Rev 300 km Circular Polar Orbit
Crosstrack Position Error (m)
8
6
4
2
0
-2
-4
-6
-8
0
1000
2000
3000
4000
5000
6000
7000
8000
9000
Time (sec)

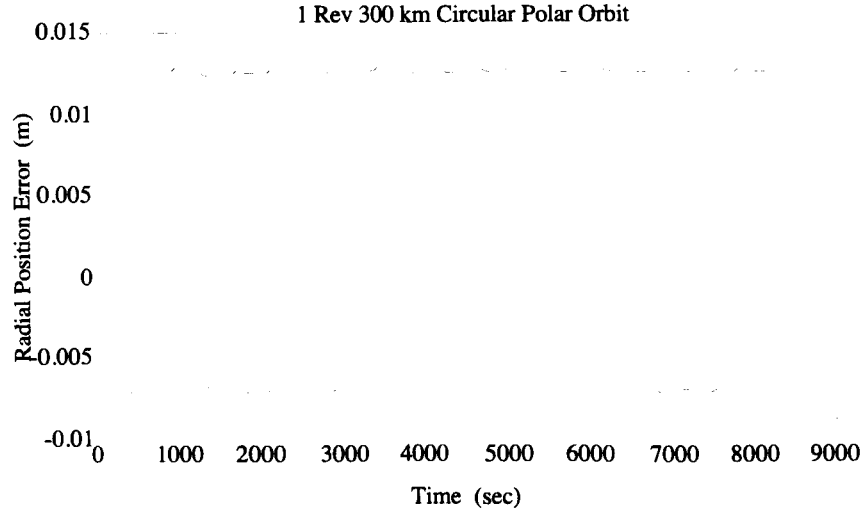
1 Rev 300 km Circular Polar Orbit
Radial Position Error (m)
0.015
0.01
0.005
0
-0.005
-0.01
0
1000
2000
3000
4000
5000
6000
7000
8000
9000
Time (sec)

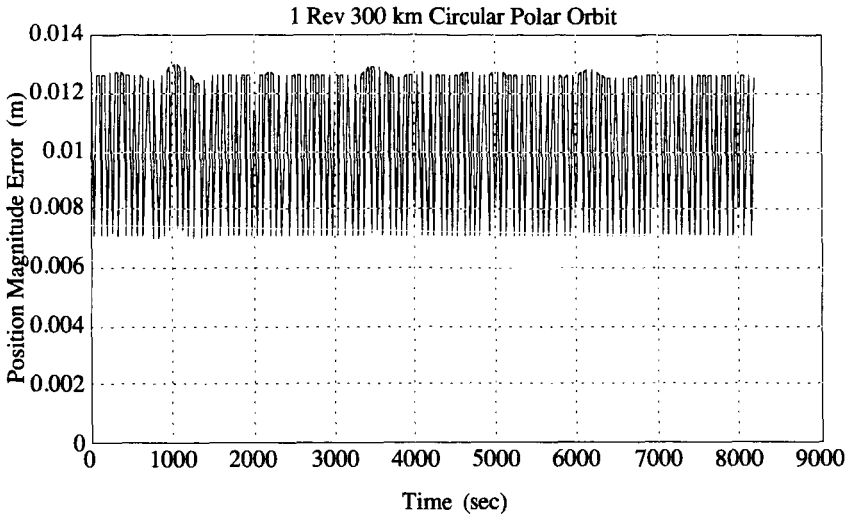

References

1. Barton, Gregg, "Gravity Task: Validation of Concept Using Simplified Orbit Trajectories on the German Photogrammetry Reconstruction when Generating Topographical Maps," CSDL memorandum ESB-93-249, April 7, 1993.

Appendix C

Appendix C - A General Analysis of the Effects of Both Deterministic and Stochastic Pointing Fluctuations on Imaging Performance

Author: Taylor W. Lawrence, Lawrence Livermore National Laboratory

Advanced Applications Program
Lawrence Livermore National Laboratory
An equal opportunity employer

A General Analysis of the Effects of Both Deterministic and Stochastic Pointing Fluctuations on Imaging Performance

With Application to the DLR High Resolution Stereo Camera In a Global Lunar Mapping Mission

Dr. Taylor W. Lawrence

Deputy Program Leader
Lawrence Livermore National Laboratory

and

Former Special Technical Assistant to the Lunar Scout Program Manager
Johnson Space Center

September 20, 1993

Contents

Page

Figures

2a	Amplitude as a function of temporal frequency for a single deterministic sinusioid	18
2b	Resulting OTF evaluated at the detector spatial frequency	18
3a	Angular standard deviation as a function of frequency bandwidth	20
3b	Resulting OTF evaluated at the detector spatial frequency	20
4a	Angular standard deviation as a function of frequency cut-off	20
4b	Resulting OTF evaluated at the detector spatial frequency	20
5	Examples of power spectral densities with different frequency bandwidths	22
6	OTF evaluated at the detector spatial frequency for a combined drift and jitter fluctuation	22
7	Examples of power spectral densities with different center frequencies	23
8	OTF evaluated at the detector spatial frequency for a combined drift and jitter fluctuation	24

Tables

1	HRSC camera and mission parameters for both a global and regional mapping base	14

1. Introduction

The effects of platform instabilities on imaging performance can be quite dramatic, ranging from imperceptible to devastating. As optical systems and detectors are designed for increasing capabilities in terms of resolution and pixel format, platform stability can become the limiting factor in achievable resolution. On spacecraft, this problem must be dealt with early on in the platform design, since modifications cannot be made once the platform is on station at some distant body, acquiring its first, possibly blurry, images. It is the purpose of this paper to present a summary of a very general analysis of the effects of pointing fluctuations and jitter on imaging performance, enabling the spacecraft designer to set requirements for stability that the platform must meet. I will present the basic governing equations and the results they lead to, leaving the details of the mathematical manipulations to the reader.

To show the utility of the analysis, the method is applied to the Lunar Scout mission in which the High Resolution Stereo Camera (HRSC), built by the German Aerospace Research Establishment (DLR) and the German Space Agency (DARA), was to fly in a lunar polar orbit to obtain a global stereo imagery database. The Lunar Scout mission encompassed a wide variety of other planetary science investigations, having been proposed in the NASA FY93 and FY94 budgets. A new start for the mission was not approved by Congress, however, as efforts to find savings to support the redesigned space station became a priority.

2. Background -- Optical Transfer Function and Pointing

For an incoherent imaging system, the starting point for specifying the imaging performance is the optical transfer function (OTF), $\mathrm{H}(\vec{u})$, which relates the Fourier transform of the object's intensity distribution to the Fourier transform of the image's intensity distribution [1],

$$\mathrm{I}_i(\vec{u}) = \mathrm{H}(\vec{u})\,\mathrm{I}_o(\vec{u}) \tag{2.1}$$

where $\vec{u}$ represents a spatial frequency vector and

$$\mathrm{I}_o(\vec{u}) = \frac{\int d^2\vec{x}\,\mathrm{I}_o(\vec{x})\,e^{-i2\pi\vec{u}\cdot\vec{x}}}{\int d^2\vec{x}\,\mathrm{I}_o(\vec{x})} \tag{2.2}$$

is the *normalized* Fourier transform of the object's intensity distribution, $\mathrm{I}_o(\vec{x})$, and

$$\mathrm{I}_i(\vec{u}) = \frac{\int d^2\vec{x}\,\mathrm{I}_i(\vec{x})\,e^{-i2\pi\vec{u}\cdot\vec{x}}}{\int d^2\vec{x}\,\mathrm{I}_i(\vec{x})} \tag{2.3}$$

is a similar expression for the image intensity distribution, $I_i(\bar{x})$. The OTF contains all of the information about the propagation path from the object to the imaging system as well as information about the imaging system itself. For the subject under consideration, namely pointing effects, we will consider a diffraction-limited imaging system in a vacuum. This is an excellent assumption for the specific case I will apply the analysis to, namely the Lunar Scout mission. Here the object intensity distribution arises from solar radiation that is scattered off of the lunar surface and propagates in a vacuum to the spacecraft and is imaged by the relatively aberration-free HRSC detector. For this case, the OTF becomes the normalized convolution of a generalized complex pupil function [1]:

$$H(\bar{u}) = \frac{\int d^2\bar{x}\, \mathbf{P}(\bar{x})\, \mathbf{P}^*(\bar{x} - \lambda z\bar{u})}{\int d^2\bar{x}\, |\mathbf{P}(\bar{x})|^2} \tag{2.4}$$

where λ is the center wavelength of the imaging system, z is the distance from the object to the imaging system, and

$$\mathbf{P}(\bar{x}) = e^{i\frac{2\pi}{\lambda}\bar{\theta}(t)\cdot\bar{x}}\, P(\bar{x}) \tag{2.5}$$

is the generalized pupil function which includes the effects of a time-dependent vectorial pointing function, $\bar{\theta}(t)$, measured in radians. $P(\bar{x})$ is the diffraction-limited pupil function, i.e., it is unity when the vector $\bar{x}$ lies inside the imaging system entrance pupil and zero otherwise. Because of the reciprocity theorem, and since we are considering imaging systems where the Fresnel approximation is valid, the pointing fluctuation has been treated as a linear phase shift in the entrance pupil.

To simplify the mathematical analysis, I will drop the vector notation and consider a one-dimensional problem. This is tantamount to considering an imaging system with a square aperture and evaluating the Fourier transform along one of the principle axes of the detector. For the HRSC case, the detector is already one-dimensional and so we will be considering jitter along the axis of the CCD lines (the most stressing case), which is spacecraft roll. Generalization to circular pupils and jitter in the other axes can be done by keeping the vector notation and carrying it through, but it does not effect the final results in any significant way.

Substituting (2.5) into (2.4), we obtain for the OTF in the presence of the pointing fluctuation, $\theta(t)$,

$$H(\xi) = e^{i\frac{2\pi D}{\lambda}\theta(t)\xi}\, \Lambda(\xi) \tag{2.6}$$

where ξ is a spatial frequency variable that is normalized to unity at the diffraction-limited spatial frequency of the imaging system with effective diameter D, i.e.,

$$\xi = \frac{\lambda z}{D} u \tag{2.7}$$

and

$$\Lambda(\xi) = \begin{cases} 1 - |\xi| & |\xi| \le 1 \\ 0 & \text{otherwise} \end{cases} \tag{2.8}$$

is the diffraction-limited OTF for the imaging system. Since we are primarily concerned with the influences of the pointing term on the imaging performance at spatial frequencies less than the diffraction limit, I will divide out $\Lambda(\xi)$, defining

$$H_\theta(\xi) = \frac{H(\xi)}{\Lambda(\xi)} = e^{i\frac{2\pi D}{\lambda}\theta(t)\xi} \tag{2.9}$$

We see that the pointing fluctuation modifies the OTF by the introduction of a time-dependent linear phase term which is normalized by the diffraction-limited angle, λ/D, of the imaging system.

The final concept we have to introduce is that of the time average OTF. Since the imaging system integrates for some time τ, the effects of the pointing fluctuation are averaged over this time

$$\langle H_\theta(\xi) \rangle = \frac{1}{\tau} \int_{-\frac{\tau}{2}}^{+\frac{\tau}{2}} dt\, H_\theta(\xi) \tag{2.10}$$

$$= \frac{1}{\tau} \int_{-\frac{\tau}{2}}^{+\frac{\tau}{2}} dt\, e^{i\frac{2\pi D}{\lambda}\theta(t)\xi}$$

In order to proceed any further, we must specify the form of the time-dependence of the pointing fluctuation. First, I will consider a known deterministic function in which the OTF can be evaluated directly. Then I will examine the case of a random pointing fluctuation in which $\theta(t)$ is considered to be a random process specified by its moments and its time autocorrelation function. Finally, I will treat the combined case of a slowly varying deterministic fluctuation (a linear drift, for example) coupled with a high frequency random component (jitter).

3. Deterministic Oscillations

Let us consider a deterministic sinusoidal oscillation, caused possibly by the platform rocking back and forth at a known rate as the attitude control system maintains nominal pointing within some dead band,

$$\theta(t) \;=\; \theta_0 \sin 2\pi\nu t \tag{3.1}$$

where θ_0 is the amplitude of the motion at frequency ν. Plugging this into (2.10), we obtain, for the time-averaged OTF

$$\left\langle \mathrm{H}_{\theta}(\xi) \right\rangle \;=\; \frac{1}{\tau} \int_{-\frac{\tau}{2}}^{+\frac{\tau}{2}} dt\, e^{i\frac{2\pi D}{\lambda}\theta_0 \xi \sin(2\pi\nu t)} \tag{3.2}$$

To evaluate this integral, we need the Bessel function expansion [2]

$$\begin{aligned} e^{i\frac{2\pi D}{\lambda}\theta_0 \xi \sin(2\pi\nu t)} \;=\; & \mathrm{J}_0\!\left(\frac{2\pi D}{\lambda}\theta_0 \xi\right) \;+\; 2\sum_{k=1}^{\infty} \mathrm{J}_{2k}\!\left(\frac{2\pi D}{\lambda}\theta_0 \xi\right) \cos(4\pi k\nu t) \\ & +\; 2i\sum_{k=0}^{\infty} \mathrm{J}_{2k+1}\!\left(\frac{2\pi D}{\lambda}\theta_0 \xi\right) \sin\!\left(2\pi(2k+1)\nu t\right) \end{aligned} \tag{3.3}$$

which results in

$$\left\langle \mathrm{H}_{\theta}(\xi) \right\rangle \;=\; \mathrm{J}_0\!\left(\frac{2\pi D}{\lambda}\theta_0 \xi\right) \;+\; 2\sum_{k=1}^{\infty} \frac{\sin(2\pi k\nu\tau)}{2\pi k\nu\tau}\, \mathrm{J}_{2k}\!\left(\frac{2\pi D}{\lambda}\theta_0 \xi\right) \tag{3.4}$$

Thus, we are able to obtain a closed-form solution for the time-averaged OTF in the presence of a sinusoidal pointing oscillation. Details of this expression will be investigated when I apply the result to the case of the HRSC. However, two limiting cases are worth mentioning at this point: $\nu\tau << 1$ and $\nu\tau >> 1$.

For $\nu\tau << 1$, the sinusoid (3.1) reduces to a linear phase term (a slow "drift"), and we can go back and linearize the original integral (3.2) to obtain

$$\left\langle \mathrm{H}_{\theta}(\xi) \right\rangle \;\underset{\nu\tau << 1}{\approx}\; \frac{\sin\!\left(\pi \frac{2\pi D}{\lambda}\theta_0 \xi \nu\tau\right)}{\pi \frac{2\pi D}{\lambda}\theta_0 \xi \nu\tau} \tag{3.5}$$

The equivalent linear drift is $2\pi\theta_0\nu$ radians per second.

For $\nu\tau >> 1$, the effects of the sinusoid are averaged over many times, and the pre-factor in the infinite Bessel sum becomes vanishingly small for all values of the index, leaving only the frequency-independent term

$$\left\langle \mathrm{H}_{\theta}(\xi) \right\rangle \underset{\nu\tau >> 1}{\approx} \mathrm{J}_0\left(\frac{2\pi D}{\lambda}\theta_0 \xi\right) \tag{3.6}$$

So that the overall amplitude of the oscillation is the key factor and the drift frequency plays no role.

4. Statistical Analysis -- The Relationship Between the OTF and the Power Spectral Density

To analyze statistical properties, we in general have to compute expectations of moments of the random process in question, in this case the random process $\theta(t)$. Using all of the normal assumptions about "well-behaved" physical processes, i.e., ergodicity, wide-sense stationarity, etc. [3], we can set about computing the optical performance of the system. To assure a non-zero characterization of the OTF, we have to compute a root-mean-square equivalent, so we begin the analysis by forming the power spectrum of the time-averaged OTF

$$\left|\left\langle \mathrm{H}_{\theta}(\xi) \right\rangle\right|^2 = \frac{1}{\tau^2}\int_{-\frac{\tau}{2}}^{+\frac{\tau}{2}}\int dt\, dt' \exp\left[i\,\frac{2\pi D}{\lambda}\left(\theta(t)-\theta(t')\right)\xi\right] \tag{4.1}$$

To compute the expectation value of the power spectrum over the random *ensemble*, we invoke ergodicity and take the *time* expectation value

$$\overline{\left|\left\langle \mathrm{H}_{\theta}(\xi) \right\rangle\right|^2} = \frac{1}{\tau^2}\int_{-\frac{\tau}{2}}^{+\frac{\tau}{2}}\int dt\, dt' \overline{\exp\left[i\,\frac{2\pi D}{\lambda}\left(\theta(t)-\theta(t')\right)\xi\right]} \tag{4.2}$$

which is denoted by the overbar. In statistical theory, the time expectation value of the complex exponential is given a special name: the characteristic function [4]

$$\overline{\exp\left[i\,\frac{2\pi D}{\lambda}\left(\theta(t)-\theta(t')\right)\xi\right]} = \mathbf{M}_{\Delta\theta}\left(\frac{2\pi D}{\lambda}\xi\right) \tag{4.3}$$

and there are lots of statistical tools for relating the characteristic function to structure functions and power spectral density, etc., as we shall shortly see. Substituting (4.3) into (4.2) we have the reasonably straightforward result

$$\overline{\left|\langle \mathrm{H}_{\theta}(\xi)\rangle\right|^2} = \frac{1}{\tau^2}\int_{-\frac{\tau}{2}}^{+\frac{\tau}{2}}\int dt\,dt'\,\mathbf{M}_{\Delta\theta}\left(\frac{2\pi D}{\lambda}\xi\right) \tag{4.4}$$

Now we must make some assumptions about the statistics of the random process $\theta(t)$. The simplest assumption, and usually most physically correct, is that $\theta(t)$ is a zero-mean Gaussian random process characterized by the following moments

$$\begin{aligned}\overline{\theta(t)} &= 0\\ \overline{\theta^2(t)} &= \sigma_\theta^2\end{aligned} \tag{4.5}$$

This assumption also implies that $\theta(t) - \theta(t')$ is a zero-mean Gaussian random process and that

$$\begin{aligned}\overline{\theta(t) - \theta(t')} &= 0\\ \overline{\left(\theta(t) - \theta(t')\right)^2} &= \mathbf{D}_\theta(t,t')\end{aligned} \tag{4.6}$$

where $\mathbf{D}_\theta(t,t')$ is the structure function of the random process. Again invoking statistical theory, the characteristic function of a Gaussian random process is related to the structure function in the following manner [5]

$$\mathbf{M}_{\Delta\theta}(\omega) = \exp\left[-\frac{1}{2}\,\omega^2\,\mathbf{D}_\theta(t,t')\right] \tag{4.7}$$

In addition, if the random process is at least stationary in first increments, the structure function is "shift-invariant" [6], meaning

$$\mathbf{D}_\theta(t,t') = \mathbf{D}_\theta(t-t') \tag{4.8}$$

We are in the home stretch now. We can substitute (4.7) into (4.4) and use (4.8) to perform one of the integrations and simplify the expression for the expected power spectrum to

$$\overline{\left|\langle \mathrm{H}_{\theta}(\xi)\rangle\right|^2} = 2\int_0^1 d\eta\,(1-\eta)\exp\left[-\frac{1}{2}\left(\frac{2\pi D}{\lambda}\xi\right)^2\mathbf{D}_\theta(\tau\eta)\right] \tag{4.9}$$

Remembering that our ultimate objective is to relate the optical transfer function (which is the square root of the expected power spectrum) to the power spectral density of the pointing fluctuations, we need the relationship between the structure function for the random process, $\mathbf{D}_\theta(\tau\eta)$, and the power spectral density of the random process, $\mathrm{G}_\theta(\nu)$, given by

$$\mathbf{D}_\theta(\tau\eta) = 2\int_{-\infty}^{+\infty} d\nu \left(1 - \cos[2\pi\nu\tau\eta]\right) \mathrm{G}_\theta(\nu) \tag{4.10}$$

which is a consequence of the Wiener-Khinchin theorem [6]. The power spectral density specifies the frequency content of the pointing fluctuation and must be symmetric in ν to preserve causality and is subject to the normalization

$$\int_{-\infty}^{+\infty} d\nu \, \mathrm{G}_\theta(\nu) = \overline{\theta^2(t)} = \sigma_\theta^2 \tag{4.11}$$

We now have all of the tools to compute the root-mean-square expected value of the OTF in the presence of the stochastic pointing fluctuation $\theta(t)$. Before proceeding to our particular application, I will consider the form that the OTF takes for two common power spectral densities: Gaussian and white noise.

4.1 Gaussian Power Spectral Density

Assume that the Gaussian random process, $\theta(t)$, also has a zero-mean Gaussian power spectral density with width σ_ν given by

$$\mathrm{G}_\theta(\nu) = \frac{\sigma_\theta^2}{\sqrt{2\pi}\,\sigma_\nu} \exp\left[-\frac{\nu^2}{2\sigma_\nu^2}\right] \tag{4.12}$$

Plugging into (4.10), we obtain for the structure function

$$\mathbf{D}_\theta(\tau\eta) = 2\sigma_\theta^2 \left(1 - \exp\left[-\frac{1}{2}\left(2\pi\sigma_\nu\tau\eta\right)^2\right]\right) \tag{4.13}$$

which ultimately results in the following OTF (and I will now introduce a hat over the OTF to stand for the combined operations $\sqrt{\overline{|\langle\ \rangle|^2}}$)

$$\begin{aligned} \hat{H}_\theta(\xi) &\equiv \sqrt{\overline{\left|\langle H_\theta(\xi)\rangle\right|^2}} \\ &= \sqrt{2\int_0^1 d\eta\,(1-\eta)\exp\left[-\alpha^2\xi^2\left(1-\exp\left[-\frac{1}{2}\beta^2\eta^2\right]\right)\right]} \end{aligned} \tag{4.14}$$

The two key dimensionless parameters appearing in the above expression are given by

$$\alpha = \frac{2\pi D}{\lambda}\sigma_\theta \qquad \beta = 2\pi\sigma_v\tau \tag{4.15}$$

The integral in (4.14) in general must be computed numerically, but a couple of limits will be useful in the later sections, namely, when $\beta << 1$, i.e., $\sigma_v << \frac{1}{2\pi\tau}$, we have

$$\hat{H}_\theta(\xi) \underset{\beta << 1}{\approx} \sqrt{2\left\{\sqrt{\frac{\pi}{2(\alpha\beta\xi)^2}}\,\mathrm{Erf}\left[\frac{\alpha\beta\xi}{\sqrt{2}}\right] - \frac{1}{(\alpha\beta\xi)^2}\left(1-\exp\left[-\frac{1}{2}(\alpha\beta\xi)^2\right]\right)\right\}} \tag{4.16}$$

where $\mathrm{Erf}[x]$ is the error function.

In the opposite limit, when $\beta >> 1$, i.e., $\sigma_v >> \frac{1}{2\pi\tau}$, we have

$$\hat{H}_\theta(\xi) \underset{\beta >> 1}{\approx} \exp\left[-\frac{1}{2}\alpha^2\xi^2\right] \tag{4.17}$$

Just as in the deterministic case, when the frequency structure is significantly higher than the exposure time, the details of the frequency dependence drop out, and in this case the only remaining important parameter is the standard deviation of the pointing fluctuation, σ_θ, analogous to the sinusoidal amplitude in the deterministic case (compare with (3.6)).

4.2 White Noise Power Spectral Density

This section is basically a repeat of the last section but now let us assume that the Gaussian random process, $\theta(t)$, instead has a white noise power spectral density which is constant at all frequencies up to some natural cut-off frequency, ν_{max}, i.e.

$$G_\theta(\nu) = \begin{cases} \dfrac{\sigma_\theta^2}{2\nu_{max}} & |\nu| < \nu_{max} \\ 0 & \text{otherwise} \end{cases} \tag{4.18}$$

Again plugging into (4.10), we obtain for the structure function

$$D_\theta(\tau\eta) = 2\sigma_\theta^2\left(1 - \frac{\sin[2\pi\nu_{max}\tau\eta]}{2\pi\nu_{max}\tau\eta}\right) \tag{4.19}$$

which results in the OTF

$$H^{\sqrt{}}_\theta(\xi) = \sqrt{2\int_0^1 d\eta\,(1-\eta)\exp\left[-\alpha^2\xi^2\left(1 - \frac{\sin[\beta\eta]}{\beta\eta}\right)\right]} \tag{4.20}$$

The dimensionless parameter, α, is the same as in (4.15) and β is analogous, i.e.,

$$\alpha = \frac{2\pi D}{\lambda}\sigma_\theta \qquad \beta = 2\pi\nu_{max}\tau \tag{4.21}$$

As before, the integral in (4.20) must be computed numerically. However, the limits are straightforward to compute. When $\beta << 1$, i.e., $\nu_{max} << \frac{1}{2\pi\tau}$, we have

$$H^{\sqrt{}}_\theta(\xi) \underset{\beta << 1}{\approx} \sqrt{2\left\{\sqrt{\frac{3\pi}{2(\alpha\beta\xi)^2}}\,\mathrm{Erf}\left[\frac{\alpha\beta\xi}{\sqrt{6}}\right] - \frac{3}{(\alpha\beta\xi)^2}\left(1 - \exp\left[-\frac{1}{6}(\alpha\beta\xi)^2\right]\right)\right\}} \tag{4.22}$$

which is identical to (4.16), but with the substitution $\beta \rightarrow \frac{\beta}{\sqrt{3}}$.

In the opposite limit, when $\beta >> 1$, i.e., $\nu_{max} >> \frac{1}{2\pi\tau}$, we have a result identical to (4.17)

$$H^{\sqrt{}}_\theta(\xi) \underset{\beta >> 1}{\approx} \exp\left[-\frac{1}{2}\alpha^2\xi^2\right] \tag{4.23}$$

5. Coupled Analysis -- Drift and Jitter

The last part of the theoretical analysis that needs to be completed before proceeding to the application is to combine the results of the previous two sections so that we have a completely general coupled analysis. As we shall see, however, some simplifying assumptions have to be made in order to reach a tractable solution. The assumptions are consistent with the most likely condition when a coupled analysis would be necessary, i.e., when we have a slow sinusoid (drift) with a high frequency random component added in (jitter).

In the coupled analysis, the pointing fluctuation function takes the form

$$\theta(t) \;=\; \theta_0 \sin\left[2\pi\nu_0 t\right] \;+\; \phi(t) \qquad (5.1)$$

where θ_0 is the amplitude of the deterministic sinusoid at frequency ν_0, and now $\phi(t)$ is the random variable from a zero-mean Gaussian process (with standard deviation σ_ϕ) and a power spectral density that will be specified. Plugging into the equation for the expected power spectrum, we have

$$\overline{\left|\left\langle \mathrm{H}_\theta(\xi)\right\rangle\right|^2} \;=\; \frac{1}{\tau^2}\int_{-\frac{\tau}{2}}^{+\frac{\tau}{2}}\!\!\int dt\,dt'\,\exp\left[i\frac{2\pi D}{\lambda}\theta_0\left(\sin 2\pi\nu_o t - \sin 2\pi\nu_o t'\right)\xi\right]\,\mathbf{M}_{\Delta\phi}\left(\frac{2\pi D}{\lambda}\xi\right) \qquad (5.2)$$

where the characteristic function refers to the random variable $\Delta\phi \;=\; \phi(t) - \phi(t')$. To proceed further, we need to make the simplification, as noted earlier, that the deterministic sinusoid is slowly varying, i.e.,

$$\nu_0\tau \;<<\; 1 \qquad (5.3)$$

We can then linearize the exponential and obtain a shift invariant kernel, i.e., one that is only a function of the difference $(t \;-\; t')$. This is tantamount to considering a linear drift coupled with the random fluctuation. In this manner, we can put in the expression for the structure function and perform one of the integrations to obtain

$$\overline{\left|\left\langle \mathrm{H}_\theta(\xi)\right\rangle\right|^2} \;=\; 2\int_0^1 d\eta\,(1-\eta)\cos\left[\frac{2\pi D}{\lambda}\theta_0\xi\cdot 2\pi\nu_0\tau\eta\right]\exp\left[-\frac{1}{2}\left(\frac{2\pi D}{\lambda}\xi\right)^2\,\mathbf{D}_\phi(\tau\eta)\right] \qquad (5.4)$$

Now we must make some assumptions about the statistics of the random process $\phi(t)$. Since I have included a low frequency component already (the drift term), the power spectral density of the random component will in general *not* be zero mean, but rather centered at some frequency, ν_m, and have some characteristic bandwidth, σ_ν.

Remembering that the power spectral density must be symmetric to preserve causality, we have

$$G_\theta(\nu) = \frac{\sigma_\theta^2}{\sqrt{8\pi}\,\sigma_\nu}\left\{\exp\left[-\frac{(\nu-\nu_m)^2}{2\sigma_\nu^2}\right] + \exp\left[-\frac{(\nu+\nu_m)^2}{2\sigma_\nu^2}\right]\right\} \tag{5.5}$$

which leads to the following structure function

$$D_\theta(\tau\eta) = 2\sigma_\theta^2\left(1 - \cos\left[2\pi\nu_m\tau\eta\right]\exp\left[-\frac{1}{2}(2\pi\sigma_\nu\tau\eta)^2\right]\right) \tag{5.6}$$

Plugging this into (5.4) ultimately leads to

$$H_\theta(\xi) = \sqrt{2\int_0^1 d\eta\,(1-\eta)\cos\left[2\pi\zeta\xi\eta\right]\exp\left[-\alpha^2\xi^2\left(1-\cos\left[\gamma\eta\right]\exp\left[-\frac{1}{2}\beta^2\eta^2\right]\right)\right]} \tag{5.7}$$

where we have the dimensionless parameters associated with the jitter

$$\alpha = \frac{2\pi D}{\lambda}\sigma_\theta \qquad \beta = 2\pi\sigma_\nu\tau \qquad \gamma = 2\pi\nu_m\tau \tag{5.8}$$

and the dimensionless parameter associated with the drift

$$\zeta = \frac{2\pi D}{\lambda}\theta_0\nu_0\tau \tag{5.9}$$

To close out this section, I show in Figure 1 an example of the various kinds of pointing fluctuations considered in this analysis. The plot is a simulation of what a star tracker might record, i.e., pointing angle, $\theta(t)$, as a function of time. Figure 1a shows a deterministic sinusoid with an amplitude of 7.07 μrad and a frequency of 5 Hz (for comparison with the statistical signals, the standard deviation of this signal is 5 μrad). Figures 1b-d show samples from a zero-mean Gaussian pointing fluctuation with a standard deviation, σ_θ, of 5 μrad and: (b) a zero-mean Gaussian power spectral density with a width, σ_ν, of 5 Hz; (c) a zero-mean Gaussian power spectral density with a width, σ_ν, of 55 Hz; and (d) a white noise power spectral density with a cut-off frequency, ν_{max}, of 256 Hz. Figure 1e shows a combined pointing fluctuation with a drift component, $2\pi\theta_0\nu_0$, of 10 μrad/s, and a stochastic jitter component with a standard deviation, σ_θ, of 5 μrad, a center frequency, ν_m, of 55 Hz and a width, σ_ν, of 13.75 Hz.

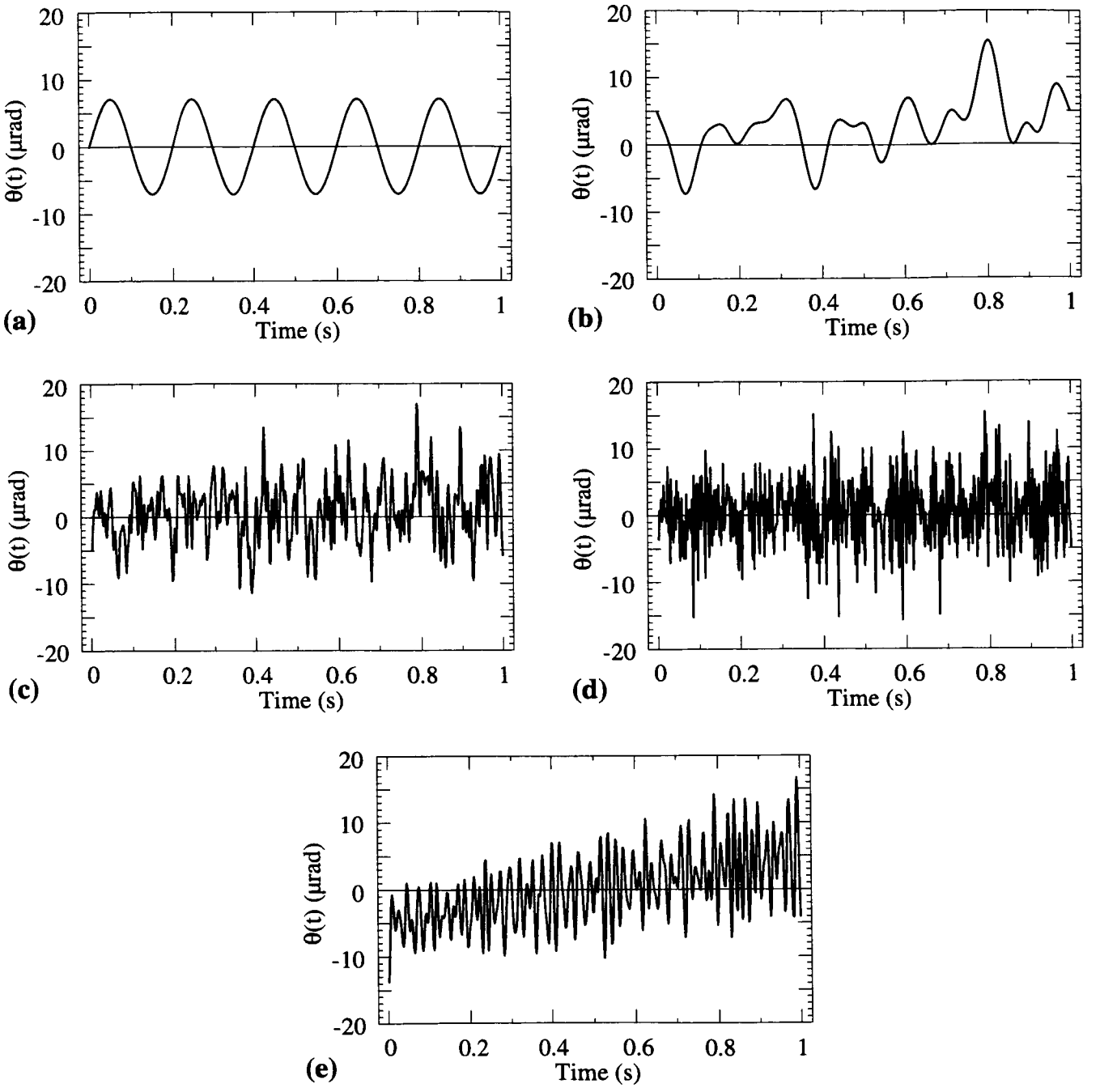

Figure 1. Examples of the various kinds of pointing fluctuations considered in this analysis. Each plot shows the pointing angle, $\theta(t)$, as a function of time.
(a) $\theta_0 = 7.07$ μrad, $\nu = 5$ Hz (b) $\sigma_\theta = 5$ μrad, $\sigma_\nu = 5$ Hz
(c) $\sigma_\theta = 5$ μrad, $\sigma_\nu = 55$ Hz (d) $\sigma_\theta = 5$ μrad, $\nu_{max} = 256$ Hz
(e) $2\pi\theta_0\nu_0 = 10$ μrad/s, $\sigma_\theta = 5$ μrad, $\nu_m = 55$ Hz, $\sigma_\nu = 13.75$ Hz

6. Application to the High Resolution Stereo Camera in Lunar Orbit

We are now ready to apply the formalism derived in the previous sections to a particular case study and make some quantitative conclusions. The present application is that of a mapping camera in orbit around the Moon. This work was performed in order to derive detailed spacecraft performance specifications for an open competition process. Because the program was terminated by Congress, the spacecraft procurement process was never completed. However, the analysis can serve as a template for future high resolution mapping missions. To set the analysis in context, I will briefly review the (now defunct) Lunar Scout mission and the role of the mapping camera in it.

6.1 The Lunar Scout I Mission

The Lunar Scout I spacecraft and its instrument suite were envisioned to provide fundamental imagery and elemental mapping of the lunar surface and facilitate mapping of the lunar gravity field [7]. Lunar Scout I was to be placed initially in a 300 km orbit for one month of global mapping. The High Resolution Stereo Camera, described shortly, would have acquired global stereo imagery at 24 meters per pixel, and x-ray and neutron spectrometers would have begun global elemental mapping. Gravity data corresponding to the front side would have been taken by using two-way Doppler tracking of the spacecraft from Deep Space Network ground stations. After the global mapping phase, the spacecraft would have descended to a 100 km orbit for higher resolution regional stereo imagery. The x-ray and neutron spectrometers would have continued acquisition of global data. At the end of Lunar Scout I's one year mapping phase, a second similar spacecraft, Lunar Scout II, was to be established in an initial elliptical orbit, and the Lunar Scout I spacecraft would have served as a passive gravity field sensor with Lunar Scout II acting as a relay, producing a global high resolution gravity field data set.

6.2 The High Resolution Stereo Camera

The German Space Agency (DARA), the German Aerospace Research Establishment (DLR) and NASA had discussed the possibility of including on Lunar Scout I a copy of the High Resolution Stereo Camera (HRSC) built by DLR for the Russian Mars '94 and '96 missions.

The HRSC is an imaging system of the push-broom line-scanner type [8]. The main optical parameters associated with the system are summarized in Table 1. The HRSC consists of a camera unit and a solid-state mass memory unit with 1 Gbit of memory and onboard compression. It is a new development in planetary imaging because it has a multi-line configuration consisting of an objective lens and three focal plate sensor arrays as opposed to two. The focal plate arrays each have 3 CCD lines of 5184 pixels for a total of nine line sensors. One array is forward looking with a panchromatic stereo, a selectable color, and a photometry channel; one is nadir looking with a panchromatic channel and two selectable color channels; and one is aft looking with a panchromatic stereo, a selectable color and a photometry channel. The system can incorporate up to nine bandpass filters with a wavelength range from 395 to 1015nm (Table 1 shows the center wavelength of the panchromatic nadir channel). The combination of a nadir array with

HRSC Parameters		
Entrance Pupil	3.125 cm	
Focal Length (f#)	175 mm (f / 5.6)	
Nadir Center Wavelength	675 nm	
Stereo Separation	18.9°	
Pixel Size (IFOV)	7 μm (40 μrad)	
Mission Parameters		
	Global Mapping	Regional Mapping
Orbital Altitude	300 km	100 km
Nadir / Stereo Resolution	24 m / 25.6 m	4 m / 4.24 m
Swath Length	4551 km	172 km
Swath Width	42.4 km	20.7 km
Stereo Base Length	104 km	34 km
Data Compression	10:1	6:1
Data per orbit	0.74 Gbit	0.82 Gbit
Data rate	558 kbps	7.4 Mbps
Months of Mapping	1	8.3
Total Compressed Data	26 Gbytes	348 Gbytes
Surface Coverage	100 %	26 %

Table 1. HRSC camera and mission parameters for both a global and regional mapping phase

fore and aft stereo arrays provides much of the fidelity for geodesy that is provided by framing cameras through use of the techniques of three-axis photogrammetry [9].

The HRSC was intended to produce data for compilation of a global geodetic net early in the Lunar Scout I mission. Parameters for both the global mapping phase and the lower altitude regional mapping phase are shown in Table 1. The selections for the global phase were based on the requirement to obtain global data as early as possible (in one month) while meeting data storage (1 Gbit) and downlink (1 Mbps) constraints [7]. For the regional mapping phase at an altitude of 100 km, 26% of the lunar surface could have been covered over the course of the mission while again maintaining the same storage and downlink constraints.

A forerunner of the HRSC was flown on the Space Shuttle (STS-55) in April, 1993 (the MOMS-02/D2 experiment) [10]. The software that was used for this experiment is directly applicable to the lunar case, and preliminary results using these tools indicate that for the global mapping parameters listed in Table 1, and with spacecraft position measurement accuracy of 10 m and attitude measurement accuracy of 0.01°, latitude and longitude accuracy of 10 m could have been achieved with an elevation accuracy of 23m[11]. The possibility of this incredible new level of fidelity in geodetic precision places strict

requirements on the spacecraft in terms of pointing and jitter fluctuations. These requirements are computed in the next section.

6.3 Pointing and Jitter Requirements

I will follow the analysis of Sections 3-5 and compute requirements for each of the three scenarios: deterministic, stochastic, and a combination. First we must specify the allowed degradation to the OTF that is induced by the pointing fluctuations. From a system engineering standpoint, this is but one term in an error budget for the overall optical system which would include aberrations, throughput, etc. For this analysis, I will assume a 10% reduction is budgeted for the pointing terms. Thus

$$\left\langle H_{\theta}(\xi_d) \right\rangle \approx 0.9 \tag{6.1}$$

where the OTF is evaluated at the spatial frequency, ξ_d, of the detector.

For the HRSC mapping mission, using the parameters in Table 1, the diffraction-limited angle of the imaging system is given by

$$\frac{\lambda}{D} = 21.6 \ \mu\text{rad} \tag{6.2}$$

and the normalized spatial frequency, given by (2.7), of the detector is

$$\begin{aligned} \xi_d &= \frac{\lambda z}{D} u_d \\ &= \frac{\left(0.675\ 10^{-6}\right)\left(300\ 10^{3}\right)}{0.03125} \frac{1}{24} \\ &= 0.27 \end{aligned} \tag{6.3}$$

where we have used the fact that the spatial frequency of the detector (referred to the image plane) is the inverse of the resolution of the system (24 m in this case). Notice that the *achievable* resolution of the system, given a pixel IFOV of 40 μrad (see Table 1) is actually 12 m. However, due to data storage constraints, the pixels are summed, or binned, by two (by lengthening the integration time in the scan direction and electronically summing in the cross-track direction). This gives an effective decrease in resolution and results in a macro-pixel IFOV of 80 μrad (note: 21.6 μrad / 80 μrad = 0.27).

The integration time is equivalent to the inverse of the line scan read-out frequency, ν_{read}, of the push-broom camera and is a function of the orbital altitude of the platform and whether there is any pixel binning. For a spherical moon, the orbital angular velocity of the spacecraft is given by

$$\begin{aligned} \omega &= \sqrt{\frac{GM_m}{R_m^3}} \left(1 + \frac{z}{R_m}\right)^{-\frac{3}{2}} \quad \frac{\text{rad}}{\text{s}} \\ &= 0.967 \left(1 + \frac{z}{R_m}\right)^{-\frac{3}{2}} \quad \frac{\text{mrad}}{\text{s}} \end{aligned} \tag{6.4}$$

where G is the universal gravitational constant, M_m is the lunar mass (7.354 x 10^{22} kg) and R_m is the lunar radius (1.738 x 10^6 m). To obtain the read-out frequency, we multiply by the angular frequency of a macro-pixel, $u_d R_m$ (the inverse of the angular size of the macro-pixel),

$$\begin{aligned} \nu_{\text{read}} &= \omega u_d R_m \\ &= \omega \frac{\xi_d}{\lambda/D} \frac{R_m}{z} \\ &= \frac{9670\ \xi_d}{\frac{\lambda}{D} \frac{z}{R_m} \left(1 + \frac{z}{R_m}\right)^{3/2}} \quad \text{Hz} \end{aligned} \tag{6.5}$$

and in the last line λ/D is measured in μrad. For the global mapping orbit of z = 300 km and using the parameters in (6.2) and (6.3), we have

$$\begin{aligned} \nu_{\text{read}} &= 55 \text{ Hz} \\ \tau &= \frac{1}{\nu_{\text{read}}} = 0.0181 \text{ s} \end{aligned} \tag{6.6}$$

6.3.1 Deterministic Oscillations

Before using the full expression of (3.4), let us examine the limits given by (3.5) and (3.6) to derive the allowed amplitude as a function of frequency for these two extremes. For the case $\nu\tau << 1$, we can make use of the numerical relation

$$\frac{\sin[\pi(0.25041)]}{\pi(0.25041)} = 0.9 \tag{6.7}$$

and (3.5) to obtain

$$\frac{2\pi D}{\lambda} \theta_0 \xi_d \nu\tau = 0.25041 \tag{6.8}$$

which basically states that in this regime, the total angular drift during the integration time can be no more than about one-quarter pixel, consistent with the typical "rule-of-thumb." Converting this to an equivalent drift rate, using the parameters in (6.2) through (6.6), we have

$$2\pi\theta_0\nu = \frac{0.25041}{\tau}\frac{\lambda}{\xi_d D} \tag{6.9}$$
$$= 1.106\ \frac{\text{mrad}}{\text{s}} = 0.0634\ \frac{^\circ}{\text{s}}$$

Obviously θ_0 cannot increase without bound as $\nu \rightarrow 0$, because there is a fundamental constraint that the spacecraft point within some angular distance of nadir to insure complete coverage of the lunar surface from orbit to orbit and maintain at least some minimum overlap. Using the geometry of the orbit and the swath parameters in Table 1, this maximum deviation angle was computed to be [7]

$$\theta_{max} = 0.368^\circ = 6430\ \mu\text{rad} \tag{6.10}$$

which occurs at a temporal frequency of $\nu = 0.0275$ Hz in (6.9).

In the opposite extreme, $\nu\tau >> 1$, we use (3.6) and the numerical relation

$$J_0\left[2\pi(0.10196)\right] = 0.9 \tag{6.11}$$

to obtain

$$\theta_0 = 0.10196\ \frac{\lambda}{\xi_d D} \tag{6.12}$$
$$= 8.157\ \mu\text{rad}$$

which says that all high frequency amplitudes must be less than about one-tenth of a pixel.
The transition behavior from low to high frequency is more difficult to treat because we have to return to the full expansion in (3.4). To make life easier, I will simply patch together the two expressions, (6.9) and (6.12), with the cut-off in (6.10), to form a complete functional form for θ_0. This is plotted in Figure 2a. The cross-over in behaviors occurs at $\nu = 21.67$ Hz, when θ_0 as given by (6.9) equals 8.157 μrad. Figure 2b shows the result of plugging the values of θ_0 given by the curve in Figure 2a into the full expression for $\langle H_\theta(\xi)\rangle$. We see that the OTF converges to 0.9 in both limits and includes some Bessel function oscillations. Although I have not strictly enforced the constraint that the OTF due to the pointing be equal to 0.9, the oscillations are not large, and we have instead a simple, monotonic, form for the

maximum allowed amplitude. For setting spacecraft requirements, a simple monotonic function is highly desirable.

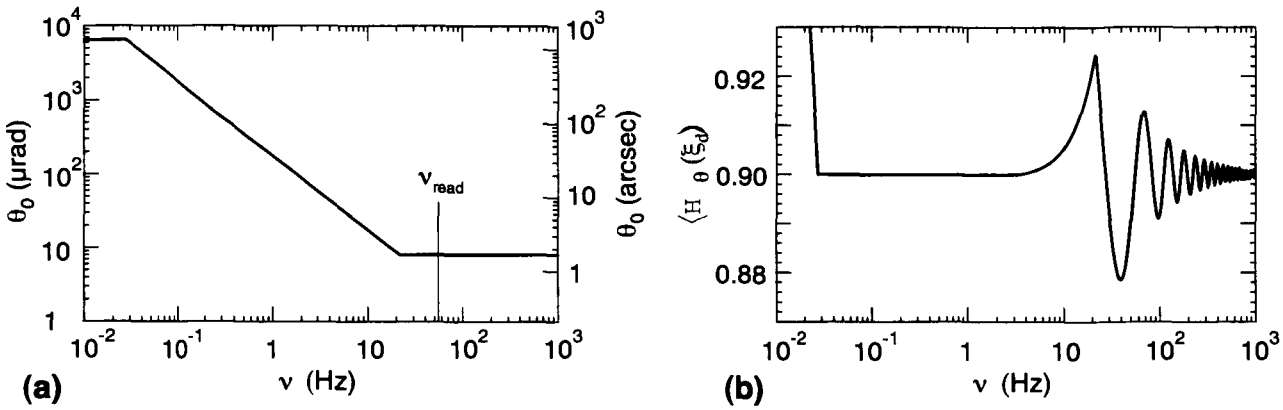

Figure 2. (a) Amplitude as a function of temporal frequency for a single deterministic sinusoid using the expressions in (6.9), (6.10), and (6.11).
(b) Resulting OTF evaluated at the detector spatial frequency.

6.3.2 Stochastic Fluctuations

Let us follow a similar treatment for the statistical pointing fluctuations, using the results of Section 4 for the two specific cases of Gaussian and white noise power spectral densities. In each case, I will use the two limits to construct a functional form for the allowed values of angular standard deviation as a function of: frequency bandwidth, in the Gaussian case; and cut-off frequency, in the white noise case (both are analogous to amplitude versus frequency). I will then plug these functions into the full expression for the OTF and compute the numerical integration to make sure any excursions are within acceptable limits.

Since the limits in Sections 4.1 and 4.2 are identical when one makes the identification: $\sigma_\nu \leftrightarrow \nu_{max}/\sqrt{3}$, I only need to produce a single functional form for σ_θ. In the regime where $\beta << 1$, we set the expression in (4.16) equal to 0.9, to obtain

$$\alpha\beta\xi = 1.72484 \tag{6.13}$$

leading to the following for the Gaussian case

$$\frac{2\pi D}{\lambda}\sigma_\theta \xi_d \sigma_\nu \tau = 0.27452 \tag{6.14}$$

which is again consistent with the quarter-pixel rule-of-thumb, and numerically very close to (6.8).

The low frequency (narrow bandwidth) cut-off for σ_θ, comes from a constraint similar to that in (6.10), but since we must constrain the *maximum* pointing fluctuation (in a statistical sense), we approximate this by setting

$$(3\,\sigma_\theta)_{max} \quad = \quad 0.368^\circ \quad = \quad 6430 \ \mu\text{rad} \tag{6.15}$$

which occurs at a frequency bandwidth of $\sigma_\nu = 0.0901$ Hz in (6.14).

In the high frequency regime, $\beta >> 1$, we set (4.17) equal to 0.9 to obtain

$$\alpha\xi_d \quad = \quad 0.45904 \tag{6.16}$$

or

$$\sigma_\theta \quad = \quad 5.845 \ \mu\text{rad} \tag{6.17}$$

which is a little stricter than that found in the deterministic case, (6.12). This result is not surprising when we consider that the statistical case includes fluctuations at *all* frequencies whereas the deterministic case leading to (6.12) is for a *single* high frequency component.
To patch the two limiting forms together, I found, after some trial and error, a monotonic function which limits to the forms in (6.14) and (6.17), and basically smoothes out the transition between the two limits while minimizing the excursion in the OTF. This form is given by

$$\sigma_\theta \quad = \quad \frac{193.11}{\sigma_\nu}\sqrt{\left(\frac{5.845}{193.11}\,\sigma_\nu\right)^2 + 1} \quad \mu\text{rad} \tag{6.18}$$

where σ_ν is in Hz. This function is plotted in Figure 3a. Figure 3b shows the resulting OTF using the full expression in (4.14), and performing the integration numerically. As in the deterministic case, there is some excursion from 0.9 in the transition region. However, for the particular form chosen in (6.18) the OTF always remains *greater* than 0.9. (As a side note, it was found during this analysis that in the deterministic case, all simple, monotonic, smoothing functions resulted in a larger excursion below 0.9 than the piece-wise continuous one used in Figure 2a.)

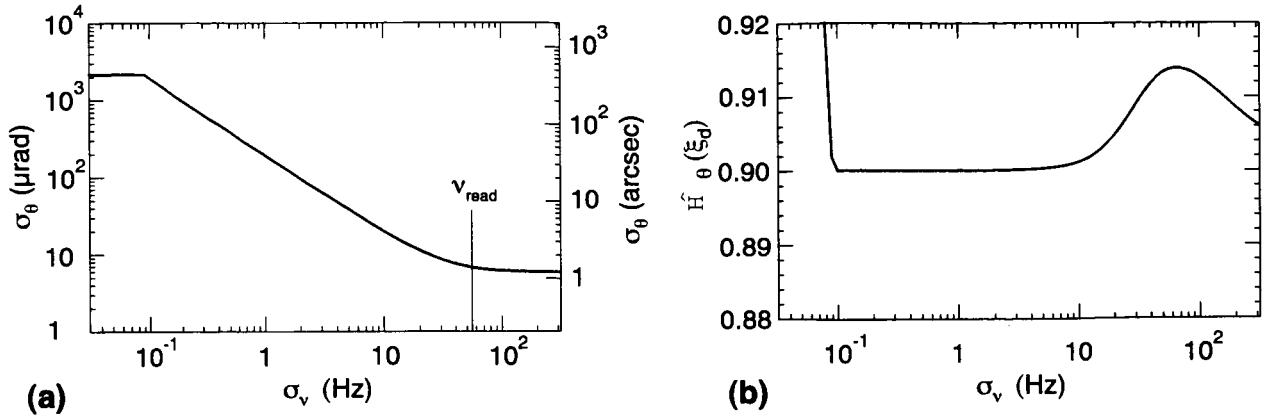

Figure 3. (a) Angular standard deviation as a function of frequency bandwidth, as given by (6.18), for a zero mean Gaussian pointing fluctuation with a zero mean Gaussian power spectral density.
(b) Resulting OTF evaluated at the detector spatial frequency.

For the case of a white noise power spectrum, we simply replace σ_ν with $\nu_{max}/\sqrt{3}$ in all of the preceding analysis. Figure 4a shows the functional form given by (6.18), where now we have σ_θ as a function of ν_{max}. Figure 4b shows the resulting OTF using the full expression in (4.20). Although the OTF dips below 0.9 in this case, it is still reasonably negligible.

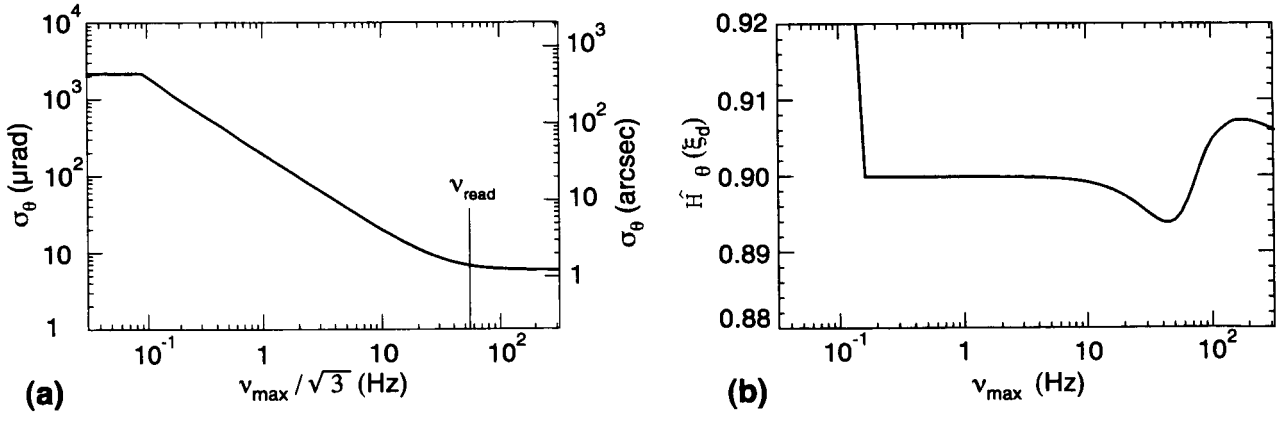

Figure 4. (a) Angular standard deviation as a function of frequency cut-off, as given by (6.18) with the substitution $\sigma_\nu \rightarrow \nu_{max}/\sqrt{3}$, for a zero mean Gaussian pointing fluctuation with a white noise power spectral density.
(b) Resulting OTF evaluated at the detector spatial frequency.

6.3.3 Combined Fluctuations

The final quantitative results to be derived from this analysis are those for the combined case. In general, we can allocate different contributions to the overall degradation of the OTF due to drift or jitter, and again this is a detailed system engineering question. For the purpose of setting requirements, we will assume that the contributions are equal. The easiest starting point is to begin with a "jitter-free" amplitude of 0.95 (approximately the square root of 0.9), and then compute the allowed jitter contribution that drives the OTF to 0.9. I will consider various frequency structures for the stochastic part of the fluctuation and then make some general comments about the sensitivity to this structure.

In the jitter-free case, i.e., when $\sigma_\theta \rightarrow 0$ in (5.7), the integral can be performed, and we obtain

$$H^{\sqrt{}}_{\theta}(\xi) \underset{\sigma_\theta = 0}{=} \frac{\sin(\pi\zeta\xi)}{\pi\zeta\xi} \tag{6.19}$$

which is identical to the result of (3.5). Using the numerical relationship

$$\frac{\sin[\pi(0.17568)]}{\pi(0.17568)} = 0.95 \tag{6.20}$$

we have

$$\begin{aligned} 2\pi\theta_0\nu_0 &= \frac{0.17568}{\tau}\,\frac{\lambda}{\xi_d D} \\ &= 0.776\,\frac{\text{mrad}}{\text{s}} = 0.0445\,\frac{^\circ}{\text{s}} \end{aligned} \tag{6.21}$$

which is more restrictive than the purely deterministic case since here the OTF can only be 0.95. Given this value for $\zeta\xi_d$, we now analyze the effects of adding jitter.

The power spectral density, as given in (5.5), has two parameters: center frequency, ν_m, and bandwidth, σ_ν. Since one of the more stressing cases occurs when the frequency structure of the jitter coincides with the line-scan read frequency, we will consider this first. Thus, I will set

$$\nu_m = \nu_{\text{read}} = 55 \text{ Hz} \tag{6.22}$$

and analyze the effects of different bandwidths. Figure 5 shows the square-root of the power spectral density (in the units of $\mu\text{rad}/\text{Hz}^{1/2}$) as a function of frequency for four different bandwidths, given an overall angular standard deviation, σ_θ, of 5 μrad. The curve marked, $\sigma_\nu \rightarrow 0$, is illustrative of the approach to a delta function at the read frequency, and this limit can be formally taken in (5.7). We see that a wide range of possible power spectral density types are covered by these choices; from an extra-wide zero-mean Gaussian, to a single high frequency component.

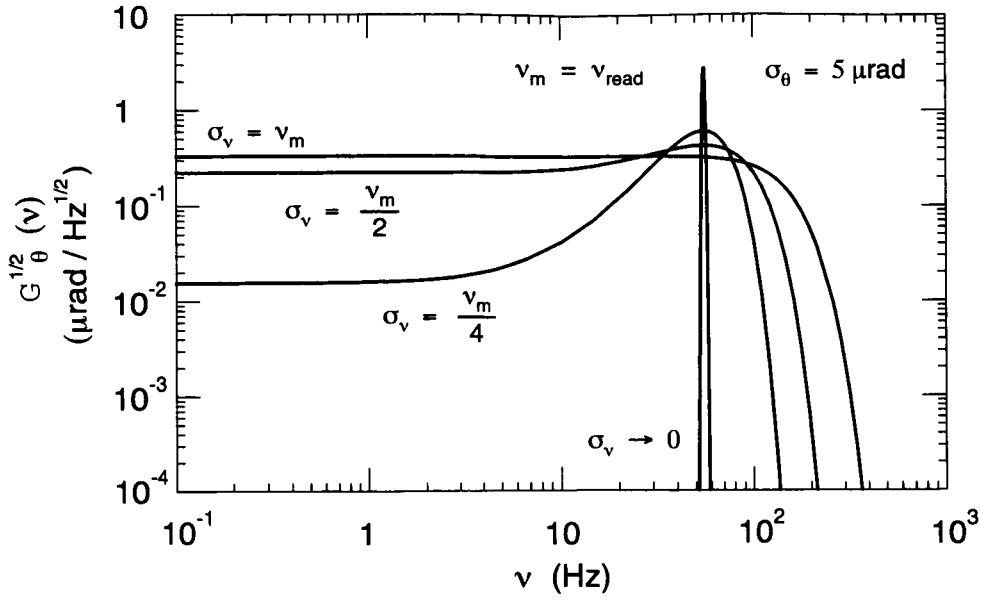

Figure 5. Examples of power spectral densities with different frequency bandwidths.

Figure 6 shows the results of performing the full numerical integration of the OTF in (5.7) using the parameters for the various power spectral densities and varying the overall angular standard deviation, σ_θ. The results indicate that the value of σ_θ for which the OTF reaches 0.9 is reasonably insensitive to the details of the frequency structure, not varying much from approximately 4.5 μrad, about 1/20th of a pixel.

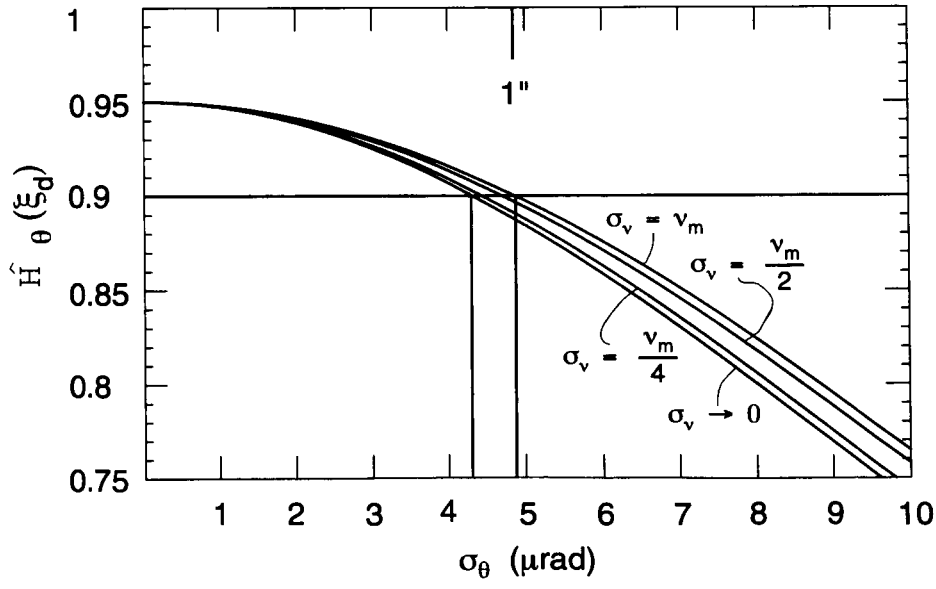

Figure 6. OTF evaluated at the detector spatial frequency for a combined drift and jitter fluctuation as a function of the jitter pointing standard deviation with the following parameters: $\zeta = 0.6507$ (drift = 0.776 mrad/s); $\nu_m = \nu_{read}$.

We can also fix the frequency bandwidth to be some fraction of the center frequency and investigate the effects of increasing the center frequency. Since the previous results were insensitive to bandwidth, I will choose the intermediate case in which $\sigma_\nu = \nu_m/4$. Figure 7 shows the resulting power spectral densities for both $\nu_m = \nu_{read}$ (as in the previous cases) and $\nu_m = 10\ \nu_{read}$, again with an overall angular standard deviation of 5 μrad. Figure 8 shows the resulting OTF evaluated at the detector spatial frequency. We see that the value of σ_θ for which the OTF reaches 0.9 is also insensitive to the choice of center frequency; a factor of ten increase results in only a minor decrease in σ_θ. Thus, once we decompose the pointing fluctuation into low and high frequency components, the details of the random high frequency structure are mostly irrelevant. This makes setting general spacecraft requirements easier.

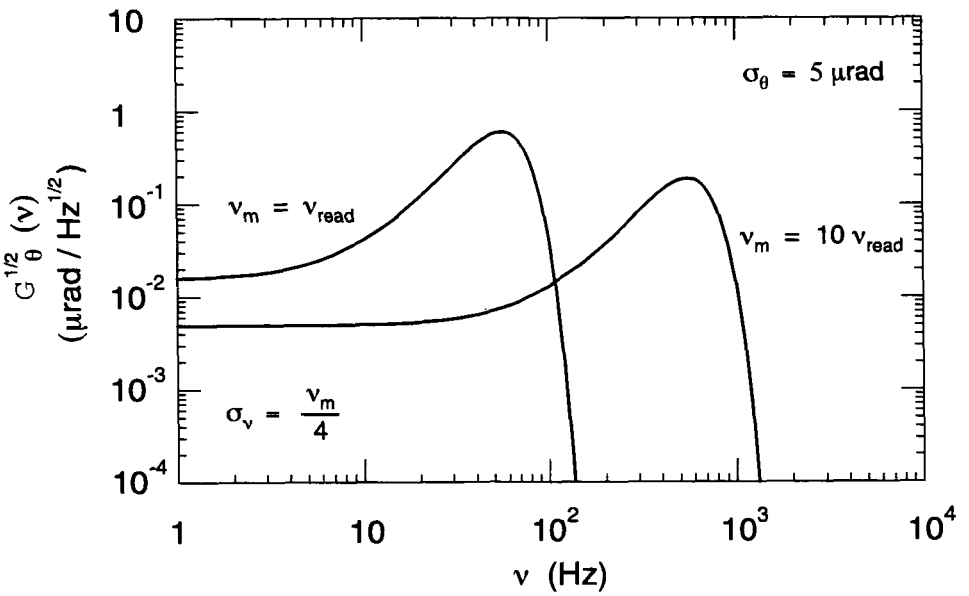

Figure 7. Examples of power spectral densities with different center frequencies.

7. Conclusions

A very general methodology was constructed to analyze the effects of both deterministic and stochastic pointing fluctuations and a combination of both on imaging performance. The techniques were applied to the case of a high resolution stereo camera in a specific orbit around the Moon. It was found that in the case of both drift and jitter components, a drift rate of 0.776 mrad/s is allowed, provided that the one-sigma standard deviation of the random component is less than about 4 μrad (or 1/20th of a pixel).

It is relatively straightforward to extend this analysis to other imaging scenarios. For example, it turns out that the drift rate is independent of the pixel size that is chosen for imaging, provided the exposure time is

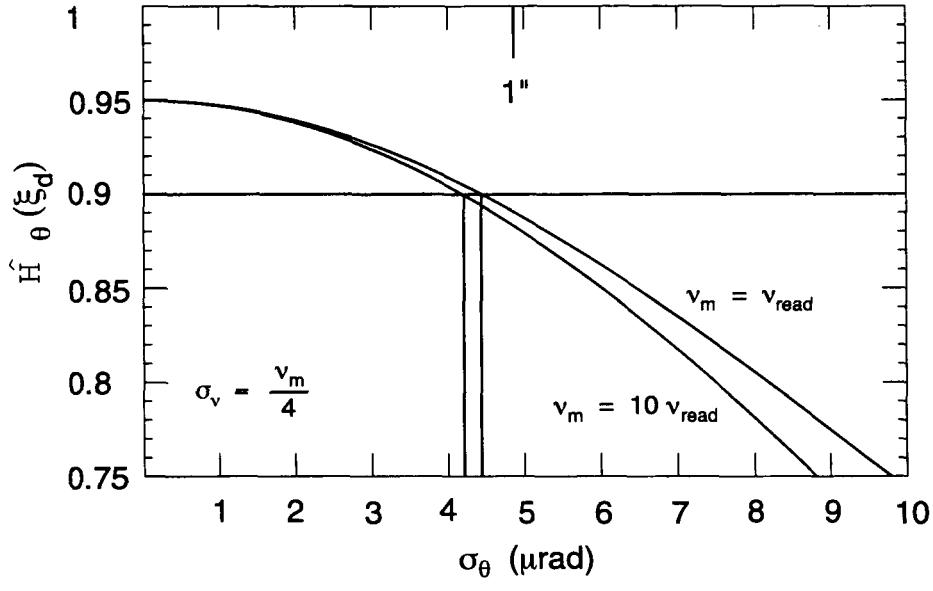

(7.1)

Figure 8. OTF evaluated at the detector spatial frequency for a combined drift and jitter fluctuation as a function of the jitter pointing standard deviation using the parameters shown and $\zeta = 0.6507$ (drift = 0.776 mrad/s).

scaled linearly with pixel size (which is typically the case). Then the drift rate only depends on the angular velocity of the spacecraft, and for a satellite in a circular orbit about the Moon, the appropriate scaling is

$$2\pi\theta_0\nu_0 = \frac{0.1697}{\frac{H_{sat}}{R_{moon}}\left(1+\frac{H_{sat}}{R_{moon}}\right)^{3/2}} \quad \frac{\text{mrad}}{\text{s}}$$

where H_{sat} is the orbital altitude of the satellite and R_{moon} is the radius of the Moon. Once this drift rate is computed, the only additional requirement is that all high frequency jitter amplitudes (three-sigma) be

less than about 1/7th of an imaging pixel expressed in angular units, with little regard to the frequency structure of the jitter. These relationships can be used quite generally, as was shown in the analysis, to set spacecraft pointing requirements.

8. Acknowledgments

I would like to express my sincere appreciation to the (now defunct) DOE Office of Space and the (now defunct) NASA Office of Exploration and JSC Exploration Program Office for the opportunity to work on this project. I am very grateful to Mike Griffin and Fenton Carey, as well as Dave Bartine and Doug Cooke for giving it their best shot. I am also most indebted to Mike Conley for continuing support when it still looked like we had a chance. I immensely enjoyed working with the whole Lunar Scout team, including Mike, Don Morrison, Bret Drake, Beth Caplan, Kent Joosten, Faith Vilas, and Mark Nebrig. I also would like to acknowledge useful discussions with (and I apologize if I leave anyone out) A. Santo and A. Cheng of APL, R. Kirk of the USGS, P. Spudis of LPI, and the whole HRSC team, who I was looking forward to working with, including G. Neukum, R. Jaumann, H. Ebner, J. Albertz, A. Drescher, W. Kornus, R. Pischel, and T. Ohlhof. This work was performed under the auspices of the U. S. Department of Energy by the Lawrence Livermore National Laboratory under contract number W-7405-ENG-48 with partial funding provided by the National Aeronautics and Space Administration, Johnson Space Center.

References

[1] J. W. Goodman, *Introduction to Fourier Optics*. McGraw-Hill Book Co., San Francisco, pp. 113-123, (1968).

[2] I. S. Gradshteyn and I. M. Ryzhik, *Table of Integrals, Series, and Products*. Academic Press, New York, p. 973, Eq. 8.511.3, (1980).

[3] J. W. Goodman, *Statistical Optics*. John Wiley & Sons, New York, pp. 63-68, (1985).

[4] *ibid.*, pp. 19-21.

[5] *ibid.*, p. 376.

[6] *ibid.*, pp. 73-79.

[7] B. Drake and T. W. Lawrence, "Lunar Scout Program--Preliminary Mission Analysis," NASA-JSC-EXPO-T2-930004-EXPO, (March, 1993).

[8] J. Albertz, H. Ebner, C. Heipke, G. Neukum, and F. Scholten. "The Camera Experiments HRSC and WAOSS on the Mars 94 Mission," *Int. Arch. of Photogrammetry and Remote Sensing*, Vol. 44, pp. 1499-1512, (December, 1978).

[9] O. Hofmann, P. Navé, H. Ebner, "DPS---A Digital Photogrammetric System for Producing Digital Elevation Models and Orthophotos by Means of Linear Array Scanner Imagery," *Photogrammetric Engineering and Remote Sensing*, Vol. 50, pp. 1135-1142, (August, 1984).

[10] H. Ebner, W. Kornus, and G. Strunz, "A Simulation Study on Point Determination Using MOMS-02/D2 Imagery," *Photogrammetric Engineering and Remote Sensing*, Vol. 57, pp. 1315-1320, (October, 1991).

[11] W. Kornus, private communication, (August, 1993).

Appendix D

Appendix D - New Ways of Doing Business

Author: Donald A. Morrison, NASA Johnson Space Center

Introduction

The Lunar Scout Program had a small budget and a tight schedule. It was necessary to make decisions expeditiously and to trim the time required to perform traditional government tasks. Management structure, procurement, and the delegation of authority and responsibility were areas that were exploited for increased productivity.

Benchmarking Lessons from Successful Programs

In an effort to have cost-effective management and to provide an innovative approach to managing the relationship between government and contractors, the Exploration Programs Office and the Office of Exploration sought the views of a large number of managers of successful programs, both in industry and government. The following ingredients of a successful program were universally recommended by those who were interviewed.

- Use government only to define and verify requirements.
- Keep requirements fixed; once requirements are stated, only relax them; never add new ones.
- Place product responsibility in a competitive private sector.
- Specify end results (performance) of products, not how to achieve results.
- Minimize government interference (small program offices).
- Ensure that all technologies are proven prior to the end of competition.
- Utilize the private sector reporting system; reduce or eliminate specific government reports.
- Do not start a new program until cost estimates and budget availability match.
- Minimize or eliminate government-imposed changes.
- Reduce development time—any program development can be accomplished in three to four years once uncertainties are resolved.
- Force people off development programs when development is complete.
- Motivate the contractor to keep costs low.
- Use geographic proximity of contractors when possible.
- Use the major prime contractor as the integrating contractor to reduce interfaces and keep responsibilities cleanly defined.

These guidelines were applied to procurement of the spacecraft fabricator for the Lunar Scout Program.

Procurement

The Lunar Scout Program served as a test case in the development of a competitive procurement strategy for a commercial spacecraft buy (Ref. 1). The strategy, designed to allow vendors to estimate costs and schedule risks accurately, consisted of a two-step procurement process: (1) a "horse race" procurement with two competing vendors to conduct a mission/spacecraft study leading to the development of a final proposal, and (2) a final competition between the two "horse race" competitors for the contract for spacecraft fabrication.

In a "horse race" procurement, a competition is held to select two companies that are then funded to study a mission (or a project) so as to become thoroughly familiar with all aspects. The study results in proposals that are submitted for a final competition—the second step in the strategy—in which the vendor is selected. The "horse race" study phase can result in proposals that are very accurately costed because all aspects of the missions are thoroughly developed in a competitive atmosphere. The vendors, in effect, are paid for developing a study that becomes a final proposal. The "horse race" procurement (and the opportunity it provides for vendors to thoroughly assess the project that they will bid on) is an up-front investment that pays dividends during the project-build phase because costs and schedule milestones are much more likely to be met.

For the Lunar Scout Program the initial procurement, the competition for the "horse race," was streamlined and completed in record time as the result of several innovative steps taken by the Office of Exploration in the way the procurement was conducted. First, procurement authority was delegated from the Associate Administrator for Exploration to the Explorations Program Office and to the Lunar Scout Program Manager. Many steps in the normal process of competitive procurement were shortened and a number were eliminated. A contracting officer was appointed to work directly with the Program Manager to ensure that no procurement regulations were violated during these preparations. Activities commonly performed in series were performed in parallel because of the close linkage between the Program Manager and procurement. The spacecraft Request for Proposal (RFP) was simplified. Only performance requirements were defined. Strategies necessary to meet performance requirements were left to the respondents to define in their proposals.

These actions trimmed about 70 days from the average RFP procurement cycle. The response from industry (to the character of the RFP) was overwhelmingly favorable because it allowed them to produce better proposals at lower cost.

References

1. Mandell, H.C., and Griffin, M.D., Management As the Enabling Technology for Space Exploration, American Institute of Aeronautics and Astronautics, 1992.

REPORT DOCUMENTATION PAGE

Form Approved
OMB No. 0704-0188

1. AGENCY USE ONLY (Leave Blank)	2. REPORT DATE	3. REPORT TYPE AND DATES COVERED
	Apr/94	Technical Memorandum

4. TITLE AND SUBTITLE
The Lunar Scout Program: An International Program to Survey the Moon From Orbit for Geochemistry, Mineralogy, Imagery, Geodesy, and Gravity

5. FUNDING NUMBERS

6. AUTHOR(S)
Donald A. Morrison, Editor

7. PERFORMING ORGANIZATION NAME(S) AND ADDRESS(ES)
Lyndon B. Johnson Space Center
Houston, Texas 77058

8. PERFORMING ORGANIZATION REPORT NUMBERS
S-762

9. SPONSORING/MONITORING AGENCY NAME(S) AND ADDRESS(ES)
National Aeronautics and Space Administration
Washington, D.C. 20546-0001

10. SPONSORING/MONITORING AGENCY REPORT NUMBER
TM-104791

11. SUPPLEMENTARY NOTES

12a. DISTRIBUTION/AVAILABILITY STATEMENT
unclassified/unlimited
Available from the National Technical Information Service
3285 Port Royal Road
Springfield, VA 22161 (703) 487-4600
Subject category: 91

12b. DISTRIBUTION CODE

13. ABSTRACT *(Maximum 200 words)*

The Lunar Scout Program was one of a series of attempts by NASA to develop and fly an orbiting mission to the Moon to collect geochemical, geological, and gravity data. Predecessors included the Lunar Observer, the Lunar Geochemical Orbiter, and the Lunar Polar Orbiter - missions studied under the auspices of the Office of Space Science. The Lunar Scout Program, however, was an initiative of the Office of Exploration. It was begun in late 1991 and was transferred to the Office of Space Science after the Office of Exploration was disbanded in 1993.

Most of the work was done by a small group of civil servants at the Johnson Space Center; other groups also responsible for mission planning included personnel from the Charles Stark Draper Laboratories, the Lawrence Livermore National Laboratory, Boeing, and Martin Marietta.

The Lunar Scout Program failed to achieve New Start funding in FY93 and FY94 as a result of budget downturns, the de-emphasis of the Space Exploration Initiative, and the fact that lunar science did not rate as high a priority as other planned planetary missions, and was cancelled. The work done on the Lunar Scout Program and other lunar orbiter studies, however, represents assets that will be useful in developing new approaches to lunar orbit science.

14. SUBJECT TERMS
lunar orbiter, lunar satellites, lunar spacecraft, lunar topography, lunar geology, geological surveys, geology, geodesy, geochemistry, lunar gravitational effects, mineralogy

15. NUMBER OF PAGES
155

16. PRICE CODE

17. SECURITY CLASSIFICATION OF REPORT	18. SECURITY CLASSIFICATION OF THIS PAGE	19. SECURITY CLASSIFICATION OF ABSTRACT	20. LIMITATION OF ABSTRACT
unclassified	unclassified	unclassified	UL